Annual Activity Report 2010

National Institute of Surface Engineering

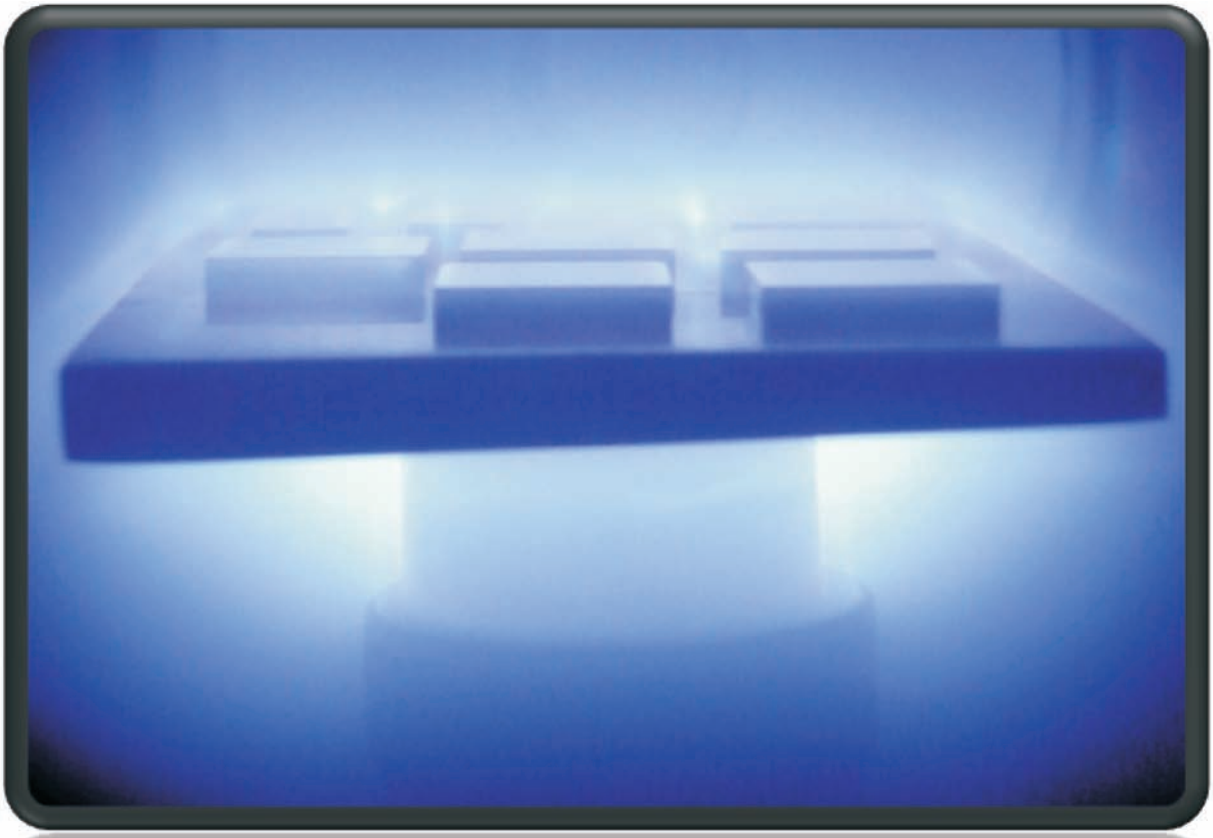

Table of Contents

Overview

Surface Engineering

Surface Engineering is the technology of preparation and modification of engineering devices that fulfills specific functions without significant change in the component dimensions. It provides technological advantage and produces effective solutions in several industrial sectors like, oil and gas industry, aeronautic and aerospace, car industry, micro and nanoelectronics, etc. While the surface engineering, on one hand, allows for the synthesis of surfaces with unusual and valuable properties, on the other hand, the scientific knowledge and the processes control in this field is still insufficient. Despite of that, Surface Engineering is widely used in industrial production of developed countries and there are many potential applications for different branches of the Brazilian industries.

National Institute of Science and Technology of Surface Engineering

The National Institute of Science and Technology of Surface Engineering (INES) main goal is the development of scientific knowledge that will result in innovative and sustainable development in many industrial segments.

The main objectives of this National Institute of Surface Engineering are:

- investigation of physical-chemical interactions of solid surfaces and interfaces;
- applications of surface engineering and transfer of this knowledge to the industrial productive system and to society;
- formation of high level human resources in surface engineering.

Coordinator: Fernando Lázaro Freire Junior (PUC-Rio)

Executive Board:
Israel J. R. Baumvol (UCS)
Pedro Grande (UFRGS)
Francisco Marques (UNICAMP)
Amilton Sinatora (USP)
Clodomiro Alves (UFRN)
Vladimir Jesus Trava-Airoldi (INPE and Clorovale Diamante S.A.)
Carlos Figueroa (UCS and Plasmar Indústria Metalúrgica)

Besides the coordination of the research activity, the executive board is responsible for the budget, the distribution of fellowships and grants to graduated students and associate researchers, the diffusion of knowledge via the institute website, meetings and scientific conferences as well as contacts with the productive sector. The executive board has an annual meeting, in 2009 it was in Porto Alegre and this year it will be in October at Ouro Preto, during the Annual Meeting of the Brazilian Research Society, while several topics were discussed along the year using internet and video conferences.

Main Researchers:
Pedro Grande (Ion Implantation Laboratory /UFRGS)
Livio Amaral (Ion Implantation Laboratory /UFRGS)
Gabriel Vieira Soares (Ion Implantation Laboratory /UFRGS)
Fernando C. Zawislak (Ion Implantation Laboratory /UFRGS)
Paulo Fernando Fichtner (Ion Implantation Laboratory /UFRGS)
Johnny Ferraz Dias (Ion Implantation Laboratory /UFRGS)
Marcos Vasconcellos (Nanolitography Laboratory/UFRGS)
Cristiano Krug (Chemical-Physics of Surface and Interfaces Laboratory/UFRGS)
Daniel Eduardo Weibel (Chemical-Physics of Surface and Interfaces Laboratory/UFRGS)
João H. Zimnoch dos Santos (Catalysis Laboratory/UFRGS)
Carlos Fortis Kwietniewski (Physical Metallurgy Laboratory/UFRGS)
Dante Franceschini (Thin Films Laboratory /UFF)
Valdir Soldi (Polymeric Materials Laboratory/UFSC)
Claudia Trindade Oliveira (Materials Laboratory / Feevale)
Amilton Sinatora (Surface Phenomena Laboratory /USP)
Roberto Martins de Souza (Surface Phenomena Laboratory /USP)
Paulo Mei (Thermo Mechanical Treatments Laboratory /UNICAMP)
Carlos Figueroa (Surface Engineering Laboratory/UCS)
Israel J. R. Baumvol (Surface Engineering Laboratory/UCS)

Cláudio Perottoni (Surface Engineering Laboratory/UCS)
Fernando Lázaro Freire Jr (Nanostructured Materials and Coatings Laboratory /PUC-Rio)
Carlos Manuel Sanchez Tasayco (Nanostructured Materials and Coatings Laboratory /PUC-Rio)
Monica de Mesquita Lacerda (Thin Films Laboratory/UDECS)
Julio Pureza (Thin Films Laboratory/UDESC)
Francisco Marques (Photovoltaic Research Laboratory/UNICAMP)
Clodomiro Alves (Plasma Processing Laboratory/UFRN)
Vladimir Jesus Trava-Airoldi (Materials and Sensors Laboratory/INPE)
Alessandra Venâncio Diniz(Materials and Sensors Laboratory/INPE)

Institutions:

Protective Coatings Laboratory (Physics Department, PUC-Rio)

The Protective Coatings Laboratory started its activities in 1994 and since then the focus of the research is on the production and characterization of hard coatings. Carbon and carbon alloys films (carbon nitride and carbon-fluorine films), boron carbide and titanium diboride coatings chemical, mechanical and tribological properties were investigated. Recently, also the study of multiwalled carbon nanotubes (MWNT) is on progress and the focus is on the doping of this material by boron, nitrogen and phosphorus atoms. The laboratory occupies an area of 150 m2 in the Van de Graaff Laboratory building.

Infrastructure

For sample preparation we have the following systems:

- Thin film deposition chamber equipped with plasma assisted techniques (PECVD and dc or rf magnetron sputtering).
- System for MWNT growth by spray pyrolysis.
- CVD system for carbon nanoutbe growth (tubular furnace and controlled atmosphere up to 11000 C).
- Furnace for high vacuum or controlled atmosphere treatments (up to 9000 C).

For sample characterization the laboratory is equipped with:

- Nanoindenter TriboIndenter from Hysitron.
- Field emission scanning electron microscope (FEG-SEM) Jeol JSM 7600 F.
- NTEGRA Spectra AFM Raman from ND-MDT.
- Omicron ultra-high vacuum STM.
- Surface characterization system from Thermo equipped with an Alpha 110 analyzer.
- Microwear test system CALOWEAR from CSEM.
- Homemade goniometer for contact angle measurements.

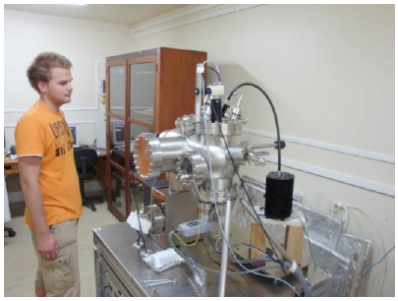

STM

NTEGRA Spectra AFM Raman

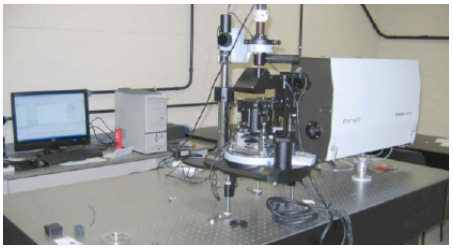

Nanoindenter

Materials Laboratory (University FEEVALE)

The researcher Cláudia Trindade Oliveira make use of the infrastructure of the Materials Laboratory, in addition to other laboratories at the University Feevale available to perform her research. In the materials laboratory, the equipments are located as follows:

- Potentiostat/Galvanostat AUTOLAB PGSTAT 302 with impedance modulo (FRA2) connected to a computer.
- Multimeter AGILENT wiht 6 e ½ digits.
- Voltage x current power supply, 20V, 2A.
- Voltage x current power supply, 30V, 4A.
- Voltage x current power supply, 300V, 0,5A

(that will be acquired until the end of 2010).

Recently, the researcher acquired the equipments as follows:

- Oven until 1200ºC.
- Oven with controlled atmosphere until 1000ºC.
- Sanding machine.
- Polishing machine.

LOFF - Laboratory of Optics and Thin Films (Physics Department, UDESC -Universidade do Estado de Santa Catarina)

Facilities

One home made plasma enhanced chemical vapor deposition (PECVD) system with temperature control of the substrate holder, pressure gauges, power supply 1000V, 1A; and mass flow controllers. The micro prosessing system control all stages of the film deposition process.

At UDESC others facilities are accessible as scanning electron microscopy, electron dispersive x-ray spectroscopy, Fourier transform infra-red spectroscopy and sample preparation room.

PECVD system at the LOFF. 60 m2 is the total area of the laboratory. At the right side one see the students' room, where two computers, 3 desks and one cabinet are available.

Thin Film Laboratory (Physics Institute- UFF, Universidade Federal Fluminense)

The laboratory has two main research objectives: the study of plasma deposited a-C:H films (DLC films) and the study of nanostructured metal oxide films deposited by laser ablation.

Laboratory facilities

Plasma deposited a-C:H films:

- Plasma deposition system, consisting of cylindrical SS vacuum chamber, high vacuum pumps, 4 gases admission system with mas flow controlers, absolute pressure measurement by capacitive manometer, 600 W RF power supply with automatic impedance matching network. All the system is interfaced with a personal computer in order to allow automatic control of the experiments. Film growth is probed by in-situ, real-time, near-normal laser reflectance, in order to determine the optical constants and film growth rate. (Fig. 1)
- CETR universal tribological test machine, capable of pin-on-disk, reciprocating and scratch tests in two normal force ranges 5-500 mN and 0.5 – N. The system is equiped with chamber for measurements in ambient atmosphere, liquid medium, and controlled atmosphere. (Fig. 2)

Nanostrucured metal oxide films deposited by laser ablation:

A new deposition chamber is under construction, consisting of a spherical SS chamber equiped with multi-target holder, load-lock chamber, mass spectrometer for plume analysis and high density plasma source. (Fig. 3)

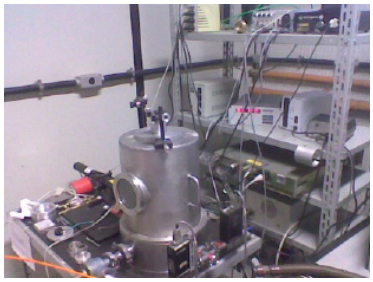

Plasma deposition system

Tribometer

Spherical chamber for laser ablation (to be assembled)

LAS- Materials and Sensors Laboratory (INPE – Instituto Nacional de Pesquisas Espaciais) and R&D Laboratory at Clorovale Diamond S.A.

Related to Surface Engineering, we have many reactors at INPE and at Clorovale Diamante S.A. Also, concerning characterization, we have a new laboratory at INPE for tribological measurements.

PECVD System at INPE for DLC Growth

PECVD System at Clorovale Diamante

Tribological Characterization System from CETR

Plasma Materials Processing Laboratory (UFRN – Universidade Federal do Rio Grande do Norte)

The Labplasma aims to develop research using plasma as energetic source to materials processing. It currently occupies an area of 150 m2. Initially, our researches converged to understanding of plasma nitriding process, working with carbon, tools and stainless steel, beside it had developed critical analysis of plasma nitriding performance on the complex geometry workpieces. A new process was developed in our laboratory, called Cathode Cage Plasma Nitriding (CCPN) where problems as edge and overheating were solved. From 1998 until now the Labplasma have been interacting with different Brazilian research groups, expanding research to other lines as:

Heating of solids immersed in plasma:

Experiments carried out at our laboratory on samples of Cu-10% Al micro-alloyed powders; it was found which those samples when heated by plasma resulted in a microstructure porous on surface but dense in the core. The conclusion of this study showed which the phenomenon occurs due to the fusion of particles of the surface which diffuse by capillary to the nucleus of the material. Based on such studies, it was created a research line in a systematic methodology in order to study the heating of solids with different plasma configurations, such as: planar discharge, (ii) hollow cathode discharge and (iii) Atmospheric microwave discharge.

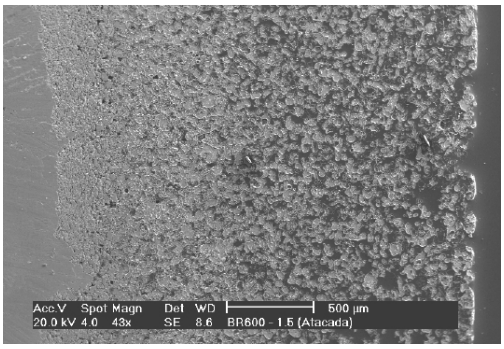

Plasma reduction of metal oxide

Reduction is done by the aluminothermic process, where metallic oxide (Ta2O5, TiO2) mixed with Al stoichiometric proportion using high energy milling, is treated by hollow cathode discharge of H2 atmosphere or plasma spray of argon atmosphere. Thermal peaks are generated due to the collisions of energetic species contained in the plasma. These peaks trigger the reaction in particle individually.

Functionalization of surfaces for tribo-mechanical applications:

In this research line, we have studied thermochemical treatments such as nitriding, oxynitriding , cabonitriding of steels and refractory metals (Ta, Ni and Ti). In this moment a systematic study about titanium modification by interstitials elements plasma (Ar, N2, O2, CH4 and H2).

Functionalization of surfaces for biomedical applications:

In this research line are studied polymer surfaces (polyester, TNT, chitosan and cotton), metal (stainless steel, titanium) and ceramics (hydroxyapatite) modified by DC plasma and DC pulsed plasma. Surfaces are also produced with a gradient of porosity to be utilized as scaffolds for drug delivery and storage. Those surfaces are characterized by wettability measurement, DRX, microhardness assays and optical microscopy. The biological response of samples are evaluated through the adhesion and growth cell measurements. For applications such as scaffolds are evaluated size, shape and pore distribution as well as time-release drugs.

Ion Implantation Laboratory (Physics Institute, UFRGS – Universidade Federal do Rio Grande do Sul)

The core of the laboratory consists of two electrostatic ion accelerators from High Voltage Engineering Europa. One of them is a 500 kV ion implanter, while the other one is 3 MV tandetron accelerator. Both machines provide a wide variety of positive ions in a broad energy range. Several beam lines with different analytical techniques are available to scientists from different fields. The techniques are:

- PIXE (Particle-Induced X-ray Emission): provide elemental concentrations of the order of part per million;
- RBS (Rutherford Backscattering Spectrometry): used for characterization of different structures, including multi-layered targets;
- NRA (Nuclear Reaction Analysis): ideal for profiling and studies of elemental distribution;
- Microprobe: allow the use of techniques like PIXE, RBS and STIM with micrometer beam size;
- MEIS (Medium Energy Ion Scattering): it is a high-resolution RBS technique with isotope-separation capability;
- Ion Implantation: used for modification of materials under controlled parameters.

The infrastructure of the laboratory includes a large variety of charged-particle, X-ray and gamma detectors, modular electronics, ovens and other related equipment. A fully-dedicated workshop allows the maintenance of the laboratory in a regular basis. A general view of the laboratory is shown below, featuring the beam lines of the Tandetron accelerator.

Laboratory of Solid Surfaces and Interfaces (Physics Institute, UFRGS – Universidade Federal do Rio Grande do Sul)

Facilities

Ultrahigh-vacuum surface characterization system (Omicron Nanotechnology) equipped for low energy ion scattering (LEIS) and photoelectron spectroscopy with X-rays (XPS) and ultraviolet radiation (UPS).

Nanofabrication Laboratory (Physics Institute, UFRGS – Universidade Federal do Rio Grande do Sul)

Facilities

Jeol JIB-4500 combined scanning electron microscope and focused ion beam instrument equipped with nanomanipulator and X-ray microanalysis (EDS)

Jeol JIB-4500 combined scanning electron microscope and focused ion beam instrument equipped with nanomanipulator and X-ray microanalysis (EDS)

Ziegler-Natta Catalysis Laboratory (Institute of Chemistry, UFRGS – Universidade Federal do Rio Grande do Sul)

The Ziegler-Natta catalysis Laboratory disposes of the facilities necessary to conduct the catalyst/sorbents/sensors synthesis, characterization and evaluation. There are several devices for supports treatments, glove boxes for the manipulation of air-sensitive materials, reactor for supercritical drying, polymerization reactors. In terms of materials characterization, infrared and ultraviolet accessories for solid analysis (PAS, DRIFTS, DRS, for instance) and nitrogen porosimetry are available. The members have also access to atomic force microscope, ion beams analysis and electron microscopy center of UFRGS.

1 and 2 Büchi reactor

nitrogen adsorption (BET method)

Parr reactor

supercritical drying

Thermal treatment system

Surface Engineering Laboratory (UCS - University of Caxias do Sul)

The Laboratory develops research activities following three different topics:

- Plasma surface treatment of metals.
- Plasma surface treatment of polymers and ceramics.
- Nanostructured protective coatings.

And it is equipped with different plasma based systems, all designed in house, like plasma nitriding by pulsed dc bias, rf and dc sputtering and ion plating.

The students and researchers of the surface engineering Laboratory have access to a last generation experimental facilities for material characterization, including, FTIR spectrometer, X-Ray difractometer and scanning electron microscopy.

Ion plating system

SEM microscope

Infrared Fourier Transform Spectrometer - FTIR (Perkin Elmer)

Industrial plasma nitriding furnace at a spin-off company

Surface Phenomena Laboratory (Mechanical Engineering Department, USP - University of São Paulo)

The Laboratory develops research activities following two research lines:

- Surface phenomena: friction, wear, lubrication and corrosion.
- Control of such phenomena through: (a) numerical modeling, (b) material and coating selections; (c) modifications in design and manufacturing processes.

Facilities

- Wear test equipments
- Abrasion (ball mills, jaw crusher, rubber wheel, micro-abrasion – calo-wear – test with constant force or constant pressure)
- Instrumented press to analyze friction during forming operations
- Erosion
- Dry and lubricated sliding wear
- Contact fatigue
- Rubber tire wear
- Cavitation
- Corrosion test equipment: potentiostat
- Heat treating furnaces
- Roughness measurers
- ABAQUS Software (FEM)
- Material characterization equipments: optical microscopes, durometers, instrumented microdurometer, atomic force microscope-AFM with nanoindentation and nanoscratch testing devices
- Data acquisition systems for machining tests
- Turning and CNC milling machines

Laboratory of Photovoltaic Research (Institute of Physics, UNICAMP – Universidade Estadual de Campinas)

The infra-structure of the Laboratory of Photovoltaic Research includes facilities for the development of solar cells based on crystalline silicon and several deposition systems for the development of thin amorphous films.

Facilities for the development of amorphous thin films using: Filtered Cathodic Vacuum Arc (FCVA), Plasma Enhanced Chemical Vapor Deposition (PECVD), ion gun, electron-beam

laboratory for the development of crystalline silicon solar cells.

Dektak perfilometer

Nanoindenter

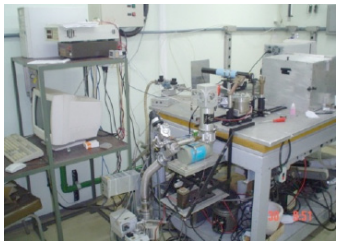

Thermomechanical properties

POLIMAT - Group of Studies on Polymeric Materials (Department of Chemistry – UFSC – Universidade Federal de Santa Catarina)

This group develops activities related to the study and characterization of polymeric systems and preparation of new materials since 1994. The main research fields of the group include the development of biofilms and nanostructured systems for food packaging and drug delivery.

The available physical infrastructure includes laboratories with two hundred square meters for development, preparation of films and biofilms and nanostructured systems, as well as space for equipment, including: thermal analysis system, universal machine test, spin coating, infrared, computers and other small equipments. Multiuser equipments are also available: nuclear magnetic resonance, scanning and transmission electron microscopy, dynamic light scattering and nanozetasizer.

Microanalysis Laboratory (Physics Institute- UFRGS - Universidade Federal do Rio Grande do Sul)

The laboratory develops research activities on:

- Plasma nitriding: processing and characterization of steel and titanium alloys;
- Tribology applied to automotive braking systems: tests and surface characterization;
- Microanalysis EDS quantification using certified standards; x ray mapping, dynamic microhardness, microRaman spectroscopy;
- Material characterization: Glancing Incidence X ray diffraction and X ray reflectometry, Mossbauer Spectroscopy;
- Mineral characterization: gems and jewels, zircon and monazites.

Facilities

Ultra Micro Hardness Tester Shimdzu DUH211S

X-Ray difractometer Shimadzu XRD 6000

Micro Raman Spectroscopy

Scanning Electron Microscopy Jeol LV5800

Science Highlights

Our Institute has stimulated and/or started a series of collaborations between high qualified research groups from different institutions.

We advanced in the description of the thermal stability of surfaces and interfaces that are relevant for (nano) electronics. We have studied the semiconductors SiC and Ge; the dielectrics $LaLuO_3$, HfO_2, Al_2O_3, and SiON; and the metal Pt. By understanding the transport of oxygen, nitrogen, hydrogen, and different heavier elements in these materials we expect to contribute for their use in electronic devices that provide high performance and low power consumption.

Besides the development of new deposition processes and surface treatments based on cold plasmas with potential applications in metal-mechanics, textile and biomedical industries, our researchers developed a new high performance coating: diamond-like carbon (DLC)-nanodiamond composite films which are promising materials for tribological applications. Further improvement on DLC and titanium-based coatings are expected as a result of the present investigations.

We are developing a new technique to characterize nanostructures on a surface using medium-energy ion scattering. We have already determined shape and size distribution of the Au nanoparticles(NPs) adsorbed on a multilayered film of weak polyelectrolyteis and Pb nanoislands at Si/SiO_2 interface. The results are very promising and open new perspectives to analyze core-shell NPs and to investigate the formation of nanostructures in situ.

In the following sections some of these results are described in detail. At the end of this section one can find a complete list of publications, patents and communications presented in international conferences. The highlights of the scientific production can also be found in our website: http://www.engenhariadesuperficies.com.br.

Surface passivation of Ge(100) with $LaLuO_3$ for application in nanoelectronics

G. V. Soares,[1] C. Krug,[1] C. Radtke,[2] I. J. R. Baumvol,[1,3] J. M. J. Lopes,[4] E. Durgun-Ozben,[4] A. Nichau,[4] J. Schubert,[4] and S. Mantl[4]

[1]Instituto de Física and [2]Instituto de Química, UFRGS, Porto Alegre, RS, Brazil
[3]Universidade de Caxias do Sul, Caxias do Sul, RS, Brazil
[4]Institute for Bio- and Nanosystems, Jülich Research Center and Jülich Aachen Research Alliance, Jülich, Germany

Abstract

Lanthanum lutetium oxide ($LaLuO_3$) films, 6 and 12 nm-thick, were prepared on Ge(100) by molecular beam deposition and submitted to thermal annealing in N_2 or O_2. Electrical characterization revealed that such treatments can have beneficial effects on the characteristics of the dielectric layer. Nevertheless, $LaLuO_3$/Ge interface characteristics are modified depending on annealing parameters and mostly on the employed atmosphere. Electrical characterization was correlated with atomic transport and chemical bonding in the resulting structures, evidencing that oxygen annealing, in certain conditions, promotes substrate oxidation. A more stable interface without the formation of excessive Ge oxidized species was achieved using N_2.

Introduction

The continued downscaling of Si-based metal-oxide-semiconductor field-effect transistors (MOSFETs) using SiO_2 as a gate dielectric has reached fundamental limits. The required SiO_2 layer thicknesses (~1 nm) gives rise to unacceptable values of gate leakage current. To continue the scaling of Si-based MOSFETs, new materials of higher dielectric constant (high-*k*) replaced thermally grown SiO_2. Because new materials are being used in place of SiO_2, the dominant role played by Si as semiconductor material is being re-evaluated. Materials of higher intrinsic carrier mobility such as Ge could be used to build faster devices. However, one must find an adequate gate insulator material that forms an interface with Ge with a sufficiently low density of active interface defects. The dielectric/Ge structure must also withstand the transistor fabrication process, which involves temperatures above 400°C.

A number of Ge passivation routes have been investigated, such as surface treatments before high-*k* deposition and formation of interlayers between Ge and the gate insulator.[1] The latter strategy consists of creating a layer that efficiently passivates the Ge surface and isolates it from the deposited high-*k* dielectric. These interlayers can be (i) thermally grown GeO_2 or GeO_xN_y or (ii) rare-earth oxides (for example, La_2O_3), which interact with the substrate forming germanates.[2]

In the present work, we investigate the passivation properties of lanthanum lutetium oxide ($LaLuO_3$) deposited on Ge. This dielectric material is a promising candidate for high-*k* applications. $LaLuO_3$ thin films deposited on Si presented thermal stability up to 1000°C. Electrical characterization revealed good capacitance-voltage (C-V) behavior, low leakage current density, and *k* value of ~32.[3] This ternary rare-earth oxide may interact with Ge forming an interlayer, resulting in a dielectric/Ge structure with a low density of interface states (D_{it}). However, the formation of a germanate at the dielectric/Ge interface can also result in a film of low dielectric constant and a rather high leakage current, as observed for La_2O_3 deposited on Ge.[2] Aiming at obtaining a dielectric layer with simultaneously good bulk and interfacial properties, $LaLuO_3$/Ge structures underwent different postdeposition annealings (PDAs). The electrical characteristics of the resulting samples were correlated with physicochemical modifications.

p-Type epi-ready Ge(100) doped with Ga wafers (Umicore) with a resistivity of 0.24 - 0.47 Ω cm were first cleaned in a mixture of acetone and propanol. They were then etched in a 2% HF aqueous solution for 4 min. After rinsing the samples in deionized water for another 4 min, they were immediately loaded in the deposition chamber. The remanent oxidized Ge was sublimed by sample heating at 450°C under ultrahigh vacuum conditions for several minutes. $LaLuO_3$ films (6 and 12 nm-thick) were deposited by molecular beam deposition using a conventional chamber with a controlled admission of oxygen for oxide growth. Samples were kept at 300°C during deposition. Thermal processing was performed in a resistively heated quartz tube furnace under a static pressure of 150 mbar of either N_2 (<1 ppm of H_2O) or O_2 enriched to 97% in the isotope of mass 18 (termed $^{18}O_2$) at 300 or 400°C. For electrical characterization of the formed structures, Pt top contacts were deposited by electron-beam evaporation through a shadow mask, followed by a forming gas anneal at 300°C for 10 min. C-V and conductance–voltage curves were measured using an impedance analyzer (HP 4192A). D_{it} was extracted according to Terman's method and by considering the peak conductance.[4] The EOTs of the films were determined by fitting the experimental C-V curves with a Hauser fit,[5] taking into account quantum-mechanical corrections. The depth distribution of ^{18}O in the annealed samples was determined by nuclear reaction profiling (NRP) using the resonance at 151 keV in the cross-section curve of the $^{18}O(p,\alpha)^{15}N$ nuclear reaction.[6] X-ray photoelectron spectroscopy (XPS) was performed in an Omicron SPHERA station using Al Kα radiation.

Figure 1 shows electrical characterstics of the $LaLuO_3$/Ge structures before and after different thermal treatments. All samples were prepared by deposition of a 12 nm-thick oxide film. The as-deposited layer revealed C-V curves without humps or irregularities (Fig. 1a), relatively low D_{it} levels around 6×10^{11} eV^{-1} cm^{-2} (Fig. 1b), and a high EOT (~3.3 nm). To improve the electrical characteristics of the dielectric film, different PDAs were performed. In the present work, PDAs were performed in N_2 or $^{18}O_2$ atmospheres at 300 or 400°C for 10 or 30 min. EOT values of the resulting samples decreased in all cases. For samples treated in $^{18}O_2$, the harsher the annealing conditions (higher temperature and longer time), the lower the EOT. The best EOT value was obtained for the sample annealed in N_2. However, PDA led to stretch-out of the C-V curve at the

depletion region (Fig. 1a), which is an indication of a higher D_{it}. Indeed, as shown in Fig. 1b, the treatments in $^{18}O_2$ resulted in higher D_{it} values compared with the sample treated in N_2 and even with the as-deposited one, which indicates that oxygen is triggering unwanted modifications in the dielectric film.

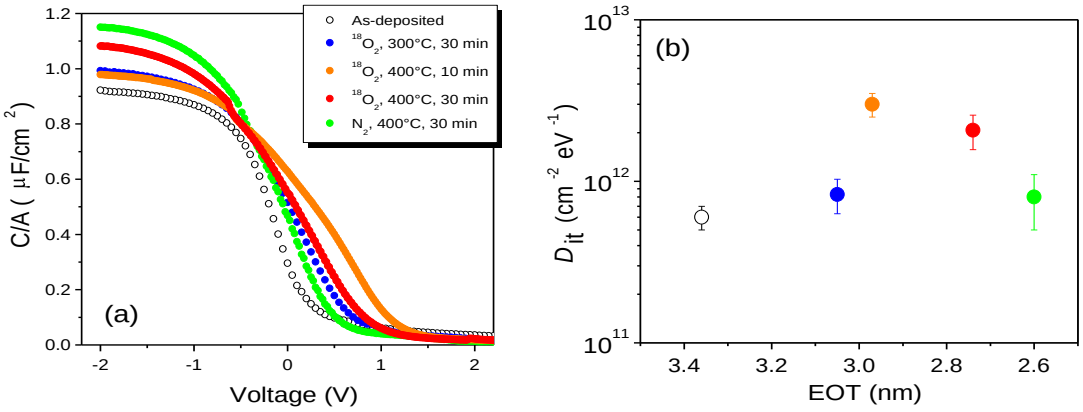

Figure 1. (a) C-V curves at 100 kHz for as-deposited and annealed $LaLuO_3$ films on Ge. Figure 1. (b) D_{it} values obtained from the peak conductance plotted as a function of the EOT of the $LaLuO_3$ films before and after different PDAs. D_{it} levels determined by Terman's method (not shown) reveal similar values.

Aiming at identifying the role played by the oxygen atmosphere on the properties of the dielectric/semiconductor structure, we performed ^{18}O depth profiling. Because we employed an isotopically enriched gas, we were able to distinguish oxygen originally present in the dielectric layer from that incorporated after PDA. Comparing the excitation curves (Fig. 2), one can observe that higher amounts of ^{18}O are incorporated as temperature and time of the annealing are raised. Harsher annealing conditions also result in deeper regions reached by ^{18}O, indicating that oxygen from the gas phase interacts with the semiconductor substrate at least for samples oxidized at 400°C for 30 min. This fact could explain the high D_{it} values obtained from these structures, which are probably a result of substrate oxidation. Counterpart samples were prepared on Si to infer about the influence of the substrate material in ^{18}O incorporation. ^{18}O profiles of these samples were similar to their Ge counterparts, evidencing that most part of ^{18}O incorporation results from its interaction with the $LaLuO_3$ matrix. ^{18}O profiles of Ge samples are slightly wider than their Si counterparts, which is probably a result of the higher reactivity of Ge with incoming oxygen.

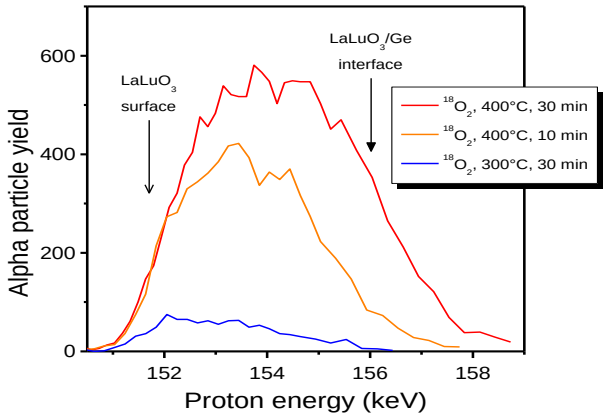

Figure 2. Excitation curves for the $^{18}O(p,\alpha)^{15}N$ nuclear reaction in $LaLuO_3$/Ge structures after different PDAs in $^{18}O_2$. The surface and $LaLuO_3$/Ge interface positions are indicated.

The formation of oxidized Ge has a strong impact on the electrical characteristics of the final structure. XPS analysis was performed to identify chemical modifications at the dielectric/semiconductor interface. To probe this interfacial region, thinner $LaLuO_3$ films (6 nm-thick) were deposited. Figure 3 shows O 1s and Ge 3p regions of the XPS spectra for the as-deposited and annealed samples. The as-deposited sample presents a Ge 3p signal with two peaks characteristic of bulk Ge. After PDA, a signal component at higher binding energy (BE = 123.1 eV) is observed, indicating that Ge is oxidized. Comparing the spectra of the sample annealed in $^{18}O_2$ with that annealed in N_2, higher amounts of oxidized Ge are observed in the former. Because higher D_{it} values were obtained for samples annealed in $^{18}O_2$, the formation of such compounds could be considered detrimental to interfacial characteristics.

The sample annealed in N_2 presented D_{it} comparable to that of the as-deposited sample despite the occurrence of a component at high BE in the Ge 3p signal. This result indicates that besides the formation of $LaGeO_x$,[8] which was shown to be beneficial to interfacial characteristics, other Ge oxidized species are formed during annealing in O_2. The formation of volatile GeO (Ref. 14) resulting from Ge oxidation is a probable explanation for this observation and for the detrimental electrical

effects of PDAs performed in O_2. O 1s spectra corroborate this scenario. The signal from the as-deposited sample has two contributions: (i) at 529.1 eV related to oxygen in LaLuO3 and (ii) at 531.3 eV related to carbonate and hydroxide species.[8] The relative intensity of the $LaLuO_3$ component rises after PDAs, indicating a reduction of hydroxide-related surface contamination and of carbonate species incorporated in the film, simultaneously with a reduction in the amorphous character of the annealed films.[8] Similar results were observed for $LaLuO_3$ films deposited on Si substrates.[9] Such modifications are likely to have an effect on the electrical characteristics of the final structure, as evidenced by the EOT values in Fig. 1. Another contribution at a higher BE (~532.3 eV) is also observed for annealed samples, related to oxygen bonded to Ge. This component is most intense for the sample annealed in oxygen, evidencing that Ge oxidation is triggered by such annealing.

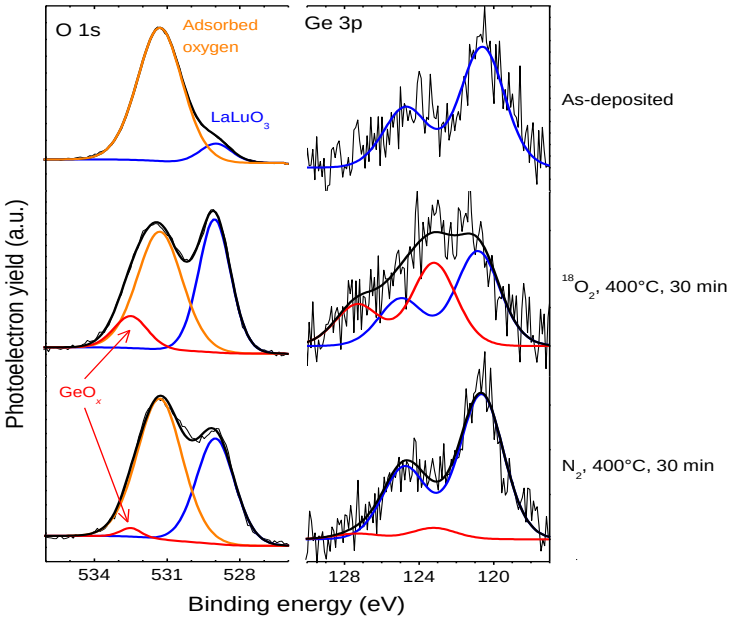

Figure 3. O 1s and Ge 3p regions of XPS spectra corresponding to $LaLuO_3$/Ge structures as deposited (top) and submitted to annealing as shown. The energy position of the components used in the fitting procedure of both regions is indicated; a.u. stands for arbitrary units.

In summary, $LaLuO_3$ films deposited on Ge substrates underwent different PDAs. Depending on the parameters (time and temperature) and mostly on the annealing atmosphere, different electrical characteristics of the resulting MOS structure are obtained. Annealing in oxygen results in Ge substrate oxidation, degrading interfacial characteristics. Annealing in N_2 was more beneficial because it promotes the formation of interfacial compounds responsible for substrate passivation ($LaGeO_x$) without the formation of oxidized Ge species responsible for electrical degradation.

References

1. R. M. Wallace, P. C. McIntyre, J. Kim, and Y. Nishi, MRS Bull. **34**, 493 (2009).
2. G. Mavrou, S. Galata, P. Tsipas, A. Sotiropoulos, Y. Panayiotatos, A. Dimoulas, E. K. Evangelou, J. W. Seo, and Ch. Dieker, J. Appl. Phys. **103**, 014506 (2008).
3. J. M. J. Lopes, M. Roeckerath, T. Heeg, E. Rije, J. Schubert, S. Mantl, V. V. Afanas'ev, S. Shamuilia, A. Stesmans, Y. Jia, et al., Appl. Phys. Lett. **89**, 222902 (2006).
4. E. H. Nicollian and J. R. Brews, MOS Technology, John Wiley & Sons, New York (1982).
5. J. R. Hauser and K. Ahmed, AIP Conf. Proc. **449**, 235 (1998).
6. G. Battistig, G. Amsel, E. d'Artemare, and I. Vickridge, Nucl. Instrum. Methods Phys. Res. B **66**, 1 (1992).
7. K. Kita, S. Suzuki, H. Nomura, T. Takahashi, T. Nishimura, and A. Toriumi, ECS Trans. **11**, 461 (2007).
8. J. P. Espinós, A. R. González-Elipe, and J. A. Odriozola, Appl. Surf. Sci. **29**, 40 (1987).
9. J. M. J. Lopes, M. Roeckerath, T. Heeg, J. Schubert, U. Littmark, S. Mantl, A. Besmehn, P. Myllymäki, L. Niinistö, C. Adamo, et al., ECS Trans. **11**, 311 (2007).

A complete version of the manuscript was published in Electrochemical and Solid State Letters 13 (5): G37 (2010).

Deuterated amorphous carbon films: film growth and properties

M.E.H. Maia da Costa and F.L. Freire Jr.

Departamento de Física, Pontifícia Universidade Católica do Rio de Janeiro, 22451-900, Rio de Janeiro, RJ, Brazil

Abstract

Deuterated amorphous carbon films (DLC) have been studied in the last few years in order to investigated possible isotopic effects in the film properties. When compared with films deposited in methane atmosphere, an important reduction of the deuterium content of the films was observed and the reasons for that are not well understood. In this work, we deposited amorphous carbon films by PECVD using methane and deuterated methane gas mixtures as precursor atmospheres. The hydrogen and deuterium content was measured by elastic recoil detection analysis and we observed the preferential incorporation of hydrogen over deuterium. The precursor atmosphere was monitored by mass spectrometry and only small differences can be observed in the obtained mass spectra. The possible reasons for the total hydrogen content are discussed.

Introduction

Diamond-like carbon (DLC) films have attracted much attention due to their outstanding physical and chemical properties [1]. DLC can be defined as an amorphous carbon material, that can be hydrogenated (a-C:H) or not (a-C), with a significant fraction of sp^3 carbon-bonds and with high mechanical hardness and wear resistance, chemical inertness and low friction. The properties of films, which are closely related to their microstructure, can be tuned by the deposition technique employed and by the growth conditions, with the energy of the impinging species playing the main role in the control of the film properties [1-3]. Deuterated amorphous carbon films (a-C:D) deposited by plasma assisted chemical vapor deposition (PECVD) using deuterated hydrocarbons as precursor gases were also investigated for some specific applications, like storing ultra cold neutron devices [4] or as neutron mirror [5]. In order to tailor the film properties in a controlled way, a fundamental understanding of the microscopic deposition process is necessary. Among the several aspects that need to be clarified, the preferential incorporation of hydrogen over deuterium in amorphous carbon films deserves investigation.

Experimental procedures

Amorphous hydrogenated carbon films (a-C:H) were deposited by plasma enhanced chemical vapor deposition (PECVD) with CH_4-CD_4 mixtures as precursor gas employing an asymmetrical capacitively coupled deposition system. Silicon substrates were mounted on a water-cooled copper cathode fed by a rf power supply. The films were deposited with a total pressure of 8 Pa and total incoming gas flux of 10 sccm up to a thickness of about 400 nm. Details of the deposition procedure can be found elsewhere [6]. The self-bias voltage (V_B) was fixed at -350 V and the CH_4 partial pressure varied from 100% (a-C:H films) to 0% (deuterated carbon films, a-C:D). A quadrupole mass analyzer was installed in the deposition chamber connected through a 1 mm diameter collimator. The region between the collimator and the quadrupole mass analyzer was pumped by a turbomolecular pump with pumping speed of 55 l/s for H_2.

The chemical composition was determined by Rutherford backscattering spectrometry (RBS) and ERDA employing a 4 MV Van de Graaff accelerator to produce a 2 MeV $^4He^+$ beam. For RBS the particle detector was positioned at 165° with respect to the incident beam, while for ERDA measurements the detector was positioned at 30°. The sample was tilted by 75° with respect to the incident beam. The atomic density was inferred by combining the areal atomic density (at/cm^2) provided by RBS and ERDA and the thickness obtained by stylus profilometry.

Results and discussions

Elastic recoil detection spectra obtained from different films are presented in fig. 1. The spectra show that both H and D concentrations are constant throughout the film.

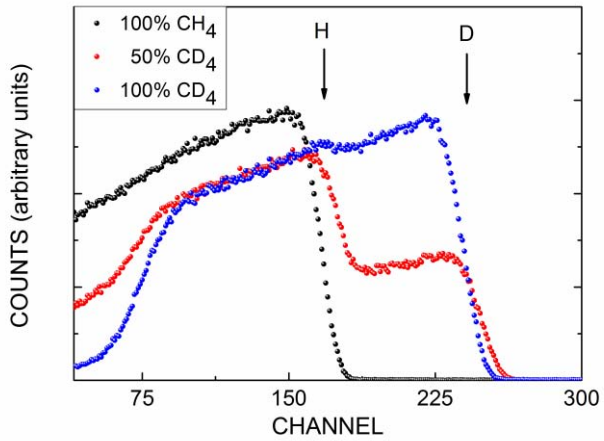

Figure 1: Elastic recoil detection spectra obtained from a a-C:H film; a-C:D film and an a-C:H:D film deposited by PECVD with CD_4-CH_4 gas mixture as precursor atmosphere. The positions of H and D when they are at the sample surface are indicated by arrows.

The atomic density, the deposition rate, the hydrogen and deuterium concentrations are presented in Table I. Absolute hydrogen and deuterium concentrations were obtained using the accurate measurements of the absolute cross sections for elastic recoil of H and D using low-energy $^4He^+$ beams [7]. The results for the absolute H or D concentrations quoted in the literature show a large deviation that is usually higher than the errors stated by the experimentalists [8]. In this work, more relevant than the absolute value are the relative errors for the ratio between the hydrogen and deuterium cross sections that are ±2% [7].

Precursor gas mixture	Atomic concentration (at.%)		Atomic density (1023 atoms/cm3)
	D	H	
100 % CH4	-	22	1.3
75% CH4 + 25% CD4	5	15	1.3
50% CH4 + 50% CD4	8	11	1.3
25% CH4 + 75% CD4	11	7	1.3
100 % CD4	17	-	1.3

Table I: Atomic density and hydrogen and deuterium concentration measured by nuclear techniques as functions of the precursor gas mixture and the self-bias voltage

Our data confirm previous results and show an important preferential incorporation of H over D [9]. In fact, in our experimental conditions, hydrogen concentration in an a-C:H film is 18% higher than deuterium concentration in a-C:D films. The same is observed in a film deposited using a 50:50 mixture of CD_4 and CH_4. One of the possible explanations for these results was presented by Johnson and collaborators [10]. They attributed the preferential incorporation of H to the different pumping speeds for the different molecules when turbomolecular pumps are used since they are more efficient for heavier molecules. In order to compensate this effect higher flow ratios for CD_4 can be used. However, our chamber is pumped by a diffusion pump and the differences in the pumping speeds are minimal for this range of molecular weight.

Differences in deuterium plasma chemistry can also be responsible for the differences in the incorporation of H and D, but there are few available experimental data [10]. In order to bring new information to this subject, we monitored the precursor atmosphere by mass spectrometry during the film deposition. The mass spectra are presented in fig. 2 for several CD_4-CH_4 mixtures. The spectra show a small peak at mass 2 (4) due to H_2 (D_2), a group due to CH_4 (CD_4) and its fragments around mass 16 (20) and a third group at around 28 (32) attributed to C_2H_n (C_2D_n) at around mass 28 (32). The same relative intensity between the second and the third group is observed for all CD_4-CH_4 mixtures. The mass spectra were also measured without power applied to the cathode. The spectra are similar than those shown in fig. 2 with some differences: the peak due to H_2 (D_2) is bellow the detection limit of our quadrupole analyzer and the intensity of the peaks attributed to C_2H_n (C_2D_n), when we normalized the spectra by the mass 16 peak, are much smaller than one can observe in fig. 2. The mass spectra did not indicate any isotopic effect during deposition. In fact, the intensities of C_nH_m or C_nD_m radical peaks observed in the mass spectra can be directly correlated with the partial pressure in the precursor atmosphere of methane or deuterated methane,

respectively. The same was observed for the peaks corresponding to mass 2 and 4. These results also support the statement made above that there is no preferential pumping of deuterated species over hydrogenated ones in our deposition system.

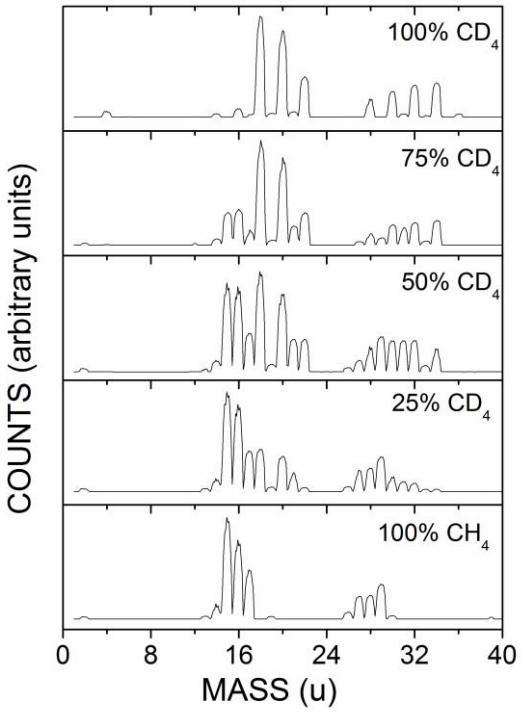

Figure 2: Mass spectrum obtained during film deposition by PECVD (8Pa, -350V) with different precursor atmosphere, as indicated in the figure.

The preferential incorporation of H over D can be attributed to an enhancement of the dehydrogenation process when deuterium is involved, favoring the loss of the heaviest isotope. The energy of the plasma is sufficient to allow subplantation of hydrogen ions, which have enough kinetic energy to modify the subsurface by removing bonded hydrogen. For the same V_B, both D and H ions will have the same kinetic energy, but probably, a shallower modified layer will be found in a-C:D films resulting in a more efficient hydrogen species removal during deposition, explaining at least partially, the less efficient D incorporation.

The film atomic density is, within our experimental errors (±10%), independent on the precursor gas used. The deposition rates for films deposited at different gas mixtures are also measured and a progressive reduction on the deposition rate was observed for films deposited in CD_4 richer plasma atmospheres. The differences in deposition rate suggest that films with different microstructure were formed.

Conclusions

We deposited a-C:D, a-C:D:H and a-C:H films by PECVD using methane and deuterated methane mixtures as precursor atmospheres. We measured the hydrogen and deuterium content in the films and verify the preferential incorporation of hydrogen over deuterium. In our experimental conditions, both the purity of the precursor gas and effects of the pumping system can be discarded as possible reasons for this result. We suggested that it can be attributed to a more efficient dehydrogenation process when deuterium is present in the plasma atmosphere and favoring the desorption of the heaviest isotope.

Acknowledgements

This work was partially supported by the Brazilian agencies, CNPq and FAPERJ.

References

1. J. Robertson, Mater. Sci. Eng. R 37 (2002) 129.
2. P. Lemoine, J.P. Quinn, P.D. Maguire, J. A. McLaughin, in Tribology of Diamond-like Carbon Films, ed. by C. Donnet and E. Erdemir (Springer, New York, 2008) p.83
3. F.L. Freire Jr., in Carbon: The Future Material for Advanced Technology, ed. by. G. Messina and S. Santangelo, Topics in Applied Physics Vol. 10 (Springer-Verlag, Berlin 2006) p. 217.

4. M.G.D. van der Grinten, J.M. Pendlebury, D. Shiers, C.A. Baker, K. Green, P.G. Harris, P.S. Iaydjiev, S.N. Ivanov, P. Geltenbort, Nucl. Instr. and Meth. A 423 (1999) 421.
5. Y. Kawabata, M. Hino, T. Horie, S. Tasaki, K. Yoshida, I. Kanno, M. Nakayama, Nucl. Instr. and Meth. A 529 (2004) 84.
6. L.G. Jacobsohn, G. Capote, N.C. Cruz, A.R. Zanatta, F.L. Freire Jr., Thin Solid Films 419 (2002) 46.
7. V. Quillet, F. Abel, M. Schott, Nucl. Instr. and Meth. B 83 (1999) 47.
8. R. Berisch et al, J. Nucl. Mater. 281 (2000) 42.
9. N. Mathias, C. Meunier, F. Munnik, S. Mikhailov, Thin Solid Films 516 (2008) 1508.
10. J.A. Johnson, J.B. Woodford, X. Chen, J. Andersson, A. Erdemir, G.R. Fenske, J. Appl. Phys. 95 (2004) 7765.

A complete version of the manuscript was published in Surface and Coatings Technology 204 (2010) 1993.

Effect of hydrogen on plasma oxidation of ferrous alloys

A.C. Rovani,[a] R. R. Fischer,[a] F. Cemin,[a] F. G. Echeverrigaray,[a] R. L. O. Basso,[a] C. L. G. Amorim,[a] G. V. Soares,[a,b] I. J. R. Baumvol,[a,b] and C. A. Figueroa[a,*]

[a] Centro de Ciências Exatas e Tecnologia, Universidade de Caxias do Sul, Caxias do Sul, 95070-560, Brazil
[b] Instituto de Física, Universidade Federal do Rio Grande do Sul, Porto Alegre, 91509-970, Brazil

Abstract

The effect of hydrogen on plasma post-oxidation, following plasma nitriding of a ferrous alloy was investigated. The increase of the hydrogen concentration in the plasma reduces progressively the hematite/magnetite concentration ratio in the outermost oxide layer down to zero at 25% H_2 concentration. Atomic hydrogen originated from scission of hydrogen molecules in the plasma leads to reduction of Fe(III) in hematite into Fe(II) in magnetite by controlling the gas mixture reduction potential.

Introduction

Hydrogen is a versatile chemical agent which is widely used in plasma surface engineering. For example, the addition of hydrogen in plasma nitriding increases the nitrogen ionization [1]. Moreover, hydrogen is added for cleaning purposes due to its chemical reduction properties. Thus, atomic hydrogen ions are reactive species leading to control the surface oxide content in ferrous alloys under plasma treatments. Indeed, hydrogen increases the reduction potential of the gas mixture in the plasma, decreasing the oxygen content in ion nitriding of austenitic stainless steels [2,3].

Plasma nitriding followed by post-oxidation is a good candidate as replacement for chromium electroplating and salt and gas oxidation techniques, due to environmental-friendly aspects and technical quality reasons. The combination of a hard and wear resistant underneath nitrided layer and a corrosion resistant and low friction outermost oxide layer provides a high performance mechanical system for hydraulic and automotive applications [4]. It is well known that the hematite phase (α-Fe_2O_3) is porous and brittle [4], while the magnetite phase (Fe_3O_4) is compact and homogenous, two important technical characteristics for corrosion resistance and low friction coefficient [5]. Hence, the formation of a hematite free oxide layer is the aim of any plasma post-oxidation process.

Experimental

Samples from the same AISI 1045 plain steel source were used for the study. Nitriding was performed in a laboratory-scale chamber. The gas total pressure was kept at 92 Pa and the gas mixture was fixed at 90% N_2 -10% H_2 during the nitriding process. The substrate temperature during nitriding was maintained at 550 +/- 2 °C during 5 hours. Following nitriding, post-oxidation was performed in the same chamber, without open it to air. The total gas pressure was kept at 112 Pa, the gas mixture was a fixed N_2/O_2 ratio of 7, and the H_2 proportion was varied from 0 to 25%. The post-oxidation temperature was maintained at 510 +/- 2 °C during 45 minutes. The crystalline structures of plasma modified layers were determined by X-ray diffraction (XRD). Cross-section micrographs of nitrided and oxidized layers were recorded using a Shimadzu SSX-550 scanning electron microscope. The chemical bonds in the plasma modified surfaces were characterized by X-ray photoelectron spectroscopy (XPS). These measurements were performed in an Omicron SPHERA station using Mg-K_α radiation (1253.6 eV) at a take-off angle of 60° with an energy resolution of 0.9 eV.

Results and Discussion

The XRD patterns in Bragg-Brentano geometry are shown in Figure 1 for samples obtained by plasma post-oxidation at different H_2 concentrations after plasma nitriding. For comparison purposes, the diffractogram of the nitrided samples without post-oxidation is also included at the bottom. The diffraction patterns can be assigned to a mixture of iron nitrides such as γ-Fe_4N and ε-$F_{2-3}N$, iron oxides such as α-Fe_2O_3 (hematite) and Fe_3O_4 (magnetite), as well as the original α-Fe (ferrite). Moreover, one can see that for increasing hydrogen concentrations, the intensity of the peaks located at 24.2 and 33.2 degrees, assigned here to hematite, decreases with respect to those assigned to magnetite, from a significant contribution at 0% H_2 to almost vanishing completely at 25 % H_2. For the sake of clearness, the inset in Fig. 1 shows the range between 2θ = 22 to 38 degrees where the characteristic peaks for hematite and magnetite are stressed [6]. Furthermore, GAXRD (not shown) confirms that the outermost layer (approximately 800 - 900 nm) is formed only by the iron oxides mentioned above. Fig. 2 shows the intensity ratio I_{104}/I_{100} as a function of the hydrogen concentration where the planes (104) and (100) are assigned to hematite and magnetite pure phases, respectively. The dashed line is only to guide the eyes. This intensity ratio decreases to almost 0 at 25 % hydrogen content. Hence, the oxide layer obtained in such condition is constituted only by the magnetite phase. In addition, photos of samples post-oxidized at 0% H_2 and 25% H_2 are presented as an inset in

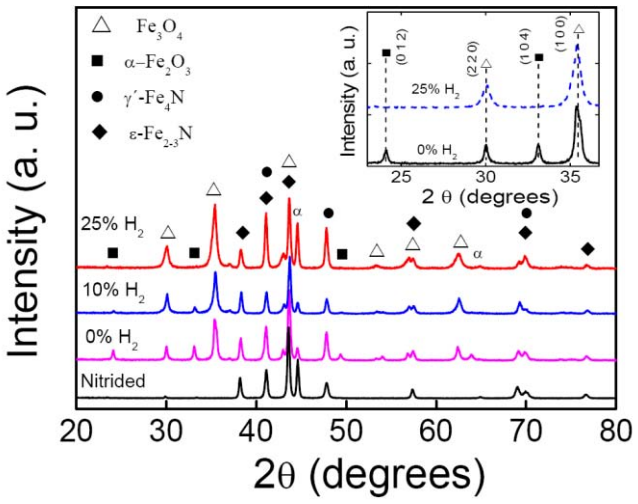

Fig. 1. Bragg-Brentano X-ray diffractograms from samples obtained by plasma post-oxidation at different H_2 concentrations after plasma nitriding. For comparison purposes, the diffractogram of the nitrided samples without post-oxidation is also included at the bottom. The inset shows the range between 2θ = 22 to 38 degrees for two samples treated at 0% and 25% H_2.

Fig. 2 One notices the different visual aspects between both extreme conditions, where a non-homogenous dark blue tone is observed on the surface of the sample post-oxidized at 0% H_2 in contrast with a homogenous black tone on the surface of sample treated at 25% H_2 (hematite free). Scanning electron microscopy confirms that the thickness of both nitrided and oxide layers (not shown) remain the same as the hydrogen concentration varies.

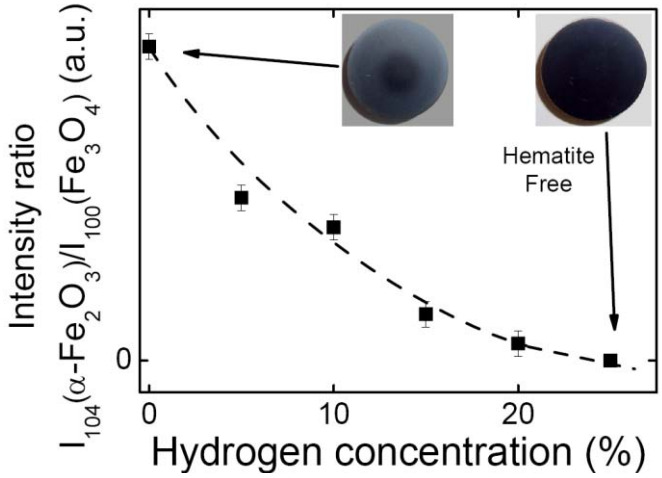

Fig. 2: XRD I_{104}/I_{100} intensity ratio, assigned to hematite and magnetite pure phases, respectively, as a function of hydrogen concentration. The dashed line is only to guide the eyes. Also, the sample surface characteristics are shown after plasma post-oxidation treatments at 0% and 25% H_2.

Figure 3a and 3b show the Fe2p$_{3/2}$ and O1s photoelectron regions, respectively, at two characteristic hydrogen concentrations. The Fe2p$_{3/2}$ photoelectron regions (Figure 3a) indicate the presence of Fe(II) and Fe(III) bonds in iron oxides and $Fe(OH)_3$ (iron hydroxide) contributions in the oxide layer. It is clearly seen that the main peak does not change either in position or intensity for different H_2 concentrations in the plasma. However, the Fe(III) satellite peak at a binding energy of 717 eV that corresponds to hematite [7], decreases drastically when the hydrogen concentration in the plasma changes from 0 to 20 % H_2. According to these authors, no evidences of such satellite appear when pure magnetite is analyzed. Moreover, Figure 3b shows a shift of the components of the O1s photoelectron regions to higher binding energies for increasing hydrogen concentrations. This corroborates the previous results, since O binding energies are higher for magnetite than for hematite [8, 9]. XPS provides information of 7 to 10 nm below the sample surface, whereas it would be desirable to have information on far more deeper regions of the sample. However, this complementary technique entirely corroborates the present XRD results, which inspect much deeper layers.

Thus, the addition of hydrogen reduces Fe(III) ions in the oxide layer, transforming the hematite phase into magnetite phase. In the absence of a plasma, when only hydrogen molecules are present, the reduction of Fe(III) in hematite to Fe(II) in magnetite is not spontaneous. Indeed, we estimated the Gibbs free energy in this case as being $\Delta G = +227$ kJ.mol^{-1} at 500°C [10, 11]. On the other hand, scission of hydrogen molecules into atomic hydrogen in the plasma does have sufficiently

negative Gibbs free energy to reduce Fe(III) into Fe(II). In this last case, our estimation gave $\Delta G = -158$ kJ.mol^{-1} at 500°C (spontaneous process). Thus, the presence of atomic hydrogen is mandatory in order to eliminate the hematite phase in plasma post-oxidation processes by achieving a sufficient gas mixture reduction potential. This easy control of such a duplex process that yields the formation of a hematite free oxide layer on nitrided surfaces could open new possibilities for establishing an environmental-friendly plasma process instead of toxic and less controlled techniques like chromium electroplating and gas oxidation, respectively, in surface engineering of ferrous alloys.

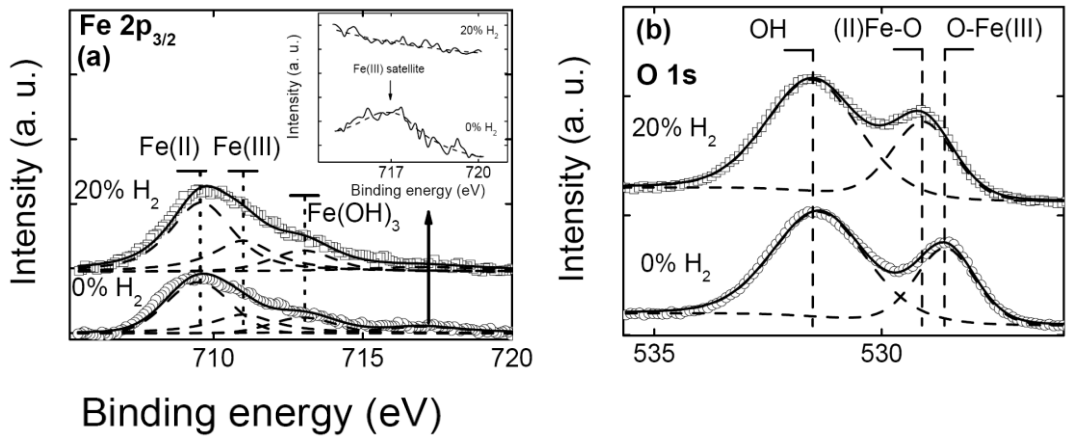

Fig. 3a and 3b show the Fe2p$_{3/2}$ and O1s photoelectron regions, respectively, at two characteristic hydrogen concentrations. The inset in fig. 3a shows the Fe(III) satellite peak at a binding energy of 717 eV that corresponds to hematite.

Conclusions

In conclusion, atomic hydrogen can act as a chemical agent in order to produce a hematite free iron oxide layer in pulsed plasma post-oxidation following plasma nitriding of ferrous alloys. The gas mixture reduction potential must be controlled and the presence of atomic hydrogen is mandatory to render spontaneous the reduction of Fe(III) in hematite to Fe(II) in magnetite. This versatile and environmental-friendly process could open new possibilities for replacing chromium electroplating and gas oxidation treatments.

Acknowledgment

This work was partially sponsored by CNPq: projects # 573628/2008-4 (INCT) and # 550316/2007-8 (Young Researcher). CAF and IJRB are CNPq fellows.

References

1. H. Michel, T. Czerwiec, M. Gantois, D. Ablitzer, A. Ricard, Surf. Coat. Technol. 72 (1995) 103.
2. C.A. Figueroa, S. Weber, T. Czerwiec, F. Alvarez, Scipta Materialia 54 (2006) 1335.
3. C.A. Figueroa, F. Alvarez, Surf. Coat. Technol. 200 (2005) 498.
4. F. Mahboubi, M. Fattah, Vacuum 79 (2005) 1.
5. M. Zlatanović, N. Popović, Ž. Bogdanov, S. Zlatanović, Surf. Coat. Technol. 177-187 (2004) 277.
6. C.A. Figueroa, E.E. Sileo, P.J. Morando, M.A. Blesa, J. Colloid Interface Sci. 225 (2000) 403.
7. T. Kendelewicz, P. Liu, C.S. Doyle, G.E. Brown Jr., Surf. Sci. 469 (2000) 144.
8. G.C. Allen, M.T. Curtis, A.J. Hooper, P.M. Tucker, J. Chem. Soc. Dalton Trans. 1525 (1974).
9. J. Haber, J. Stoch, L. Ungier, J. Electron Spectrosc. Relat. Phenom. 9 (1976) 459.
10. R.D. Ride, Handbook of Chemistry and Physics, 85th ed., LLD, Boca Raton, 2005.
11. W.P. Tong, N.R. Tao, Z.B. Wang, J. Lu, K. Lu, Science 299 (2003) 686.

A complete version of the manuscript was published in Scripta Materialia 62 (2010) 863.

Nitriding in Cathodic Cage of Stainless Steel AISI 316: Influence of the Sample-Cage Walls Distance

C. Alves Jr [1], R.R.M. de Sousa [2], F.O. de Araújo [3], J.A.P. da Costa [4], T. Dumelow [4], R. S. de Oliveira [5]

Departamento de Engenharia Mecânica – UFRN
Instituto Federal do Piaui
Universidade Federal Rural do Semi-árido
Universidade do Estado do Rio Grande do Norte
Instituto Federal do Rio Grande do Norte

Abstract

The aim of this work is to perform a systematic study about sample position influence of a new plasma nitriding process called cathodic cage plasma nitriding (CCPN). It was studied the nitrided layers properties as function of the distance between cage wall and samples. In this technique the samples are kept on floating potential, inside a cage, that acts as a cathode and shields the samples from the cathodic potential. Cylindrical austenitic stainless steel AISI 316 samples were placed in different positions on the alumina plate inside the cathodic cage. The nitrided samples were characterized by optical microscopy, x-rays diffraction and microhardness measurements. The results shows that for samples near wall cage exhibit higher layer thickness This results must be due to compromise between mean path free and sputtering rate that changes in the depositon rate depending on how far the samples surface are from the cage walls.

Introduction

All kinds of stainless steel are of great use in engineering due to their high corrosion resistance, although they process low were resistance and reduced hardness. These two last properties are significantly improved through ionic plasma nitriding [2-4]. As it is well known, when the nitriding of austenitic stainless steel is carried out at temperatures higher than 723 K it produces layers of high were resistance and surface hardness, while the corrosion resistance decrease significantly due to precipitation of chromium nitride, with a consequent reduction of the chromium content in the matrix. In contrast, when the nitriding is carried out at temperatures lower than 723 K a supersatured phase with nitrogen is formed which is called expanded austenitic or S-phase, which possess high hardness and were resistance besides a great resistance to corrosion [5,6]. It is observed that in the conventional nitriding process, called direct current plasma nitriding (DCPN), the nitriding layer is not uniform because edge effect and area to volume ratio. We show that this effect there is not occurring in the cathodic cage plasma nitriding [1]. It was also observed that in this process, nitriding layers with properties as good as layers obtained by DCPN, but with some improvements, such as bigger thickness, better uniformity, higher hardness and the elimination of the so called border effect [1,9]. In this study the objective is to identify the influence of the sample position inside the cage on the nitriding layers properties.

Materials and methods

The material used in this study was austenitic stainless steel 316, supplied by the Villares Metals Co., annealed (hardness 240 HV).

The stainless steel AISI 316 samples were machined in cylindrical form, 8 mm x 8 mm (diameter x height) previously annealed, grounded with 320, 400, 600 and 1200 mesh grinding papers and polished on a felt disc with 1,0 and 0.3 µm diamond suspensions. They were then ultrasonically cleaned in an acetone bath, before being placed into the nitriding chamber. The nitriding system consists of a power source (maximum tension 1500 V, current 2A), a cylindrical stainless steel vacuum chamber (Figure 1) with 40 cm in diameter and 40 cm in height. A stainless steel cathodic cage with 112 mm diameter and 25 mm height was placed on the cathode. The cage has holes with diameter of 8 mm, 9.2 mm distance between centers and 0.8 mm thickness.

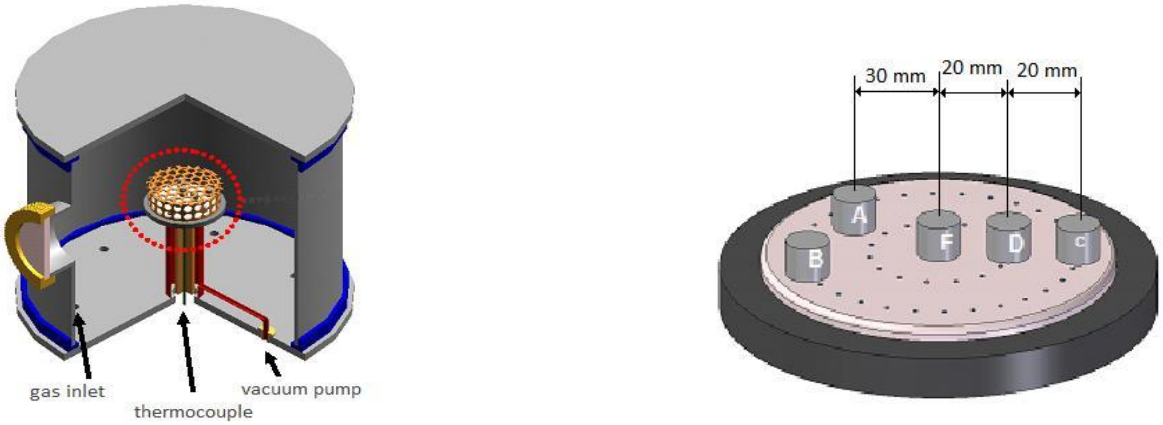

(a) **(b)**

Figure 1 – (a) The plasma nitriding reactor scheme and (b) spatial distribution of the samples

The samples were pre-treated in hidrogen for 20 minutes at a temperature of 573 K and pressure of 200 Pa in order to eliminate contaminants such as oxides and/or grease/fat adsorbed on the surface. After pre-treatment the samples were treated during 5 hours, at 723K for pressures of 120 and 250 Pa. The nitriding atmosphere mixture of (80% N_2/ 20% H_2) with a flow rate of 20 sccm, regulated with a mass flow controller manually adjusted. After the nitriding process the samples were cooled down slowly inside the chamber to a temperature of 353 K in order to prevent oxidation. Then they were prepared for metallography analysis and etched in a solution containing 50%HCl+25%HNO_3+25%H_2O (água régia) and Beraha II for microstructural .observation.

The composition and texture were analyzed using X-ray diffraction (XRD). The referred analysis were carried out using Cu*Ka* (wave length: 0.154 nm) and Mo-*Ka* (λ = 0.07094 nm) lines operated at 40 KV using a Shimadzu XRD-6000 instrument. An optical microscope (Olympus BX60M) and SEM (Philips, model XL 30 ESEM) were used to observe and measure the layer thickness and to evaluate its texture and uniformity. Microhardness measurement profiles were carried out on the top surface of the nitrided samples in order to evaluate uniformity of the layers.

Results and Discussion

The surface hardness and layer thickness measurements data for samples treated in different positions A_{30}, B_{40}, C_{40}, D_{20}, E_{center} (fig. 1b) under pressures of 120 and 250 Pa, are presented in table 2.

Table 2 – Layers thicknesses and microhardness of the nitride layers as a function of the work pressure and sample position inside the cage (5 h, 723 K and 80% N2+20% H2)

Presure [Pa]	Sample Position	Nitriding Layer Thickness [μm]	Microhardness [$HV_{0,1}$]
250	A_{30}	26,6	1175
	B_{40}	28,3	1216
	C_{40}	28,2	1115
	D_{20}	24,4	1305
	E_{center}	22,2	1213
120	C_{40}	61,9	978
	D_{20}	56,7	953
	E_{center}	51,4	931

This data show that samples treated by the cathodic cage technique under the lower pressure (120 Pa) develop nitrided layers thicker than the samples treated at the pressure of 250 Pa, as it was observed in previous study [1,7]. This can be explained assuming that both the deposition by sputtering as well as the mean path free of the active species produced on the cage walls and transferred to the sample surface, play important role in the overall process. For lower working pressure we have lower sputtering rate but long mean free path of the species from cage hole to the sample surface, increasing the deposition rate and resulting on thicker layers compared to the higher pressure. This value also is higher than DCPN, contributing to idea that in the CCPN the deposition is the predominant process and overall species deposited on the sample surface are not subsequently sputtered from it. It was observed that in DCPN, for a nitriding temperature of 723 K, the growth rate of nitride layer is 3.0 μm/h [11] while in CCPN this value is between 12.0 μm/h (150 Pa) and 5.0 μm/h (250 Pa). Comparing the nitride layer thickness for sample at different position it can be observed (Table 1) that there is a light increase in the layers thickness for the samples placed in positions B_{40} and C_{40} (the nearest the cage wall) produced by the superposition of the species flow originated on the top and lateral cage walls.

The micrograph for the samples nitrided under a pressure of 250 Pa (fig. 2) shows some difference concerned with dark and white regions in the nitride layer especially when we compare the layer formed in the sample placed on the position E_{center} with the others. For this sample the micrography presents white regions what is an indication of the presence of phase-S (expanded austenite) whereas, for example, for the sample placed on position A the micrography presents almost only dark regions, what suggest the presence of nitrites.

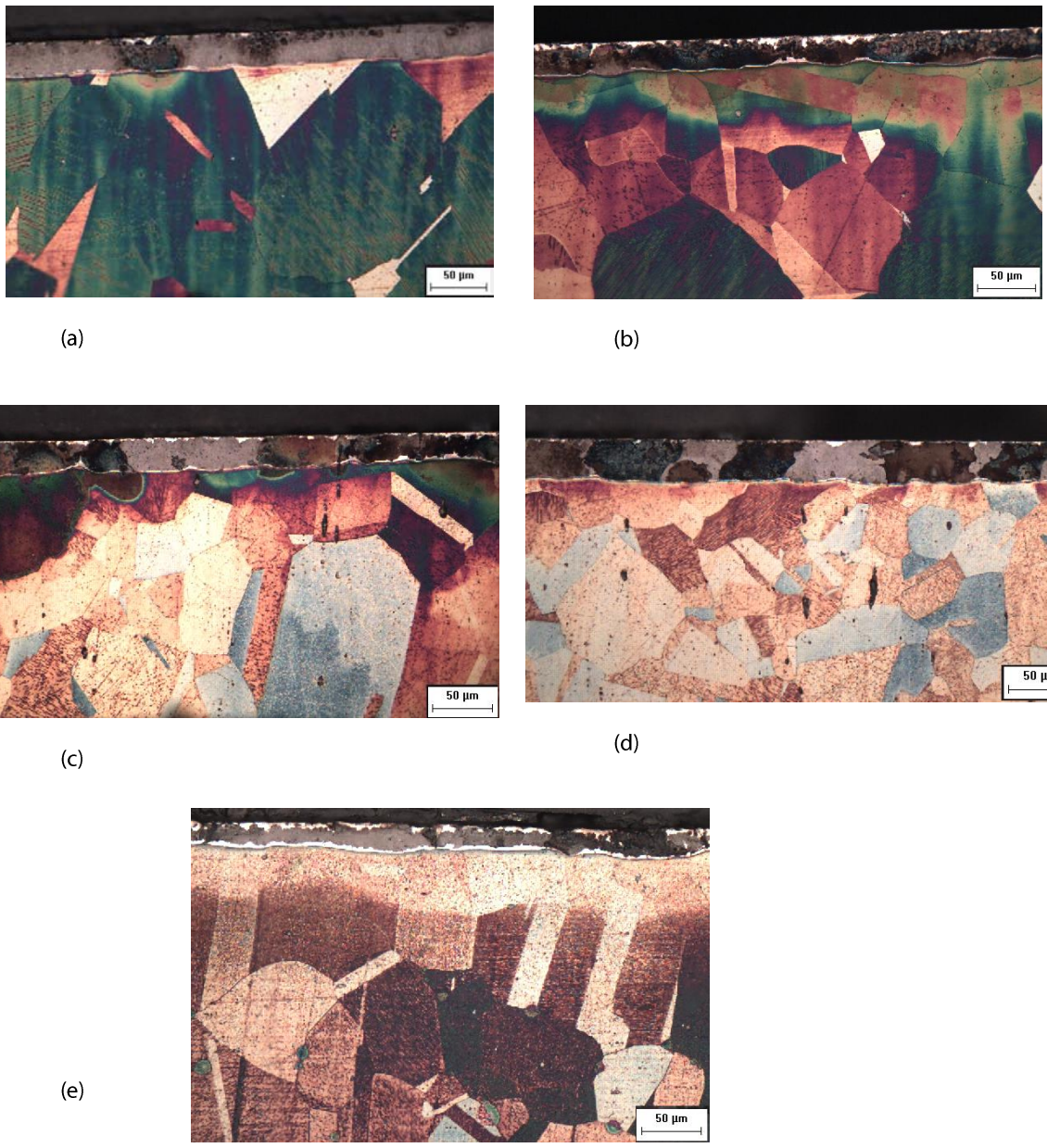

(a) (b)

(c) (d)

(e)

Figure 2 – Micrographs of samples treated under a pressure of 250 Pa at temperatures of 723 K during 5 hours placed at different radial positions 30 mm (a), 40 mm (b), 40 mm (c), 20 mm (d) e center (e).

The X-ray diffractograms presented in figure 3 show that for the samples of larger thickness layers (B_{40},C_{40}) there is a predominance of iron nitrites [12], what confirm the the micrograph analisys, and should be caused by the fact that the nitriding species reach the sample surface with larger energy and intensity, since they are originated in the cathodic cage walls, which are very close to the sample surface.

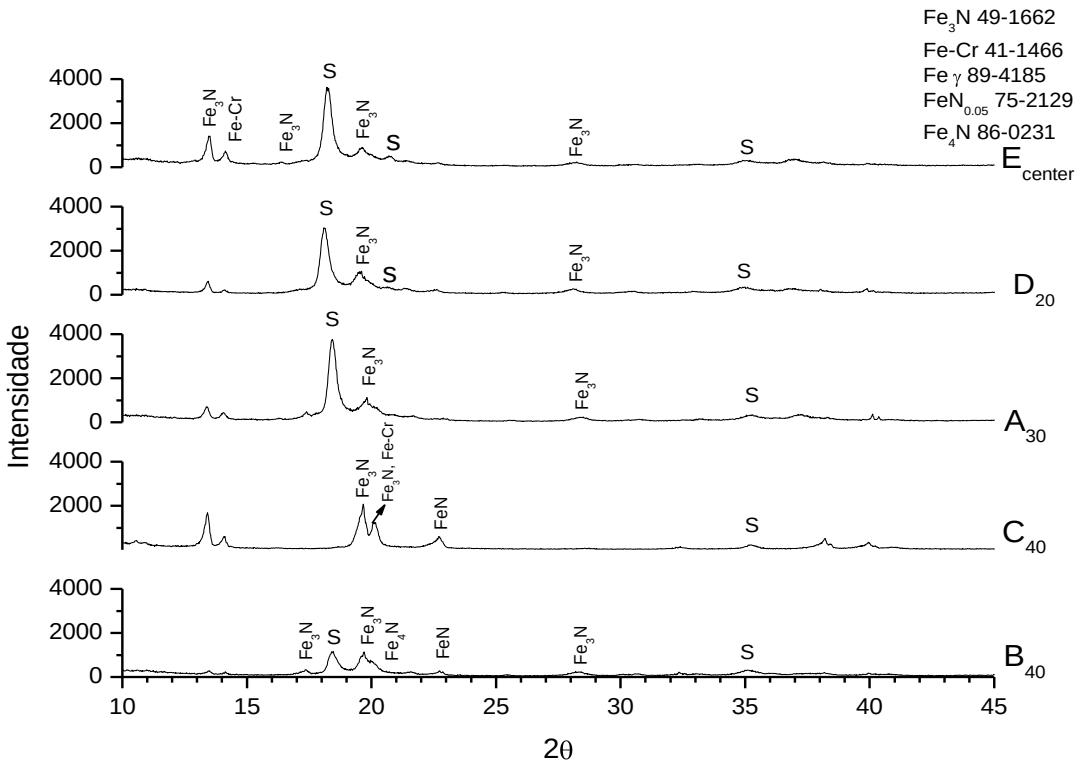

Figure 3 – X-ray difractograms [Mo-*Kα* (λ = 0.07094)] for samples nitrided at 723K, during 5 hours under a pressure of 250 Pa, placed at different positions inside of the cathodic cage.

The micrographs of samples treated under the pressure of 120 Pa (fig. 4) shows nitrided layers do totally dark in contrast with the samples nitrided under the pressure of 250 Pa, what means that the expanded austenite is absent. This fact is confirmed by the X-ray analysis (fig. 5) and this is probably responsible for the systematic reduction in the surface hardness (table 1), when compared with the samples treated under the pressure of 250 Pa.

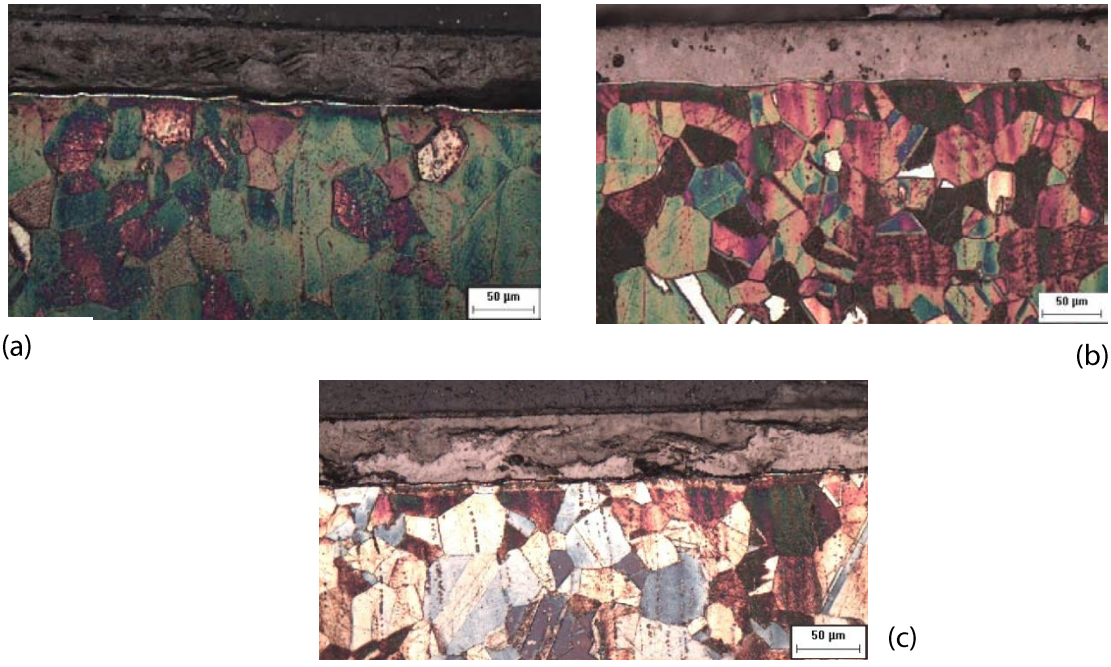

Figure 4 – Micrographs of samples treated under pressure of 120 Pa at the temperatures of 723 K during 5 hours placed on different positions (a) C_{40}, (b) D_{20} e (c) E_{center}.

The difractograms presented in figure 5, for samples nitrided at a pressure of 120 Pa and at a temperature of 723 K, placed on different positions, inside of the cathodic cage, are nearly the same. Moreover, they do not present characteristic

peaks of phase-S and it do not present intensity variation for the peaks characteristics of iron nitrite [γ' – Fe_4N]. This is an indicative that does not exist thermal gradient in the interior of the cathodic cage, since any increase in the treatment temperature should causes an increase of the intensity of the peaks of iron nitride, γ' – Fe_4N [13].

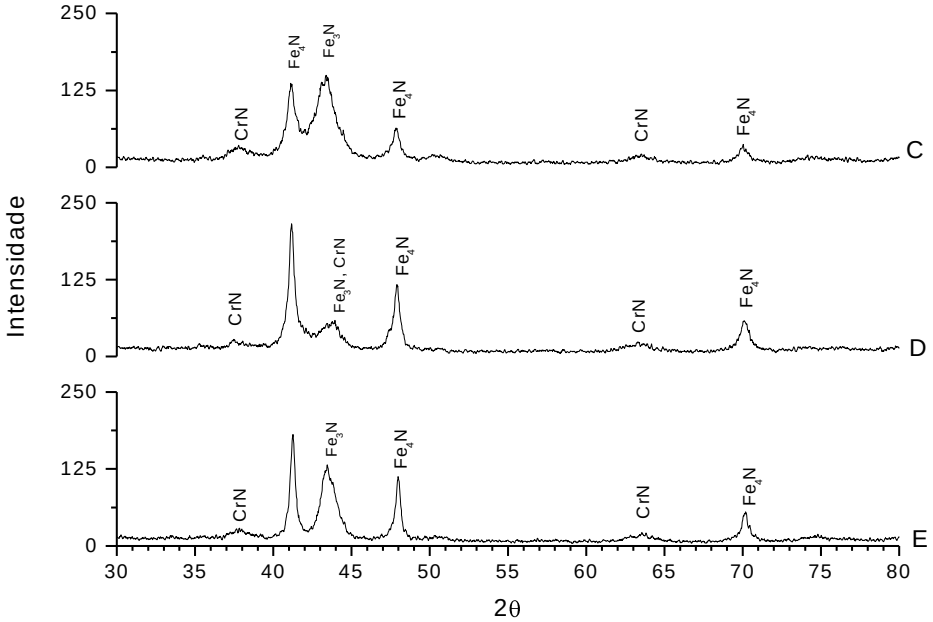

Figure 5 – X-ray difractograms for samples nitrided at 723K, during 5 hours under a pressure of 250 Pa, placed at different positions (C_{40}, D_{20}, E_{center}) inside of the cathodic cage.

Conclusions

Samples nitrided at lower pressure (120 Pa) present ticker nitrided layers than at higher pressure (250 Pa). A probable explication for this is because the mean free path of the particles from hole to sample surface is higher.

The growth rate of nitrided layer in this process is higher than in DCPN for both (150 Pa and 250 Pa) pressure used in this work.

S-phase is only present for sample nitrided at 250 Pa and positioned near cage center (beween 0 and 30 mm). A probable explication for this is that the time for temperature decreasing is higher, resulting in S-phase formation.

The growth rate of nitride layer for samples near cage wall is higher than samples near center because in the first case the sum of the contributions of species from the top and sides of the cages is larger.

References

1. ALVES JR., C. at al, Use of cathodic cage in plasma nitriding, **Surface and Coatings Technology** 201 (2006) 2450-2454.
2. ZHANG, Z. L.; BELL. T., **Surface Engineering** 1 (2) (1995) 131.
3. MENTHE, E.; RIE, K.-T., **Surface and Coatings Technology** 116 – 119 (1999) 199C.
4. CHENG, ZHAO; LI, C. X.; DONG, H.; BELL, T., **Surface and Coatings Technology** 191 (2005) 195 – 200.
5. MENTHE, E.; BULAK, A.; OLFE, J. et al., **Surface and Coatings Technology** 133 – 134 (2000) 259 – 263.
6. LI, C.X.; BELL, T. Corrosion properties of active screen plasma nitrided 316 austenitic stainless steel, **Corrosion Science** 46 (2004) 1527 - 1547.
7. SOUSA, R.R.M.; ARAUJO, F.O.; RIBEIRO, K.J.B.; MENDES, M.W.D.; COSTA, J.A.P.; ALVES JR., Cathodic cage of samples with different dimensions, **Materials Science and Engineering A** 465 (2007) 223 – 227.
8. MACAK, E.D., MUNZ, W.D., RODEMBURG, J.M., Journal of Appl. Physics, 94 (2003) 2829-2836.
9. LI, C.X.; GEORGES,J.; LI, X. Y. Active screen plasma nitriding of austenitic stainless steel, **Surface Engineering** 18 (6) (2002) 453 - 458.
10. MOLLER, W.; PARASCANDOLA, S.; TELBIZOVA, T..; GÜNZEL, R.; RICHTER E., Surface processes and diffusion mechanisms of ion nitriding of stainless steel and aluminium, **Surface and Coatings Technology**, 136 (2001) 73-79.
11. DIMITROV, V.I.; D'HAEN, J.; KNUYT, G.; QUAEYHAEGENS, C.; STALS, L.M., A method for determination of the effective diffusion coefficient and sputtering rate during plasma diffusion treatment, **Surface and Coatings Technology** 99 (1998) 234 – 241.
12. BORGIOLI, F.; FOSSATI, A.; GALVANETTO, E.; BACCI, T.; PRADELLI, G., Glow discharge nitriding of AISI 316L austenitic stainless steel: influence of treatment pressure, **Surface and Coatings Technology** 200 (2006) 5505 – 5513.
13. SUN, Y.; LI, C.X.; BELL, T., X-ray diffraction characterization of low temperature plasma nitrided austentic stainless steels, **Journal of Materials Science,** 34 (1999) 4793 - 4802.

A complete version of this manuscript was published in Vacuum, v. 83, p. 1 (2009).

Diamond-like carbon deposited by plasma technique as a function of methane flow rate

G.A. Viana[a], E. F. Motta[a], M.E.H.M da Costa[b], F. L. Freire Jr.[b] and F.C. Marques[a]

[a] Instituto de Física Gleb Wathagin, Universidade Estadual de Campinas, 13083-970, Campinas, SP, Brazil, P.O. Box 6165
[b] Pontifícia Universidade Católica do Rio de Janeiro, Departamento de Física, 22453-970, Rio de Janeiro, RJ, Brazil

Abstract

In this work we investigate diamond-like carbon (a-C:H) prepared by plasma enhanced chemical vapor deposition (PECVD) as a function of methane gas flow rate, including films deposited at zero flow rate, i.e., without the use of vacuum pumps during the deposition. The deposition rate and film structure (investigated by Raman spectroscopy) depend on the methane gas flow rate. A maximum for deposition rate was found at methane flow much smaller than the flow usually adopted in conventional procedures.

Introduction

Diamond-like carbon (DLC) have been used in a number of application such as hard coating for tools, cold cathode electron emitters, micro-electro-mechanical systems **(**MEMS**)**, car parts and protective coating in hard disk drives. These applications are mainly associated with the high hardness and low friction coefficient of DLC [1-6]. One of the most used techniques is the plasma enhanced chemical vapor deposition (PECVD). In this technique, a continuous supply of methane gas is required to guarantee that the atmosphere be constant along the deposition. This procedure results in the waste of a considerable amount of methane gas to the atmosphere. In this work we investigated diamond-like carbon (a-C:H) prepared by PECVD in a wide range of methane gas flow rate, including films prepared at zero flow rate.

Experimental

The films were deposited in an ultra-high-vacuum system to reduce desorption of contaminating gases from the walls of the reactor chamber. In addition, the reactor chamber was baked for more than 10 hours at a temperature of about 120 ^{o}C and pumped down to about 10^{-8} torr. Films were then deposited by PECVD on the cathode electrode as a function of methane gas flow rate. For the deposition at zero flow, the chamber was closed and methane gas was introduced until the desired pressure was reached. Using this procedure, hydrogenated amorphous carbon (a-C:H) films with diamond-like structure were obtained. Micro-Raman scattering spectroscopy was carried out in air at room temperature in an Acton Research SpectraPro 500i analyzer, using the 488 nm Ar^{+} laser line with 10 nW emission power.

Results and Discussion

The deposition rate of the DLC films (Fig. 1) changes significantly in the methane flow rate range investigated. A maximum is found at a relatively low flow, 4 sccm, with deposition rate of about 50 % higher than in normal condition (10-40 sccm range). The increase in the deposition rate as the methane flow rate decreases from 80 sccm to about 4 sccm (Fig. 1), is related to an increase in the methane dissociation, which is supported by the work of Zhang and Catherine [7].

The reduction of the deposition rate for methane flow rate below 4 sccm is related to the enrichment of the atmosphere with H_2 molecules coming from the dissociation of methane. The use of low flow rate gives an expressive decrease in the amount of CH_4 consumed in the deposition. As can be observe in the inset of figure 1, the consumption of methane as a function of the flow rate can be reduced by about two orders of magnitude at 4 sccm, and by three orders of magnitude without pumping the reactor chamber during deposition. This represents a huge reduction of consumed gas, beside the beneficial effect to the environment.

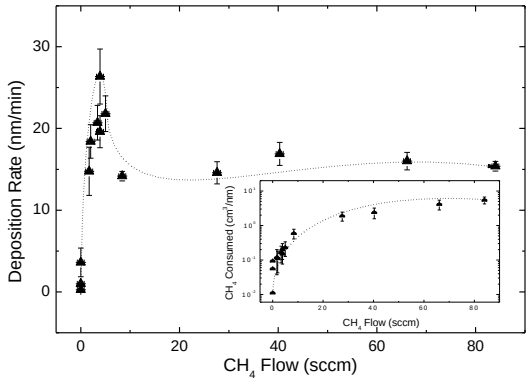

Figure 1 – Deposition rate of diamond-like carbon films deposited by PECVD as a function of methane flow. The inset shows the consumption of methane in the same flow range.

Figure 2 shows the concentration of hydrogen as a function of the methane flow obtained from the integrated area of the C-H stretching mode (in the 2800 -3100 cm^{-1} frequency range, determined by FTIR). It is observed that the concentration increases as the methane flow decreases. This effect must be related to the increase in the partial pressure of H_2 in the atmosphere, promoted by the reduction of the pumping speed.

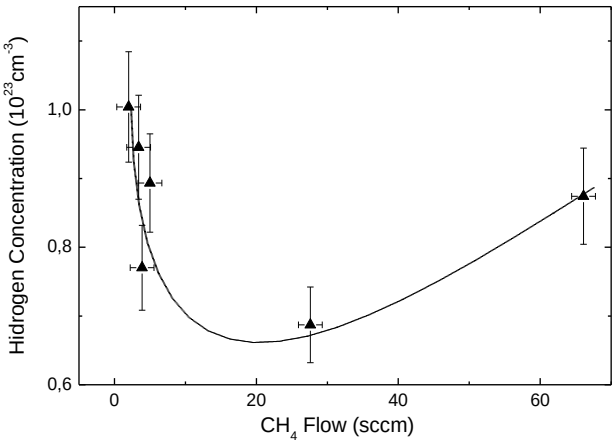

Figure 2- Hydrogen concentration of a-C:H films, using the integrated area of the C-H stretching mode (2800-3000 cm^{-1} wavelength range), as a function of methane flow rate.

Figure 3 shows the fitting results of Raman spectra for the films as a function of the methane gas flow rate. It shows the G peak position (3a), full width at half maximum, FWHM, of the G peak (3b) and the ratio between the intensities of the D peak by the G peak, I(D)/I(G), (3c). They show characteristic patterns of diamond like-carbon. The D peak is related to closed sp^2 structures (aromatics), and the G peak is related either to closed as well as open (olefenics) sp^2 structures. The full width at half maximum (FWHM) of the G peak (Fig. 3b) is associated with the structural order (angles and length of chemical bonds) of all sp^2 sites presented in the film. The I(D)/I(G) ratio (Fig. 3c) gives qualitative information about the number and the order of aromatic structures. It indicates a slight decrease in the graphitic characteristic as the methane flow decreases. On the other hand, the FWHM displayed in Fig. 3b indicates that all samples have similar structural order with exception to the sample deposited at zero flow, where the value of FWHM (G) was lower, revealing a more organized film. In view of this result, the I(D)/I(G) ratio is probably related to aromatic structures only.

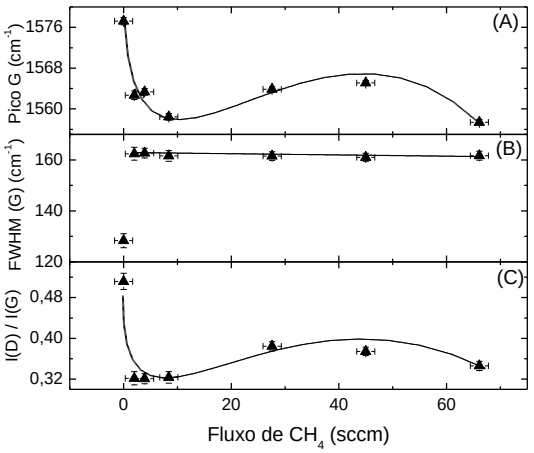

Figure 3 – (a) Wavenumber (Raman shift) position of the G peak; (b) full width at half maximum (FWHM) of the G peak and (c) ratio between the intensities of the D and G peaks, I(D)/I(G), as a function of methane flow rate.

The sample deposited at zero flow rate presents a behavior quite different from the others. We ascribed this behavior to the condition of the deposition of this film. When the system is not pumped, a rapid enrichment with H_2 in the atmosphere is established and the deposition process stops after the depletion of methane gas and the radicals containing carbon atoms (C_2H_2, C_2H_4, and others, generated by the methane plasma). That means the deposition is performed with a significant variation in the composition of the atmosphere, which varies from pure methane to pure hydrogen plasma. The enrichment of H_2 molecules in the atmosphere changes the film properties.

Conclusion

Diamond like carbon (a-C:H) were deposited by PECVD as a function of methane gas flow rate. It was observed that the deposition rate has a maximum at a relatively low methane flow rate (about 4 sccm for our system). Raman measurements indicate that at low methane flow rate the material becomes less graphitic. The film prepared at zero flow can be deposited with an extremely reduced amount of methane gas, been 2 to 3 orders of magnitude smaller than that adopted for the deposition of films following traditional procedures.

Acknowledgment

This work was supported by the Brazilian research agencies FAPESP, CNPq and CAPES.

References

1. S. Neuville, A. Matthews, MRS Bulletin 22, 22 (1997)
2. C. H. P. Poa, S. R. P. Silva, R. G. Lacerda, G.A.J. Amaratunga, W.I. Milne and F. C. Marques, Applied Physics Letters 86 (23) Art. No. 232102 (JUN 6. 2005).
3. G. A. J. Amaratunga and S.R.P. Silva, Appl. Phys. Lett. 68, 2529 (1996)
4. J. Robertson, Materials Science and Engineering, R 37 (2002) 129-281
5. F. C. Marques, R. G. Lacerda, A. Champi, V. Stolojan, D. C. Cox and S. R. P. Silva, Appl. Phys. Lett. 83(15) 3099 (2003)
6. R.G. Lacerda and F. C. Marques, Applied Physics Letters, 73 (5), 617 (1998).
7. W. Zhang and Y. Catherine, Surf. Coat. Techn. 47 (1991) 69-83.

A complete version of the manuscript was published in Diamond and Related Materials 19 (2010) 756.

Residual stresses in titanium nitride thin films obtained with step variation of substrate bias voltage during deposition

A.G. Gómez[a] , A.A.C. Recco[b], N.B. Lima[c], L.G. Martinez[c], A.P. Tschiptschin[b], R.M. Souza[a]

[a] Surface Phenomena Laboratory, Department of Mechanical Engineering, Polytechnic School of the University of São Paulo, Av. Professor Mello Moraes, 2231, São Paulo, Brazil.

[b] Department of Metallurgy and Materials Engineering, Polytechnic School of the University of São Paulo, Av. Professor Mello Moraes, 2463, São Paulo, Brazil

[c] Nuclear and Energy Research Institute, IPEN, Av. Prof. Lineu Prestes, 2242, São Paulo, Brazil

Abstract

In this work, a series of depositions of titanium nitride (TiN) films on M2 and D2 steel substrates were conducted in a Triode Magnetron Sputtering chamber. The substrate bias was either decreased or increased in a sequence of steps. Residual stress measurements were later conducted through the grazing x-ray diffraction method. Different incident angles were used in order to change the penetration depth and to obtain values of residual stress at different film depths. A model described by Dolle was adapted as an attempt to calculate the values of residual stress at each incident angle as a function of the value from each individual layer. Stress results indicated that the decrease in bias voltage during the deposition has produced compressive residual stress gradients through the film thickness. On the other hand, much less pronounced gradients were found in one of the films deposited with increasing bias voltage.

Introduction

The deposition of thin films on substrates is usually inherently associated with the development of residual stresses[1,2]. In general, Physical Vapor Deposition (PVD) processes result in compressive stresses on the order of a few GPa[3,4]. Data in the literature[5,6] indicate that compressive stresses can improve the wear resistance of coated systems, but can also increase the possibility of film detachment during system use in tribological applications[5,6]. In theory, one could think that the imposition of a stress gradient in the film could be beneficial. Lower levels of compressive residual stresses at the film/substrate interface would decrease the tendency for film detachment and a gradual increase in compressive values towards the surface would improve wear resistance. The idea of gradient film stresses was already presented in the literature[7,8]. However, one of the challenges associated with such idea is to verify if the deposition procedure was successful in imposing the stress gradient and also to determine the residual stress values in such gradients using a non-destructive technique.

Several authors have studied film stress and strain gradients through grazing incidence x-ray diffraction (GIXD) techniques, where the penetration depth was varied by changing the incident angle of the beam. These x-ray methods are usually employed to determine stresses in thin films produced with constant deposition parameters. Little work has been conducted in order to verify if the variation of the parameters selected during deposition results in stress gradients. Exceptions may be found[7], but stress gradients were measured in combination with stepwise removal of the film layers by mechanical polishing.

The objectives of this work are to verify the possibility of imposing stress gradients in thin films by changing the process parameters during deposition and to adapt a model available in the literature[9] in order to evaluate these gradients using a non-destructive technique.

Experimental details

TiN films were deposited on steel substrates. A hybrid duplex treatment was carried out in all cases, in a home built hybrid reactor, where pulsed plasma nitriding and triode unbalanced reactive magnetron sputtering are conducted in the same cycle[10]. Three types of specimens were produced in this work (Table 1): Specimens with films deposited (i) without variation of substrate bias voltage during deposition (S1, S2, S3, S4 and S5), (ii) with increasing substrate bias voltage (G1D2 and G3M2), and (iii) with decreasing substrate bias voltage (G2D2 and G4M2).

Table 1: Deposition conditions for TiN thin films

Sample	Substrate material	Layer	Time (min)	Bias (V)	Film thickness (μm)
G1D2	AISI D2	1	45	-20	≈ 2.4
		2	45	-40	
		3	45	-100	
		4	45	-150	
		5	45	-200	
G2D2	AISI D2	1	45	-200	≈ 2.0
		2	45	-150	
		3	45	-100	
		4	45	-40	
		5	45	-20	
G3M2	AISI M2	1	45	-20	≈ 1.4
		2	45	-40	
		3	45	-80	
		4	45	-100	
G4M2	AISI M2	1	45	-100	≈ 1.4
		2	45	-80	
		3	45	-40	
		4	45	-20	
S1	AISI D2	1	120	-20	≈ 1.5
S2		1	120	-40	
S3		1	120	-100	
S4		1	120	-150	
S5		1	120	-200	

In this work, the GIXD method was used and S_1^{hkl} and $½S_2^{hkl}$, the X-ray elastic constants, were calculated for the different lattice planes (*hkl*) using procedures defined in the literature[11-13]. In the analysis, different angles of incidence (α) were selected in order to measure the residual stresses at different beam penetration depths. Measurements were conducted part at LNLS - Brazilian Synchrotron Light Laboratory and part in a Rigaku RINT Ultima+ diffractometer.

In X-ray diffraction, the intensity of the incident beam is attenuated exponentially by the specimen due to absorption. Therefore, if the specimen stress changes with the distance from the surface, the measured value is affected not only by the variation of the stress but also by any change in the penetration depth. Dolle[9] described a method to calculate the mean value of residual stress over a depth *x* based on the depth profile of stress $\sigma(x)$, assuming it is a continuous function. However, in the case of multilayered coating systems, or films deposited with step variation of bias voltage, the method must be corrected to consider that $\sigma(x)$ is not continuous[14]. Adjusting the model by Dolle and assuming that the procedure has succeeded in producing a step distribution of residual stresses, a system composed of N_L layers will have a mean stress over a depth *x*, at a given angle of incidence (α_i), given by:

$$\sigma(\alpha_i) = \sum_{n=1}^{N_L} I_n(\alpha_i)\sigma_n \qquad (1)$$

where σ_n is the mean residual stress of layer *n*, *t* is the thickness of the film, and τ is the mean penetration depth. Furthermore, $i=1,2,\ldots,N_\alpha$ is the number of the angle of incidence that is considered and

$$I_n(\alpha) = \frac{\int_{t_{n-1}}^{t_n} e^{-x/\tau}dx}{\int_{o}^{t} e^{-x/\tau}dx} \qquad (2)$$

Since the values of σ_n are unknown, the values of stress measured in the films deposited at constant bias voltage (S1 to S5) were used to calculate the mean stress at each angle of incidence.

In this work, Eq. 1 was also used in an attempt to calculate the residual stress value in each layer based on the average residual stresses obtained in a given specimen at each of the angles of incidence. Thus, based on an optimization algorithm, Eq. 1 was used to find the values of σ_n that would best provide the N_α values of $\sigma(\alpha_i)$ obtained experimentally for a given specimen.

Results and discussion

The residual stress values calculated for specimens S1 to S5, deposited with constant bias voltage, initially increased as the bias voltage increased. This behavior has been previously reported in several works regarding thin films deposited by sputtering. Some authors have found that the stresses reach a maximum value as the negative bias substrate increases[2,15], which was observed in this work.

Fig. 1 shows a comparison between the experimental results of specimens deposited with variation of bias voltage, and the values of stress over a depth at each angle of incidence, calculated using the model in Eq. (1). In specimens G2D2 and G4M2, which were deposited with decreasing bias voltage, Fig. 1 indicates smaller compressive residual stress levels near the surface and higher residual stresses closer to the film/substrate interface. This behavior was expected since lower stresses should be associated with lower bias. In terms of specimens G1D2 and G3M2, in which the bias voltage was increased during deposition, high compressive stresses were expected at the surface and smaller stresses were expected at the interface, as previously obtained by Fischer and Oettel[7]. However, in specimen G1D2 the difference found in residual stress level between the surface and the interface was not significant. In specimen G3M2 a difference of 1 GPa was observed between the interface and the surface. In general, Fig. 1 shows that the trend in residual stress values predicted by the model is in agreement with the experimental results, although some discrepancy can be observed in terms of the absolute values.

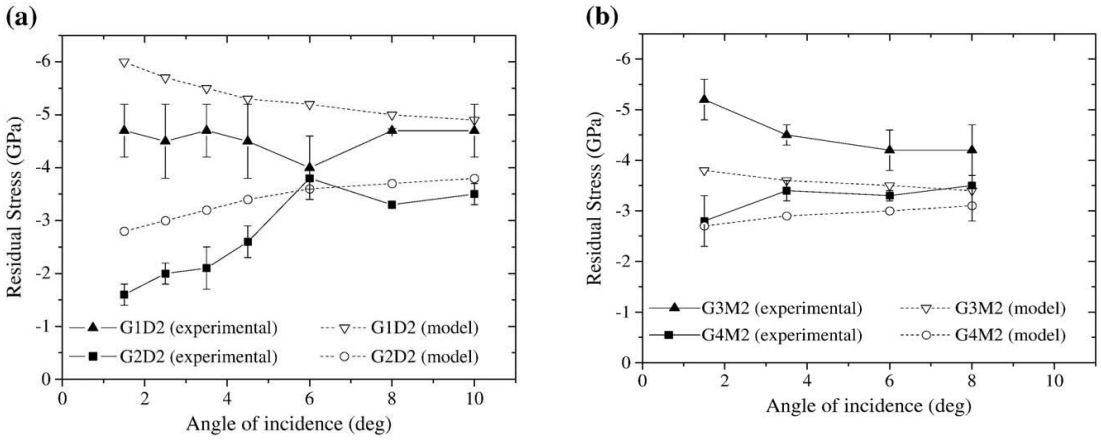

Fig. 1: Comparison between the experimental values of residual stress of specimens deposited with variation of bias voltage, and the results of stress over a depth calculated using the model of (a) specimens deposited on AISI D2 substrates, and (b) specimens deposited on AISI M2 substrates.

The results of the optimization method are shown in Fig. 2. In this figure, the open squares represent the values of residual stress calculated for films deposited at constant bias voltage. In terms of the values that were obtained, the results of the optimization procedure presented in Fig. 2b) suggest that, although differences exist in terms of the maximum residual stress value and the voltage at which the residual stresses reach the maximum, the trend was similar to that of the specimens deposited with constant bias voltage. Fig. 2a presents the optimization procedure for specimens produced with increasing bias In this case, although the optimization values for specimen G3M2 suggest that the differences in experimental and predicted results were due to the layer stress values used in Eq. (1), the optimization results suggest that no stress gradient was obtained for specimen G1D2. At this point, no reason was found to explain why such differences may occur for the two films produced with increasing bias, especially when one considers that the differences were basically regarding the substrate and film thickness.

Conclusions

A model described by Dolle was adapted to calculate the residual stresses as a function of beam penetration depth for the cases where deposition was conducted to impose a step variation in residual stresses along the film thickness. The values of stress measured in the films deposited at constant bias voltage were used in the calculations. The results were compared with the experimental ones, providing good qualitative agreement in all cases.

An optimization procedure was later conducted to analyze the individual layer values that would provide the best agreement with the experimental values calculated as a function of penetration depth. The results suggest that, in most cases, a step variation in residual stresses may have been obtained, and that the differences between experimental and predicted results are due to the stress value selected for each layer. The optimization procedure suggested that no step variation in residual stresses was obtained for one of the specimens produced with increasing bias.

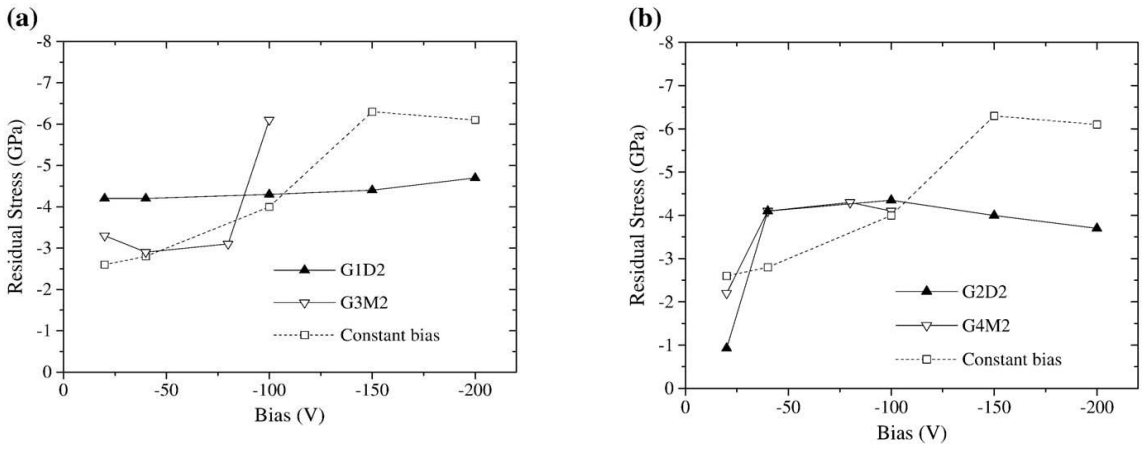

Fig. 2: Values of mean stress of each layer obtained using an optimization procedure for specimens deposited with a) increasing substrate bias voltage and b) decreasing substrate bias voltage.

Acknowledgements

Research supported by LNLS - Brazilian Synchrotron Light Laboratory/MCT, under proposal D12A - XRD1 6680. The authors are grateful to the Laboratório de Cristalografia – Instituto de Física- Universidade de São Paulo and to CNPq (National Council of Technological and Scientific Development) for grants 303780/2008-8 and 150966/2009-1.

References

1. Jansen,G.C.A.M. Stress and strain in polycrystalline thin films. Thin Solid Films, v.515, p.6654-6664, 2007.
2. Pauleau, Y. Generation and evolution of residual stresses in physical vapour-deposited thin films. Vacuum, v.61, p.175-181, 2001.
3. Perry,A.J et al. X-ray residual stress measurement in TiN, ZrN and HfN films using the Seemann-Bohlin method. Thin Solid Films, v.214, p.169-174, 1992.
4. Holmberg,K. et al. Residual stresses in TiN, DLC and MoS_2 coated surfaces with regard to their tribological fracture behavior. Wear, v.267, p.2142-2156, 2009.
5. Bull,S. Can scratch testing be used as a model for the abrasive wear of hard coatings? Wear, v.233-235, p.412-423, 1999.
6. Cozza,R.C. et al. Micro-abrasive wear of DC and pulsed DC titanium nitride thin films with different levels of film residual stresses. Surface and Coatings Technology, v.201, p.4242-4246, 2006.
7. Fischer,K., Oettel,H. Microstructural gradients in thin hard coatings – tailor-made. Surface and Coatings Technology, v.97, p.308-312, 1997.
8. Uhlmann, E., Klein, K. Stress design in hard coatings. Surface and Coatings Technology, v.131, p.448-451, 2000.
9. Dolle,H. The influence of multiaxial stress states, stress gradients and elastic anisotropy on the evaluation of (residual) stress by x-rays. Journal of Applied Crystallography, v.12, p.489-501, 1979.
10. Recco, A.A.C. et al. Adhesion of reactive magnetron sputtered TiN_x and TiC_y coatings to AISI H13 tool steel. Surface and Coatings Technology, v.202, p.1078-1083, 2007.
11. Fillit,R.Y., Perry,A.J. Residual stress and x-ray elastic constants in highly textured physically vapor deposited coatings. Surface and Coatings Technology, v.36, p.647-659, 1988.
12. Atar,E.C. et al. Residual stresses in (Zr,Hf)N films (up to 11.9 at.% Hf) measured by x-ray diffraction using experimentally calculated XECs. Surface and Coatings Technology, v.191, p.188-194, 2005.
13. Perry,A.J. A contribution to the study of Poisson's ratios and elastic constants of TiN, ZrN and HfN. Thin Solid Films, v.193/194, p.463-471, 1990.
14. Klaus,M. et al. Residual stress depth profiling in complex hard coating systems by x-ray diffraction. Thin Solid Films, v.517, p.1172-1176, 2008.
15. Davis,C.A. A simple model for the formation of compressive stress in thin films by ion bombardment. Thin Solid Films, v.226, p.30-34, 1993.

A complete version of the manuscript was published in Surface and Coatings Technology 204 (2010) 3228.

Characterization of nanoparticles through medium-energy ion scattering (MEIS)

M. A. Sortica, P. L. Grande, G. Machado, L. Miotti

Universidade Federal do Rio Grande do Sul, Instituto de Física, Avenida Bento Gonçalves 9500, 91501-970 Porto Alegre, RS, Brazil

Abstract

In this work we review the use of the MEIS technique to characterize nanostructures at the surface of a substrate. We discuss here how the determination of shape and size distribution of the nanoparticles is influenced by the energy-loss at the backscattering collision, which leads to an asymmetrical energy-loss line shape. We show that the use of a Gaussian line shape may lead to important misinterpretations of a MEIS spectrum for nanoparticles smaller than 5 nm. The results are compared to measurements of gold nanoparticles adsorbed on a multilayered film of weak polyelectrolyte.

Introduction

Nanotechnology has brought some new challenges, not only for the development of new processes for synthesis of nanostructures but also for the characterization of them. The latter is usually achieved by techniques involving incident electrons or photons (e.g. electron microscopy, X-ray spectroscopy and diffraction, and ultraviolet–visible spectroscopy), and to a less extend by using incident ions (e.g. Rutherford backscattering spectrometry – RBS) [1].

Determining the depth distribution of different chemical elements near and at the surface of solids is of major importance for many aspects of nanotechnology. In principle, this can be accomplished quantitatively with deep subnanometric depth resolution, using ion scattering at energies corresponding to the maximum stopping power and high-energy resolution detection systems. The method is called medium energy ion scattering (MEIS) [1,2] and uses typically 100-200 keV incident H^+ or He^+ ions, and combines effects of elastic recoil energy loss and inelastic losses, as in a conventional Rutherford backscattering. The MEIS technique is widely used for analysis of microelectronic materials as well as for the determination of structural and vibrational parameters of crystalline surfaces [3].

More recently, the MEIS technique was used as an additional tool for characterization of Pt-Rh [4] and Au nanoparticles [5] and of InAs-GaAs quantum dots [6] Basically the nanoparticles shape, composition, size distribution and stoichiometry have been successfully obtained. In addition, the determination of the number of nano-size inhomogeneities in thin films was also investigated for some particular geometrical shapes. Nevertheless, the most promising MEIS application, namely the determination of depth distributions of different elements in a single nanoparticle, still needs further investigations. This possible MEIS application is unique and is hardly achieved by any other analytical technique.

In this work we developed a Monte Carlo simulation of MEIS spectra that considers any nanoparticle geometry and areal density, going beyond previous investigations that were restricted to few specific nanostructures shapes and surface coverage [7]. The present method also includes the effect of the asymmetry of the energy-loss distribution due to a single violent collision such as the backscattering event. Using this method we investigated the influence of the nanoparticle geometry, areal density, size distribution, and energy-loss line shape on the 1D (energy) and 2D (energy and angle) MEIS spectrum.

MEIS technique

MEIS is based on the same principles of Rutherford backscattering spectrometry (RBS), however the implementation and data analysis of MEIS is somehow different. A toroidal electrostatic energy analyzer, with a much larger solid angle, replaces the surface barrier detector used in RBS analysis. The system presents a much better energy resolution, typically dE/E of about 10^{-3}, meanwhile both the energy and the scattering angle are simultaneously stored in a 2D multichannel system.

The experimental work was performed at the Ion Implantation Laboratory of the Physics Institute (Federal University of Rio Grande do Sul). A 500 kV electrostatic accelerator provided beams of H^+ at a nominal energy of 100 keV. The samples were mounted in a 3-axis goniometer inside the analysis chamber kept under a pressure of about 10^{-7} mbar. Typical ion current was less than 15 nA and the samples was moved each 4.5 C in order to avoid damage of the nanoparticles. Details of the data analysis are found in ref[8]

Simulation procedure

General formulas to simulate MEIS or RBS spectra were proposed only for particular shapes of nanostructures such as for spherical and columnar nanoparticles (or inhomogeneities) [9]. Here we followed a quite general approach, where any nanoparticle geometry, inclusions, porous, inhomogeneities, and their corresponding areal and size distributions are accounted for. To this end, we use the Monte Carlo method for the 3D-spacial integrations and determine the incoming- and outgoing-projectile paths numerically from the incident and scattering angles. The best way to determine the shape of a nanoparticle through the MEIS technique is to look at all different scattering angles available since each geometrical shape has a typical angular dependence of the backscattering yield. For normal incidence, figure 1 shows this angular dependence for the 4 geometries and beam parameters mentioned above. The overall features are the following. As well known, for films, the decrease of the highest backscattering energy (the front edge in a 1D MEIS spectrum) with increasing scattering angle is only due to the variation of the kinematical factor K. The rapid decrease of the lowest detected energy for smaller scattering angles is a direct consequence of the enhanced path length (by the factor 1/cos(Θ)) in a grazing detection direction. Thus, the energy-loss spectrum is much wider at smaller scattering angles. In the case of a spherical nanoparticle, as depicted in Fig. 1, we have the opposite. In normal incidence, the maximum path length of two diameters is found at the scattering angle of 180 degrees, which makes the energy-loss wider at large scattering angles. For the hemisphere (see Fig. 1), the enhancement of the path length at larger scattering is not as important as in a sphere, neither the enhancement at smaller scattering angle is as large as in a film. In this way, the lowest energy edge will depend weakly on the scattering angle. Finally, the cylindrical geometry (representing disks, wires or columnar structures) is peculiar because the energy spectrum is widest at an intermediate scattering angle, where the outgoing particles can travel along a major diagonal of the cylinder. Thus, MEIS could easily identify uniformly right or oblique cylinders.

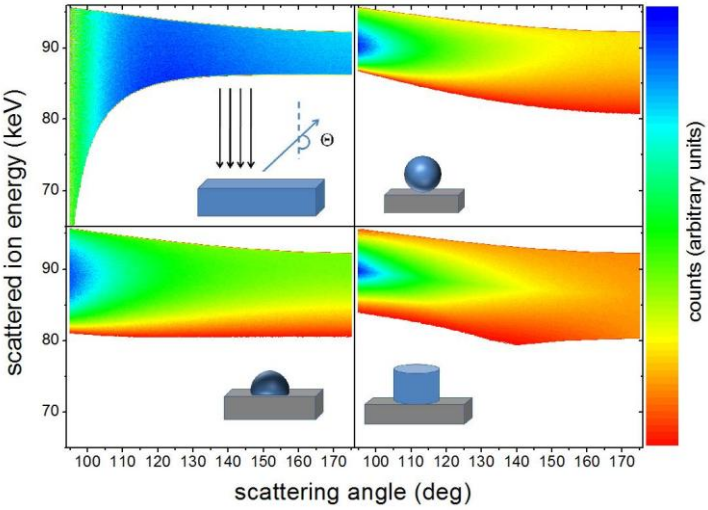

Fig.1:Two-dimensional map of scattered ion intensities as a function of scattering angle and scattered ion energy for incidence of 100 keV He+ ions.

Comparison with experimental data

A sample containing Au nanoparticles were prepared using the layer-by-layer (L-b-L) process to get nanoparticles with specific size through methodology [10]. Here, the polyelectrolyte multilayer (PEM) was used to bind nanoparticles. This process involves deposition of weak polyelectrolytes from diluted aqueous solution, based in electrostatic interactions of opposite polymer charges, on specific substrates.. The samples were first characterized by transmission electronic microscopy (TEM) using JEOL 200CX operated at 120 kV. The Au nanoparticles image and the inset for the corresponding size distribution are found in Figure 2. The gold nanoparticles obtained are spheres with mean diameter of about 11.2 nm. The experimental and simulated MEIS energy-angle spectra for the gold nanoparticle described above are shown in Figure 3. The simulation was performed considering spherical Au nanoparticles separated from each other by 8 nm and the best fit criterion was the minimum chi squared for 3 different scattering angles. The agreement is very good and the remaining differences can be attributed to a better description of the target. In fact, overlapping nanoparticles and their distribution in depth and distance from each other were not included in the simulation. Overlapping nanoparticles are visible in the TEM cross-view image, but they are the result of projection on the transversal plane. If we have considered any other geometry, the resulting 2D spectra would be significantly different from the experimental one. Concerning the determination of size distribution of nanoparticles, the uncertainties are about 5 % for the mean diameter and 15% for the Two-dimensional map of scattered ion intensities as a

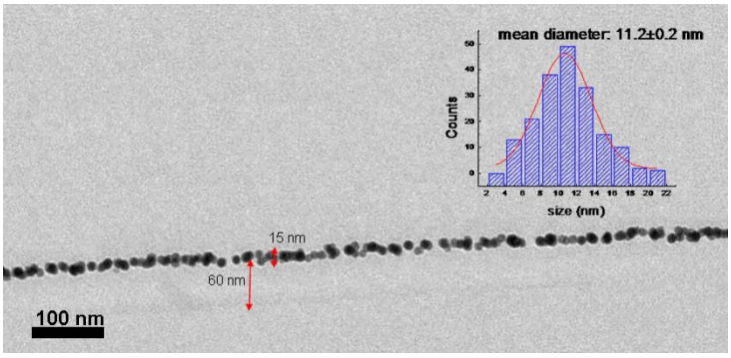

Fig.2:TEM image and size distribution of gold nanoparticles (inset).

function of scattering angle and scattered ion energy for incidence of 100 keV H ions. The experimental data are shown on the left and theoretical simulation on the right.

For the present case of nanoparticles with mean diameter of about 11nm, the use of the Gaussian energy-loss distribution would affect the prediction of the mean diameter by only 3%. The comparison of the full energy-angle distributions is a unique feature of the present simulation Two-dimensional map of scattered ion intensities as a function of scattering angle and scattered ion energy for incidence of 100 keV H ions. The experimental data are shown on the left and theoretical simulation on the right. Two-dimensional map of scattered ion intensities as a function of scattering angle and scattered ion energy for incidence of 100 keV H ions. The experimental data are shown on the left and theoretical simulation on the right.

Conclusions

The main results of the present investigation can be summarized as follows: a) we observed that, although the influence of the energy-loss distribution on the MEIS spectrum is significant only for small nanoparticles (diameter < 5 nm), the use of the actual nanoparticle geometry is important for all sizes of nanostructures;b) neglecting the asymmetry of the energy-loss leads to a false nanoparticle size distribution in the case of small nanoparticles; c) the method used here is the first to our knowledge not restricted to a few nanoparticles shapes and surface coverage.

Finally, we used the method described here to simulate MEIS spectra and determine the shape and size distribution of gold nanoparticles adsorbed on a multi-layered film of weak polyelectrolyte. The parameters obtained for the nanoparticles from the simulation of experimental MEIS spectra agrees quite well with an image obtained by transmission electron microscopy (TEM) of the sample.

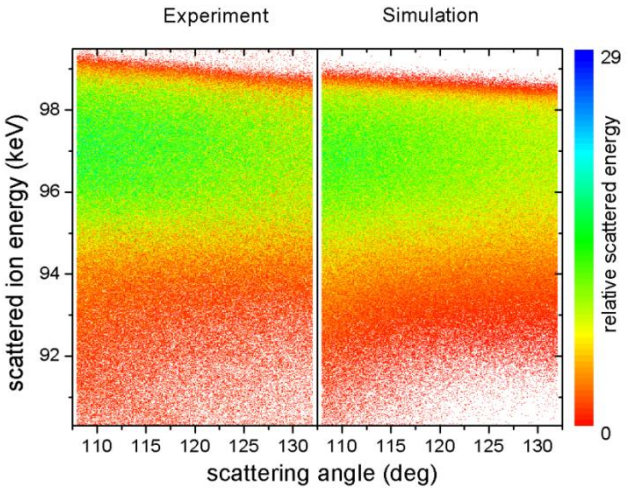

Fig.3 Two-dimensional map of scattered ion intensities as a function of scattering angle and scattered ion energy for incidence of 100 keV H ions. The experimental data are shown on the left and theoretical simulation on the right.

References

1. S. J. Rosenthal, James McBride, Stephen J. Pennycook, Leonard. C. Feldman, Surface Science Reports **62**, 111 (2007).
2. J.F. van der Veen, Surf. Sci. Rep. **5**, 199 (1985).
3. D. P. Woodruff and T. A. Delchar, Modern Techniques of Surface Science – second edition, Cambridge University Press
4. Konomi, S. Hyodo, and T. Motohiro, Journal of Catalysis **192**, 11 (2000).
5. T. Okazawa et al., Surface Science **600** 1331 (2006).
6. T. Okazawa, M. Kohyama, and Y. Kido, Surface Science **600**,4430 (2006).
7. P.D. Quinn, N.R. Wilson, S. A. Hatfiled, C.F. McConville, G.R. Bell, T.C.Q. Noakes, P. Bailey, S. Al-Harthi, F. Gard,. Applied Physics Letters **87**, 153110 (2005).
8. J.P. Stoquert and T. Szörényi, Physical Review B **66**, 144108 (2002).
9. S. M. Shubeita, M. A. Sortica, P. L. Grande and J. F. Dias, Physical Review B **77** 115327 (2008).
10. Nicholas A. Kotov; Imre D.Ckiiny, and Janos H. Fendler, J. Phys. Chem., **99** 13065 (1995).

A complete version of the manuscript was published in Journal of Applied Physics, 106 (2009) 1.

Adhesion of L929 mouse fibroblast cells on poly(styrene)/poly(methyl methacrylate) films modified by cold oxygen plasma process

A. M. G. Borges and V. Soldi

Departamento de Química – UFSC, Florianópolis/SC

Introduction

Biomaterials are one of the most productive research areas in materials science. As a result, a great diversity of new classes of materials has been created. Researchers are currently using synthetic and/or natural macromolecule biomaterials for the fabrication of devices designated to replace a biological tissue or organ with the ultimate goal of promoting life. In this sense, the synthesis of new polymeric materials that interact favorably with biological organisms may favor the replacement of damaged organs, hence promoting the quality of life of patients[1]. Thus, it is of interest to produce polymers that have physical-chemical properties as similar as possible to the tissues in which they are employed. A number of important properties of polymeric materials, including their interaction with biological systems, are controlled by their surface chemistry and morphology[2,3]. Polymer films have a wide field of application, due to some properties that are inherent to this type of material, such as good mechanical strength, chemical resistance to acids and bases and low production cost. However, polymer films have limitations such as low surface tension, low roughness and poor adhesion, which prevent their use in some instances, especially when such use requires that the material has a good wettability, hence requiring the use of techniques capable of modifying their surfaces[4]. The cold plasma generated in a dielectric barrier discharge (DBD) device operating close to atmospheric pressure was used for the purpose of surface treatment. The advantage of this process is that the surface properties and biocompatibility can be enhanced selectively, whereas the attributes of the material remain unchanged[5]. In the present study, polymeric films of PS, PMMA and 1:1 PS/PMMA blends were prepared and characterized. The biocompatibility of the polymeric films was assessed by studying cell adhesion and proliferation of L929 mouse fibroblasts.

Experimental

Poly(styrene) (PS), Mw = 300500 g mol^{-1}, and poly(methyl methacrylate) (PMMA), Mw =139595 g mol^{-1}, were obtained from Aldrich Chemical Co. (St. Louis, USA) and chloroform ($CHCl_3$) was obtained from Nuclear (São Paulo, Brazil). All materials were used without further purification.

Films were prepared by dissolving the polymers in 2% (m/v) $CHCl_3$ in a closed flask under magnetic stirring for 24 h at room temperature followed by solvent evaporation (casting method).

The plasma system used in this work is schematically shown in Figure 1. The films were wrapped up in order to cover the inner surface of the quartz tube in the plasma discharge zone. Afterwards, the system was purged with O_2 for a few minutes (1 L min^{-1}) in the DBD reactor using the input gas positioned at the bottom cap of the reactor, in order to eliminate possible gaseous contaminants present in the system. The plasma system was turned on during the treatment time (1-4 hours) and triggered the gas phase chemical reactions, which promoted the modification of the polymeric surface. Finally, the films were taken from the DBD reactor and maintained in an argon atmosphere inside desiccators, until further use. Subsequent tests were performed 24 hours after plasma treatment.

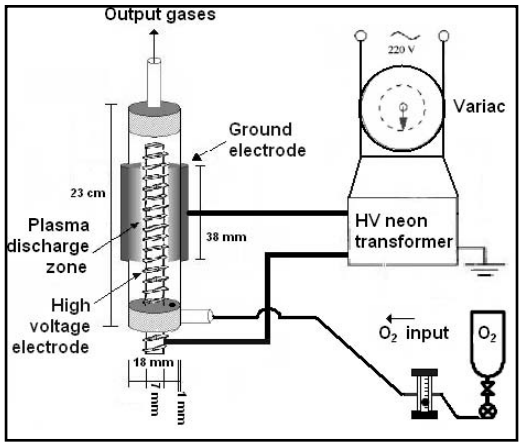

Figure 1 - Experimental setup used in this work.

The contact angles were measured after deposition of drops of distilled and deionized water on the films under study. A DATA PHYSICS goniometer with Image Tool software especially designed for this type of analysis was used. A high-resolution camera was used for image capture. Five measurements were carried out for each sample, and the mean value was considered.

Each of the polymeric films was cut into circular disks, soaked in 70% (v/v) ethanol, placed under UV light for 30 min for sterilization, and thoroughly washed with sterile phosphate-buffered saline (PBS) solution. For the experiments, cells were detached with trypsin, counted in a hemacytometer and seeded at a density of 50000 cells/well. Two types of control were used: cells seeded directly onto the well of the plastic plate or on top of a glass coverslip lying on the bottom of the well. The cells were stained with acridine orange and, after a 24 h incubation period, cell morphology was assessed by optical microscopy.

Results and Discussion

Figure 2 shows the variation of the interaction of the drop of deionized water with the material surface before and after plasma treatment. It can be observed that after treatment there was a significant decrease in the contact angle, as a result of an increase in the hydrophilicity of the material. This phenomenon is related to the concentration of oxygen in the polymeric surface, which resulted in formation of polar groups. It can be observed that the contact angle varies with the time used for plasma treatment, stabilizing at approximately 38° after 3 and 4 hours of treatment, as shown in Figure 3. The hydrophilicity of all sample surfaces was significantly improved after plasma treatment. Differences exceeding 60% in the values of contact angles of treated samples when compared to the same polymeric films that were not modified by the DBD plasma were observed. This means that the plasma treatment in any of the conditions used in this work increased substantially the wettability of the films. Figure 3 also evidences that the variation in treatment time of the polymeric films did not promote significant changes after 3 hours, as the contact angle observed following a 3 h-treatment was similar to that from a 4 h-treatment. This aspect is particularly relevant, as it represents significant time-saving, which can be especially critical for large-scale production of the material.

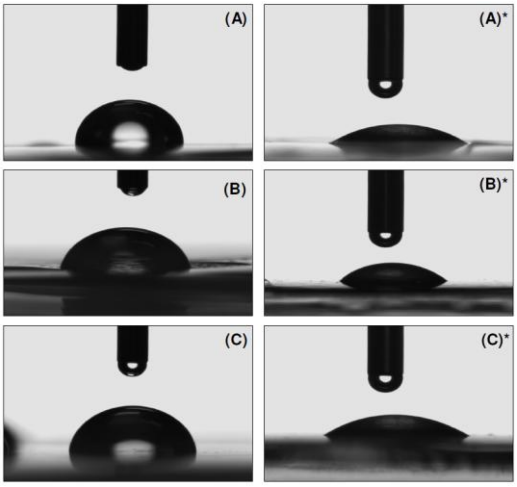

Figure 2 – Images of water droplets on the surface of films (A) PS, (B) 1:1 PS/PMMA blend and (C) PMMA films unmodified and * films modified t= 3 hours of plasma.

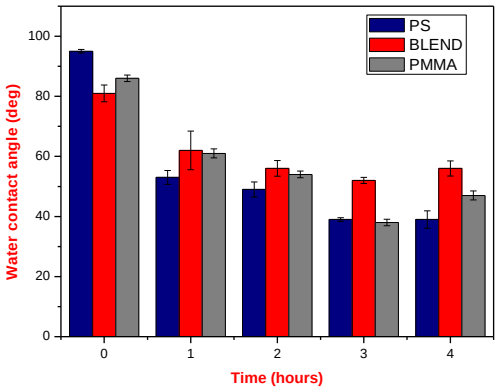

Figure 3 - Contact angle to the surface of the films before and after modification by DBD plasma.

As can be seen in Figure 4, L929 cells attached to and spread over the surface of all polymeric films and the results for cell adhesion after treatment of plasma did not differ from those of the control wells. Several adhesion processes can be seen in all images, assuring that the L929 cells adhered strongly to the polymeric films. The results of optical microscopy analysis revealed that there were no significant differences regarding the number of cells adhered to the polymeric films after treatment when compared to the untreated films. The pure PS film showed the highest number of adhered cells after treatment, which can be explained by the contact angle value. According to Yang *et al.*,[6] hydrophilicity is a relevant factor in defining cell adhesion. Polymeric films with moderate hydrophilicity are more efficient at promoting cell adhesion.

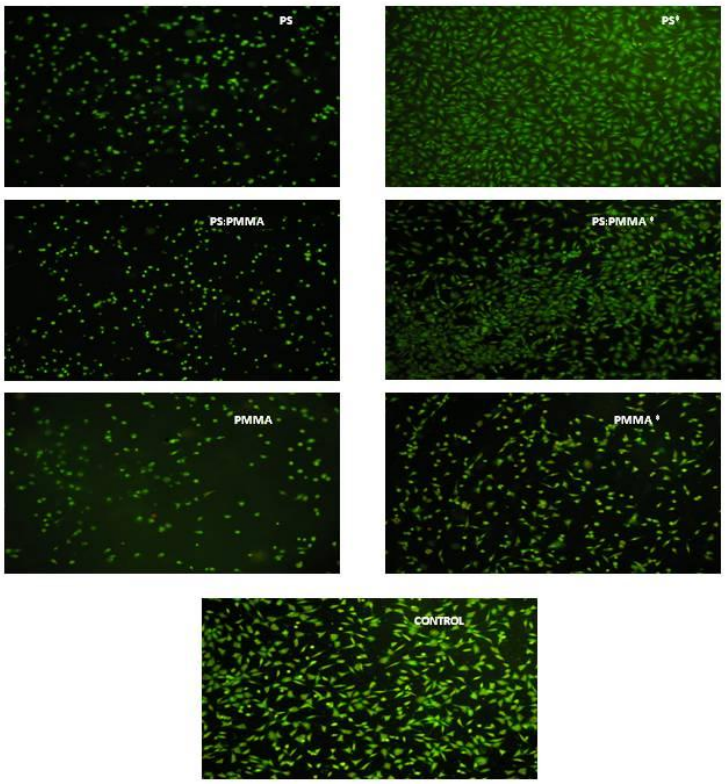

Figure 4 – Pictures of L929 fibroblasts on the surface of (A) PS, (B) 1:1 PS/PMMA blend and (C) PMMA films unmodified and * films modified t = 1 hour of plasma.

Conclusion

The oxygen plasma treatment using a dielectric barrier discharge (DBD) promoted an increase in the hydrophilicity of the studied samples, observed by a decrease in the contact angles of the plasma-treated film. This study suggests that plasma-induced surface changes increase the effectiveness of cell adhesion, since the cells adhere and spread more easily to surfaces with higher wettability. All films showed good cell adhesion after treatment, although analysis using optical microscopy showed that the pure PS film had the highest number of adhered cells after treatment, which can be explained by the increased contact angle observed in this film.

References

1. B. He; Y. Wan; J. Bei; S. Wang *Biom*. 2004, *25,* 5239.
2. S. E. Woodcock; W. C. Johnson; Z. Chen. *J. Colloid Interface Sci.* 2005, *292*, 99.
3. Melo; A. C. Bet; J. Assreuy; N. A. Debacher; V. Soldi. *J. Braz. Chem. Soc.* 2009, *20*, 1753.
4. C. M. Dekeiser; S. Biltresse; J. Marchand-Brynaert; P. G. Rouxhet; C. Duppont- . *Polymer*. 2004, *45*, 2211.
5. T. Desmet; R. Morent; N. Geiter; C. Leys; E. Schacht; P. Dubruel. *Biomac*. 2009, *10*, 2351.
6. J. Yang, J; J. Bei; S. Wang. *Biom*. 2002, *23*, 2614.

Silica-based solid sensors prepared by the sol-gel method

João Henrique Zimnoch dos Santos

Laboratory of Ziegler-Natta Catalysis, Instituto de Química – UFRGS

Abstract

The scope of the laboratory is the development of silica-based materials, with potential application as catalyst support, polymer additive, sorbents, sensors, preconcentration phases and chromatographic phases. The present text illustrates the development of two solid pH sensors with potential application in the fabrication of intelligent plastics, i.e., packing plastics which may change color in the case of degradation of the food by the alteration of pH or evolving of amines. In the first case study, the nature of the sol-gel route impinges some textural effects on the resulting sensor, which in turn responds differently to the target molecule. In the second case study, the presence of organic groups (coming from organoalkoxisilanes employed in the sol-gel synthesis) within the silica matrix affects the encapsulated content, and therefore the performance of the pH indicator.

Introduction

Sol-gel derived materials have received a peculiar interest as chemical receptor matrices due to their optical transparency, mechanical stability, chemical resistance and flexibility of sensor morphological configurations. Furthermore, the control of textural properties, in the case of pH sensors, enables a rapid response because the sol-gel matrix allows fast proton diffusion, and their ability to respond rapidly makes them desirable for use in pharmaceuticals, foods and chemicals industries [1].

The nature of the encapsulation route

We have investigated the effect of the nature of the indicator molecule and the influence of the sol-gel route on the structural, textural and morphological characteristics of the final sensor and its influence on the response to ammonia gas.[2] Three different pH indicators (alizarin red, brilliant yellow and acridine) were encapsulated by the three different sol-gel routes (the hydrolytic acidic, hydrolytic basic and non-hydrolytic routes), and the resulting systems performance were tested as acid-base sensors. Figure 1 illustrates the resulting sensors and their color change in contact with ammonia vapor. Shorter response times were achieved by the pH indicators encapsulated by acid route (RA). Higher incorporated indicator content was achieved by the non-hydrolytic sol-gel route (RNH).

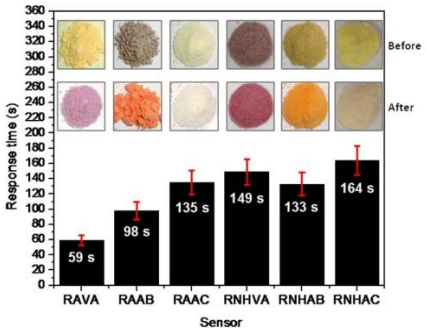

Figure 1. Incorporated content, visual color change and response time to ammonia gas for the synthesized solid sensors. RA = acid route; RNVA = non-hydrolytic route; VA = alizarin red; AB = brilliant yellow; AC = acridine.

Applications for real samples (environmental and industry samples) have shown their application as pH sensor. Figure 2 shows some examples about their pH range. It is worth mentioning that AC (acridine) is a fluorescent molecule.

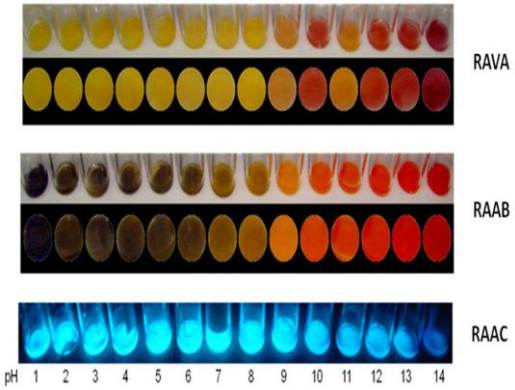

Figure 2. Performance of the solid sensor at different pH in environmental and industrial samples. RA = acid route; Indicators: VA = alizarin red; AB = brilliant yellow; AC = acridine.

The perception of color change of the sensor in the presence of ammonia was investigated by monitoring the perception of color change by 50 subjects. Correspondence analysis has shown statistic significance between females with blue eyes older than 25 years old and the visual perception and the rapid perception of color change of RAVA, for instance, as shown in Figure 3.

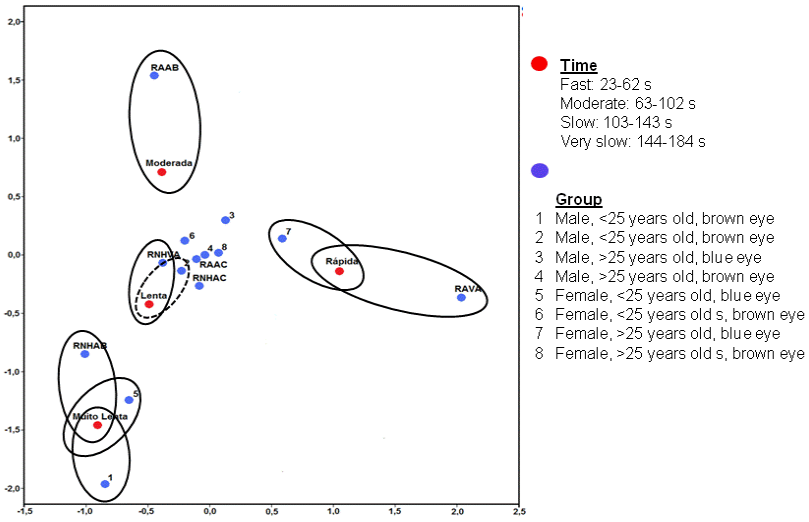

Figure 3. Correspondence analysis of the visual color change perception by the human eye.

Such behaviour can be assigned to delta color in the perception model of color change. Figure 4 provides the data showing the gap of color change of the solid sensors. Measurements were performed by diffuse reflectance in the UV-vis region and data were analyzed by color software.

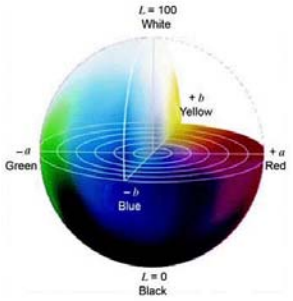

Sensor	Color coordination after NH_3 contact	AE^*_{ab}
RAVA		41,19
RAAB		37,23
RAAC		8,39
RNHVA		12,63
RNHAB		28,81
RNHAC		9,81

Figure 4. Correspondence analysis of the visual color change perception by the human eye. N = 50.

According to Figure 4, the acid route (RA) provides the higher color variation (Delta color). Furthermore, one can observe that the sol-route affects the pH indicator performance: compare the same indicator (VA): in the case of acid route (RAVA) and non-hydrolytic one (RNHVA).

The effect of organoalkoxysilane within the silica matrix

Another group of sensor was developed by the use of anthocyanins, pigments responsible for the red, purple, and blue colors of many fruits, vegetables, cereal grains, and flowers, as indicators. Anthocyanins were then efficiently incorporated within hybrid silica matrixes synthesized by the sol-gel method (series A). Silica structure was chemically modified with different organoalkoxysilanes. The presence of anthocyanins is revealed by the absorption band at 520 nm. Series B shows the series of hybrid silica without anthocyanins (Figure 4).

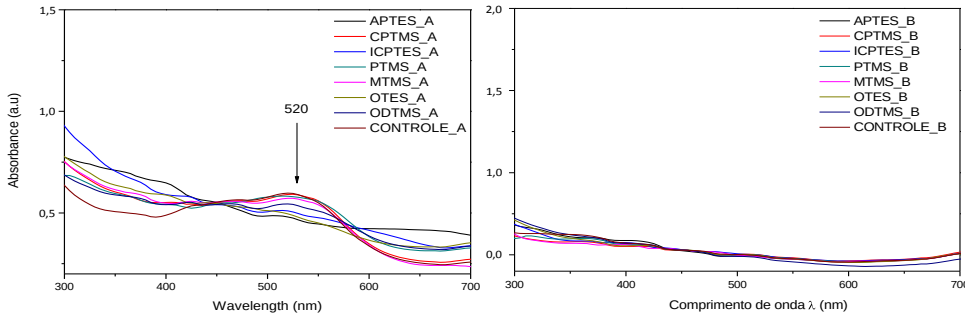

Figure 5. UV-vis spectra of hybrid silicas (serie B) and hybrid silicas containing encapsulated anthocyanins.

According to the results, the nature of the organoalkoxysilane impinges structural modifications in the silica matrix. Furthermore, as shown in Figure 5, the presence of anthocyanins affects textural characteristics of the hybrid matrices, resulting from the reaction between the organoalkoxisilanes and TEOS.

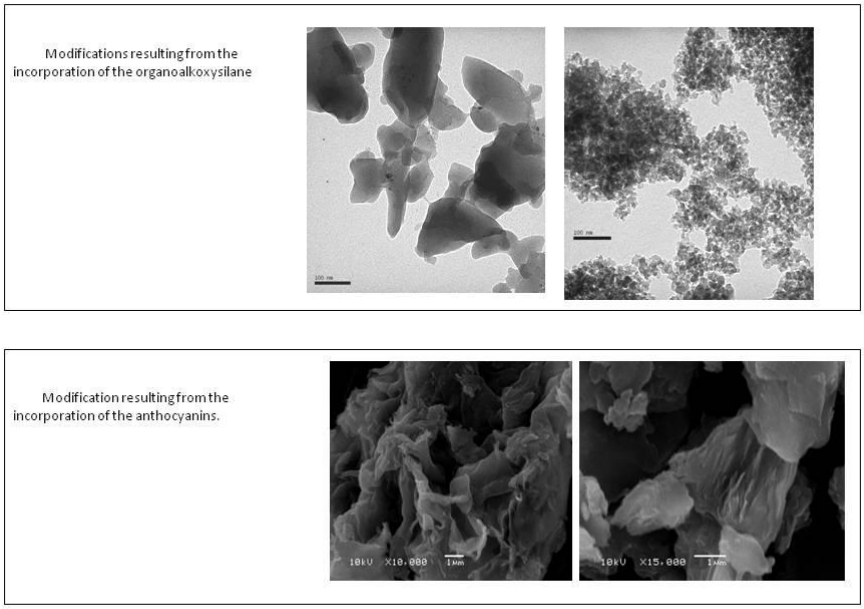

Figure 6 depicts the heterogeneity resulting from the distribution of anthocyanin. Brighter point represents higher anthocyanin concentration. In smaller circles, the sensor behavior vis-à-vis the pH is shown: rose/red (acid medium) – green (basic medium), observed for the neat anthocyanin.

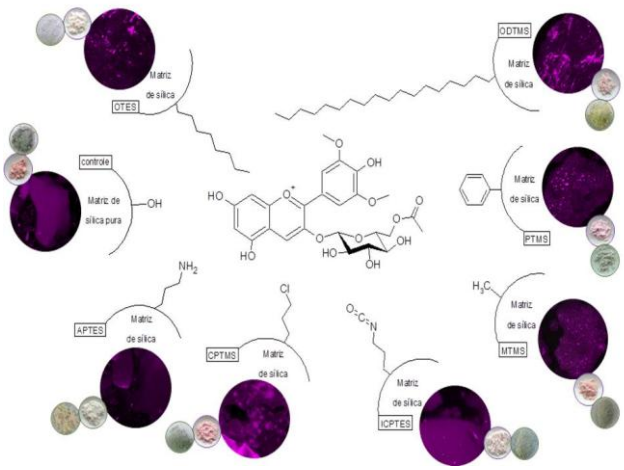

ODTMS_A

Figure 6. Scheme representing the color change and morphological aspects (confocal microscopy) of the anthocyanins encapsulated in hybrid silicas prepared in the presence of different organosilanes.

References

1. L.A. Terry, S.F. White, L.J. Tigwell, The application of biosensors to fresh produce and the winder food industry, *J. Agric. Food Chem.* 53 (2005) 1309-1316.
2. L.B. Capeletti, F.B Bertotto, J.H.Z. dos Santos, E. Moncada, The effect of the sol-gel route on the characteristics of acid-base sensors. *Sensor & Actuators B: Chemical* (2010) (no prelo).

A complete version of the manuscript will be published in Sensor & Actuators B: Chemical (2010)

Recent advances in diamond-like carbon-based nanocomposites

Vladimir Jesus Trava Airoldi, Fernanda Roberta Marciano, D.A. Lima-Oliveira, Polyana Alves Radi, Luis Francisco Bonetti*

Instituto Nacional de Pesquisas Espaciais (INPE),
Laboratório Associado de Sensores e Materiais (LAS)
*Clorovale Diamante S.A.

Abstract

Diamond-like Carbon (DLC) films have been the focus of extensive research in recent years due to its potential application as surface coatings. Crystalline diamond (NCD) and titanium dioxide (TiO_2) in the form or nanoparticles were incorporated in DLC films for different applications. The films were growth on 316L stainless steel substrates from a dispersion of these nanoparticles in hexane using plasma enhanced chemical vapor deposition. NCD particles reduced the steel pitting corrosion, improving DLC and stainless steel electrochemical corrosion resistance and preventing aggressive ions from attacking metallic surfaces. The presence of TiO_2 nanoparticles increased DLC bactericidal activity. In addition, TiO_2–DLC films increase the chemical interaction between bacteria and the films, which is an additional factor for the increasing bactericidal activity. From these results, nanoparticle-incorporated DLC films increase the range of applications of these coatings, adding them new properties.

Introduction

Diamond-like carbon (DLC) films have been actively studied over the last decades in the field of material engineering [1-2]. In our laboratory, it was developed a new technique that permits the deposit of DLC films from liquid hexane [3]. With this technique, it is possible to deposit films from a dispersion of different kind of nanoparticles in hexane in order to create different kind of DLC films for different applications. In this report, we show the main results obtained in our laboratories from the production and characterization of nanoparticle-incorporated DLC films.

The films were grown over 316L stainless steel using plasma enhanced chemical vapor deposition. Details concerning the sample preparation and deposition technique can be found in our previous publications [3-4]. To produce the nanoparticle-incorporated DLC films, crystalline diamond (NCD) and titanium dioxide (TiO_2) nanoparticles were dispersed in hexane at different proportions. These dispersions replaced the pure hexane during the DLC deposition.

Nanocrystalline diamond (NCD) particles with ~250 nm of average particle size were incorporated into DLC films in order to investigate NCD-DLC electrochemical corrosion resistance. Electrochemical tests were performed using a conventional three-electrode electrochemical cell [5]. In this cell, the reference electrode was a saturated Ag/AgCl electrode, the counter electrode was a platinum wire and the working electrodes were the stainless steel, DLC and NCD-DLC films. The electrolyte solution was a 0.5 mol/L sodium chloride (NaCl) aqueous solution, pH 5.8, which was not stirred and was naturally aerated. Potentiodynamic tests were carried out by polarization of samples in the anodic direction, from -2.0 to +2.0 V, just after exposition to the electrolyte solution. The potential sweep rate was 1 mV/s. The impedance measurements were also carried out in 0.5 mol/L NaCl aqueous solution, pH 5.8. The electrochemical impedance spectra (EIS) were obtained over the frequency range 100 kHz–10 mHz, at open circuit potential, with an AC excitation of 10 mV. All experiments were performed at room temperature.

The electrochemical stability of the systems in the test solution was investigated by the open-circuit potentials (OCP). The greatest E_{corr} value of -0.321 mV was observed for NCD-DLC films. The negative OCP values for the samples may be caused by the penetration of the test solution [6-7]. The electrochemical parameters obtained from the potentiodynamic polarization curves (Fig. 1a) are given in Tab. 1. The corrosion current density (i_{corr}) of NCD-DLC films reduced by more than 5 times with comparison to the stainless steel. The protective efficiency [7] calculated from corrosion current density also indicates NCD-DLC films offer the best protection among the uncoated samples up to 81.3%. In general, samples in the corrosion behavior with lower current density and higher potential indicate better corrosion resistance [8]. An improvement in the NCD-DLC corrosion resistance is evidenced by a shift of the polarization curve towards the region of lower current density and higher potential. Even DLC films presented the best protective effect at high anodic potentials, with a greater tendency to passivate, the presence of nanoporous on its surface increase its corrosion current density.

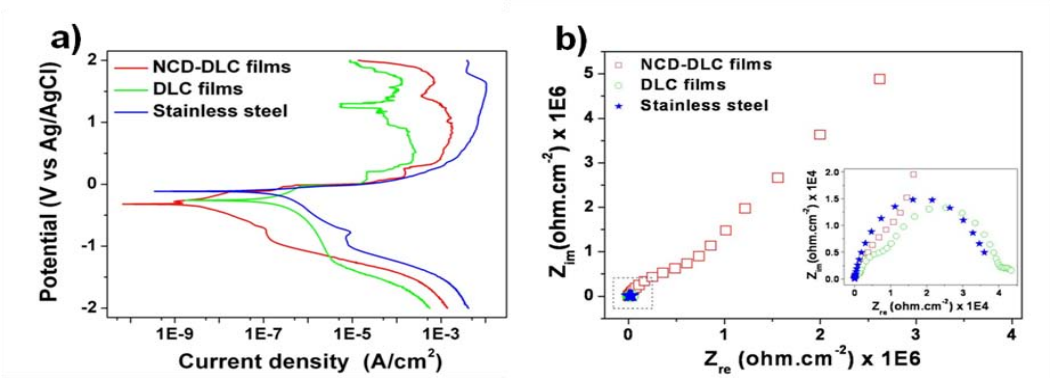

Figure 1. a) Potentiodynamic polarization curves of stainless steel, DLC and NCD-DLC films in NaCl at room temperature. b) Nyquist plot of stainless steel, DLC and NCD-DLC films, with an enlargement of the region within the rectangular box.

Table 1. Electrochemical parameters obtained from potentiodynamic polarization curves in NaCl at room temperature.

Samples	E_{corr} (mV)	i_{corr} (nA/cm²)	Protective efficiency (%)
Stainless steel	-0.117	0.359	-
DLC films	-0.241	1.740	-748.8
NCD-DLC films	-0.321	0.067	81.3

The Nyquist plots determined by electrochemical impedance spectroscopy (EIS) in Fig. 1b show the different corrosion behavior of the samples after immersion in NaCl. NCD-DLC films present superior impedance in comparison to the pure DLC and the stainless steel. The enhancement in corrosion resistance of the NCD-DLC samples can be attributed to the reduced electrical conductivity caused by the intrinsic chemical inertness of the NCD-DLC films in comparison to the uncoated samples [8]. In addition, NCD-DLC films can act as a passive film to prevent aggressive ions from attacking the substrate and thereby improve the corrosion resistance of 316L stainless steel (Fig. 2). The chloride (Cl^-) ions of the NaCl solution attack the protective oxide layer on 316 stainless steel surface, penetrating to the austenite matrix and resulting in pitting corrosion [9]. The NCD-DLC samples show very little pitting corrosion. NCD particles may occupy the nanoporous in DLC films, preventing the attacking of the Cl^- ions. The SEM images of NCD-DLC film after the electrochemical corrosion test (Fig. 2b) shows minor NCD particles that did not belong to the film surface (Fig. 2a). These NCD particles probably block the attacking of Cl^- ions, forming a barrier against the corrosion. From the results here presented, it is possible to see NCD-DLC films improving DLC and stainless steel electrochemical corrosion resistance, becoming a potential candidate for an anti-corrosion material in industrial applications.

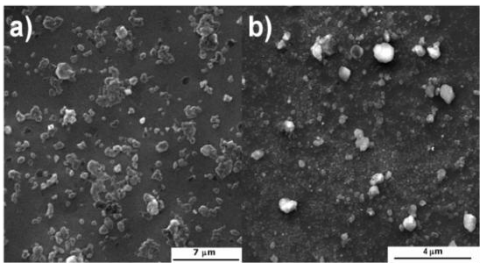

Figure 2. SEM images of NCD-DLC films (a) before and (b) after the electrochemical corrosion tests.

Concerning space application, some studies is in progress in order to get higher hardness and low friction coefficient when diamond nanoparticles under 10 nm is incorporated in DLC films.

On the other hand, due to TiO_2 photo-semiconductor properties, it may find an application as antibacterial agent for the decomposition of organisms [10-11]. TiO_2 in the anatase crystalline form is a strong bactericidal agent when exposed to near UV-light [12]. TiO_2 nanoparticles with average particle size of 21 nm, in anatase crystalline form were dispersed in hexane at 0.1, 0.5 and 1.0 g/L. These dispersions replaced the pure hexane during the DLC deposition. The antibacterial activity of the TiO_2-DLC films was determined using *Escherichia coli* ATCC 25922. More details about the antibacterial test methodology can be found in our previous publication [13].

Figure 3a shows the antibacterial activity of the stainless steel coated and non-coated with DLC and TiO_2-DLC films in different TiO_2 concentrations. The pure DLC films killed at about 32.5% of the total bacteria content. However, the bactericidal effect of TiO_2-DLC films was increasing with the increasing of TiO_2 content. The exact killing mechanism(s) underlying the TiO_2 photocatalytic reaction is not yet well understood. Huang et al. [10] proposed a detailed mechanism for the bactericidal effect of TiO_2 photocatalytic reaction. They pointed out the initial oxidative damage takes place on the cell wall, where the TiO_2 photocatalytic surface makes first contact with intact cells. Cells with damaged cell wall are still viable.

After eliminating the protection of the cell wall, the oxidative damage takes place on the underlying cytoplasmic membrane. Photocatalytic action progressively increases the cell permeability, and subsequently allows the free efflux of intracellular contents that eventually leads to cell death.

From a physicochemical point of view, the adhesion of bacteria cells to a surface is determined by the interplay of electrostatic and hydrophobic/hydrophilic interactions. The interfacial free energy of adhesion (ΔF_{Adh}) for bacteria to attach the coatings was calculate according to Schneider [14]. The as-deposited DLC films presented ΔF_{Adh} = +17.6 mJ/m^2. According to the thermodynamic theory, the bacterial adhesion is unfavorable if the work of adhesion is positive. The TiO_2-DLC films produced from 1.0 g/L TiO_2 in hexane presented ΔF_{Adh} = -5.2 mJ/m^2. In this case, the bacterial adhesion is favourable. Figure 3b compared the theoretical values of work of adhesion with the practical results of antibacterial activity. The good correlation coefficient (R^2 = 0.9999) shows that the bactericidal mechanism suffers influences not only from the presence of TiO_2 nanoparticles on the DLC surface, but also from the interaction between the nanoparticles and the DLC film, changing its proper characteristics. These results suggest that as the TiO_2 content in DLC films increased, they become thermodynamically favorable to bacterial adhesion, increasing the direct contact between bacteria and more TiO_2 nanoparticles, promoting the increase in the bactericidal activity.

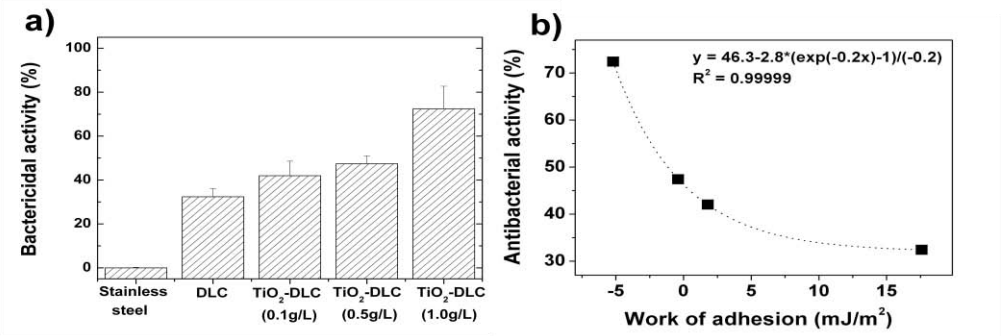

Figure 3. a) Antibacterial activity of the stainless steel coated and non-coated with DLC and TiO_2-DLC films in different TiO_2 concentrations. b) Antibacterial activity vs. work of adhesion.

In this manuscript, it was reported the main results obtained in our laboratories from the production and characterization of nanoparticle-incorporated DLC films. NCD particles improve DLC and stainless steel electrochemical corrosion resistance, reducing the pitting corrosion. NCD-DLC films prevented aggressive ions from attacking metallic surfaces, becoming a potential candidate for an anti-corrosion material in industrial applications. In addition, TiO_2 nanoparticles increased DLC antibacterial activity against *E. coli*. Thermodynamic approaches confirm these results due to the increasing of interaction between bacteria and the studied films. In general, DLC films have a huge range of applications. As it was demonstrated in this manuscript, the nanoparticle-incorporated DLC films can modified the DLC structure increasing the range of applications with new scientific and technological applications.

The authors are very thankful to CNPq and FAPESP for the financial support.

References

1. L.F. Bonetti et al., V.J. *Thin Solid Films* 515 (2006) 375.
2. C. Donnet et al., G. *Surf. Coat. Technol.* 120 (1999) 548.
3. F.R. Marciano et al., V.J. *Synth. Met.* 159 (2009) 2167.
4. F.R. Marciano et al., *Thin Solid Films* 517 (2009) 5739.
5. M.A.S. Oliveira et al., *Diamond Relat. Mater.* 12 (2003) 2136.
6. E. Liu and H.W. Kwek, *Thin Solid Films* 516 (2008) 5201.
7. H.G. Kim et al., *Diamond Relat. Mater.* 14 (2005) 35.
8. J.V.Manca et al., *J. Microelectron Reliab.* 39 (1999) 269.
9. H.P. Feng et al., *Mater. Sci. Eng. A* 347 (2003) 123.
10. Z. Huang et al., *J. Photochem. Photobiol. A. Chem.* 130 (2000) 163.
11. W. Shun-Wen et al., L. *Trans. Nonferrous Met. Soc. China* 18 (2008) 1145.
12. J.C. Ireland et al., *Appl. Environ. Microbiol.* 59 (1993) 1668.
13. F.R. Marciano et al., *J. Colloid Interf. Sci.* 340 (2009) 87.
14. R.P. Schneider et al., *J. Colloid Interface Sci.* 182 (1996) 204.

Complete versions of this manuscript were published in Synthetic Metals 159 (2009) 2167, and Thin Solid Films 517 (2009) 5739.

Stoney Equation limits for samples deformed as a cylindrical surface

Pureza, J. M.[a]*, Neri, F.[b], Lacerda, M. M.[b],

[a] Department of Mechanical Engineering, Santa Catarina State University, UDESC - Joinville - Brazil
[b] Department of Physics, Santa Catarina State University, UDESC - Joinville - Brazil
* e-mail: pureza@joinville.udesc.br

In a previous work, Pureza et al [1] proposed an approach for the evaluation of the stress in thin films deposited on substrates much thicker than itself. This problem is a relevant issue for several areas of science [2-9], being the theme of a recent review [10] in commemoration of 100 years of the first description of the problem, proposed by Stoney in 1909 [11] who considered the sample as an one-dimensional plate. The Stoney equation indicates a linear relationship between the film stress (σ) and its bending, being straightforwardly modified for two-dimensional systems with small deformation by including the substrate Poisson ratio (ν_s) [12], as seen in equation (1).

$$\sigma = \frac{E_s \cdot t_s^2}{6 \cdot (1-\nu_s)\, t_f} K \qquad (1)$$

where E_s is the substrate Young modulus, t_s e t_f are the substrate and film thickness, respectively, and K is the film curvature. It has become the standard expression for the analysis of this problem with reasonable agreement with experimental results. However, Stoney equation does not take into account relevant aspects like the non-uniformity of the stresses as well as the tri-dimensionality and the boundary conditions of the samples. Such aspects gave rise to semi-empirical modifications, with little experimental agreement [12-14] and more elaborated models (see e.g. [15] and references therein, [1,16-18]), as well as finite-element simulations that present local dependence to stress distribution [3,19].

Finot et al [3] using a finite element analysis identified three distinct regimes for the evolution of curvature, which are dependent on the quantity $A = \sigma\, t_f\, l_s^2\, t_s^{-3}$, where l_s is the characteristic size of the sample: (I) for lower values of A, the deformation has a spherical shape and Stoney equation is satisfied considering 10% of error as acceptable; (II) as the parameter A increases, deformation maintains the spherical shape but Stoney equation looses validity and (III) for even larger values of A, Stoney equation is no longer valid and the sample undergoes two abrupt changes, initially to an ellipsoidal shape and finally to a cylindrical shape.

In the previous work [1], by means of the minimization of the deformation energy, we derived an expression for the thin film stress when the deformation maintains the spherical shape (regimes I and II in Finot et al [3]). We considered samples with thickness ratio $t_f/t_s<<1$, a assumption that allows the simplification of the deformation energy of the sample and consider that the substrate thickness change is a lower order term. So, the stress of the film is written in terms of the curvature K of the sample, as seen in equation (2)

$$\sigma_\theta = \sigma_\varphi = \frac{E_s}{6} \frac{1}{1-\nu_s-2\nu_s^2} \frac{t_s^2}{t_f} K \qquad (2)$$

which is quite similar to Stoney's. Figure 1 shows agreement between this equation and Stoney's at regime I but, at regime II, results stay in between the finite element (obtained by Finot et al [3]) and the other formulations [12,14-16]. However, the analysis of the values obtained by Finot [3] using finite element simulation, see Figure 1, indicate a important change on the dependence between the curvature and the stress at regime III.

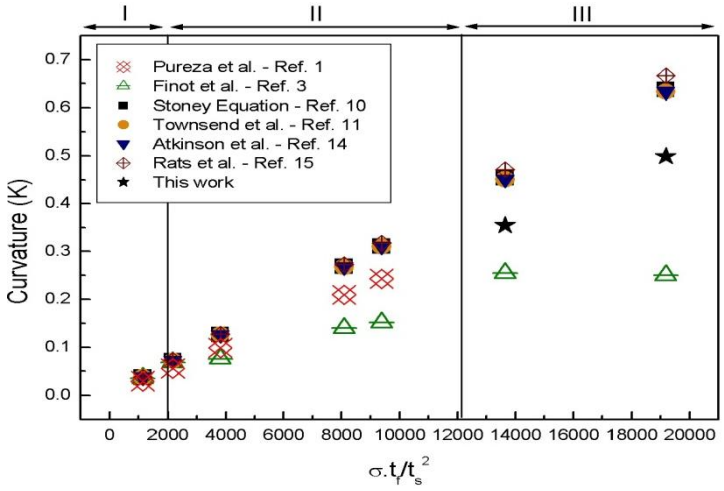

Figure 1: Sample curvature for different models.

This situation motivated us to apply the same approach to a thin film deposited on a thick substrate that is deformed as a cylindrical surface. In this situation, Figure 2 shows a three-dimensional sample that is subjected to linear and angular deformation components, given by equations (3),

$$\varepsilon_r^s = \frac{(a+b)-t_s}{t_s} = \tau - 1 \qquad \varepsilon_\theta^s(r) = \frac{(r-R)\Omega}{l_s}$$

$$\varepsilon_z^s(r) = -\frac{(r-R)\beta}{l_s} \qquad \gamma_{rz}^s(r) = \frac{\beta z}{S_s - \beta(r-R)}$$

$$\varepsilon_z^f(r) = \frac{(R-a)\beta - l_f}{l_f} \qquad \varepsilon_\theta^f(r) = \frac{(R-a)\Omega - l_f}{l_f} \qquad \gamma_{ij}^f = 0 \qquad (3)$$

where $i,j = r, \theta, z$. In the elastic regime, the film and substrate stress states are described by equations (4)

$$\sigma_i^\alpha = \frac{E_\alpha}{1-\nu_\alpha-2\nu_\alpha^2}\left[(1-\nu_\alpha)\varepsilon_i^\alpha + \nu_\alpha(\varepsilon_j^\alpha + \varepsilon_k^\alpha)\right] \qquad \tau_{ij}^\alpha = \frac{E_\alpha}{2(1+\nu_\alpha)}\gamma_{ij}^\alpha \qquad (4)$$

where $\alpha = s,f$. The deformation energy is simplified by the fact that the film is very thin and is given by the integrals in equation (5)

$$U = U_s + U_f = \frac{1}{2}\int(\sigma_i\varepsilon_i + \tau_{ij}\gamma_{ij})dz\cdot dr + t_f\frac{1}{2}\int(\sigma_i\varepsilon_i + \tau_{ij}\gamma_{ij})dz \qquad (5)$$

with the limits:

$$z \in \left(-\frac{S_s}{2} + \frac{\beta}{2}(r-R), \frac{S_s}{2} - \frac{\beta}{2}(r-R)\right) \text{ and } r \in [R-a, R+b]$$

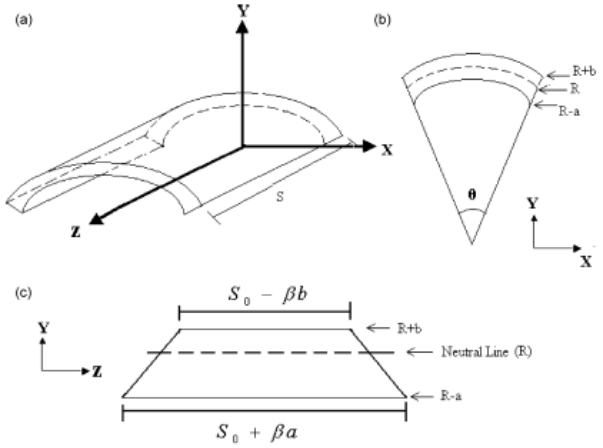

Figure 2: Projections of deformed sample as a cylindrical surface.

Finally, taking into account that changes in the substrate thickness (t - t_s) is a lower order term and making use of dimensionless variables, the energy (U) is written in the form of equations (6)

$$\overline{U} = D(1+\frac{\sigma\beta}{2}+\omega)\left\{(1-\nu_f)\left[(\delta l+\frac{\sigma}{2}\beta+\omega)^2+(\delta l+\frac{\sigma-2\Sigma}{2}\beta+\omega)^2\right]+2\nu_f(\delta l+\frac{\sigma}{2}\beta+\omega)(\delta l+\frac{\sigma-2\Sigma}{2}\beta+\omega)\right\}+$$
$$+\left(\frac{\beta^2}{4}+\frac{1-\nu_s}{1-2\nu_s}\Sigma^2\Omega^2\right)+\omega\left(\frac{\beta^2}{4}-2\frac{1-\nu_s}{1-2\nu_s}\Sigma\frac{\Omega^2}{\beta}+\frac{1-\nu_s}{1-2\nu_s}\Sigma^2\Omega^2+\frac{2\nu_s}{1-2\nu_s}\Sigma^2\Omega\right)+$$
$$+\left(\frac{\sigma^2}{12}+\frac{\omega^2}{\beta^2}\right)\left(\frac{1-\nu_s}{1-2\nu_s}\Omega^2-2\frac{1-\nu_s}{1-2\nu_s}\Sigma\Omega^2\beta^2+\frac{1-\nu_s}{1-2\nu_s}\beta^2-\frac{2\nu_s}{1-2\nu_s}\Omega\beta+\frac{2\nu_s}{1-2\nu_s}\Sigma\Omega\beta^2\right)+$$
$$+\left(\frac{\sigma^2\omega}{4}+\frac{\omega^3}{\beta^2}\right)\left(\frac{1-\nu_s}{1-2\nu_s}\Omega^2+\frac{1-\nu_s}{1-2\nu_s}\beta^2-\frac{2\nu_s}{1-2\nu_s}\Omega\beta\right)$$

(6)

$$D=\frac{E_f}{E_s}\frac{1+\nu_s}{1-\nu_f-2\nu_f^2}\frac{t_f}{t_s};\qquad \sigma=\frac{t_s}{l_s};\qquad \omega=2\beta\frac{a-b}{l_s};\qquad \delta l=\frac{l_f-l_s}{l_s}$$

The minimum energy configuration of the system (τ, ω e Ω)$_{min}$ is obtained by the following Lagrangean equations:

$$\frac{\partial\overline{U}}{\partial\beta}=\frac{\partial\overline{U}}{\partial\omega}=\frac{\partial\overline{U}}{\partial\Omega}=0 \qquad (7)$$

An exact solution of this system is extremely difficult to obtain. However, it is possible to obtain an approximate solution after the identification of dominant terms in each Lagrangean equation, showed as equation (8)

$$\Omega\cong\frac{\nu_s}{1-\nu_s}\left(\beta-\frac{12\omega^2}{\sigma^2\beta}\right);\qquad \omega\cong-(1-\nu_s)\left[\frac{\beta^2}{8}+D\left(\delta l+\sigma\beta\right)\right]\qquad \delta l=-\frac{1}{6D}\frac{\sigma\beta}{1-2\nu_s}$$

(8)

In such a way that the stress of the film is given by equation (9)

$$\sigma_\theta\cong\sigma_r\cong\frac{E_s}{6}\frac{1}{1-\nu_s-2\nu_s^2}\frac{t_s^2}{t_f}K\left(1+\frac{t_sK}{2}\right)^{-1} \qquad (9)$$

with no relevant difference to the results obtained in Ref. 1 (see equation 2). The linear relationship between the stress and the curvature of the sample, as proposed by Stoney, is preserved , but the ($2\nu_s$)-term plays a relevant role for substrates with $\nu_s \geq 0.25$, which includes most of metals and ceramic-like materials and the formula indicates a divergence of the stress when $\nu_s = 0.5$, a critical value corresponding to a truly incompressible (theoretical) material [20].

However, although the results stay in between the values obtained by other formulations and by finite element simulation (see Figure 1, for regime III), this approach was not able to identify a change in the behaviour of the curve at the transition from regime II to regime III. This situation could be better understood by analysing a sample that is deformed as a ellipsoidal surface, in such a way that the spherical and cylindrical surfaces would correspond to eccentricity limits of the figure and maybe the transitions would arise from the relationship with the stress of the film.

References

1. Pureza, J. M., Lacerda, M. M., De Oliveira, A. L., Fragalli, J. F., Zanon, R. A. S., Appl. Surface Sci., **62,** 4438 - 4444 (2009)
2. Geim, A. K. and Novoselov, K. S. Nature Mater. **6,** 183 - 191 (2007).
3. Finot, M., Blech, I. A., Suresh, S. and Fujimoto, H. J. Appl. Phys., **81,** 3457 – 3464 (1997).
4. Espinosa, H. D. et al. Appl. Phys. Lett., **89,** 73111 (2006).
5. Lacerda, M.M., Chen, Y.H., Chung, Y.W., Guruz, M.U. and B. Zhou. J. Vac. Sci. Tech. A, **17,** 2915 - 2919 (1999).
6. Luxon, J. T. and Parker, D. E. *Low Power Laser Applications*, Prentice-Hall (1985).
7. Zhang,Y., Wang, W. H. and Greer, A. L. Nature Mater. **5,** 857 – 860 (2006).
8. Hoffman, D. W. and Thornton, J. A. J. Vac. Sci. Tech., 20, 355 - 358 (1982).
9. Suo, Z. Fracture in Thin Films, Encyclopedia of Materials: Science and Technology. 2nd edition, pp. 3290 - 3296, Elsevier Science (2001).
10. Janssen, G. C. A. M., Abdalla, M. M., Van Keulen, F., Pujada, B. R.and Van Lenrooy, B. Thin Sol. Films 517, 1858-1867 (2009).
11. Stoney, G. G. Proc. R. S. London, Ser. *A*, **82,** 172 (1909).
12. Townsend, P. H., Barnett, D. M. and Brunner, T. A. J. Appl. Phys., **62,** 4438 - 4444 (1987).
13. Flinn, P. A., Gardner, D. S. and Nix, W. D. IEEE Transactions on Electron Devices, **34,** 689 - 699 (1987).
14. Schafer, J., Nafe, H. and Aldinger, F. J. Appl. Phys. **85**, 8023 (1999) and Atkinson, A. Br. Ceram. Proc. **54**, 1 (1995).
15. Klein, A. C. J. Appl. Phys., **88,** 5487 - 5489 (2000).
16. Rats, D., Bimbault, L., Vandenbulcke, L., Herbin, R. and Badawi, K. J. Appl. Phys. **78**, 4994 (1995) and Brenner, A. and Senderoff, S. J. Res. Natl. Bur. Stand. **42**, 105 (1949).
17. Timoshenko, S. *Theory of Plates and Shells* (McGraw-Hill, New York, 1959).
18. Jawad, M. H. *Theory and Design of Plates and Shells Structures*, Chapman and Hall (1994).
19. Blech, I. A., Blech, I. and Finot , M. J. Appl. Phys., **97,** 113525 (2005).
20. Y. F. Li, B. Yao, Y. M. Lu, C. X. Cong, Z. Z. Zhang, Y. Q. Gai, C. J. Zheng, B. H. Li, Z. P. Wei, D. Z. Shen, and X. W. Fan, L. Xiao, S. C. Xu, and Y. Liu. App. Phys. Lett. **91**, 021915 (2007).

A complete version of this manuscript was published in Applied Surface Science 256 (2010) 4408.

Electrochemical behavior of Ni-P-SiC composite coatings: Effect of heat treatment and SiC particle incorporation

C. F. Malfatti[*,a], J. Z. Ferreira[b], C. T. Oliveira[c], E. S. Rieder[d], J-P Bonino[e]

[a] DEMET/PPGEM/ Universidade Federal do Rio Grande do Sul
[b] DEMAT/PPGEM/ Universidade Federal do Rio Grande do Sul
[c] PROPTEC/ICET/GEMA/ Centro Universitário Feevale
[d] Post Graduation Program in Engineering, Universidade Luterana do Brasil
[e] Institut Carnot - CIRIMAT, Unité Mixte de Recherche CNRS-UPS-INP (n°5085), Université Paul Sabatier, Toulouse-France.

Abstract

This paper describes the effects of heat treatment and of SiC particle incorporation on the electrochemical behavior and physical structure of Ni-P (17 at% P) composite coatings. The deposits were obtained by electrodeposition with various contents of SiC particles in the plating bath and heat treated at 420 °C. The physical structure was investigated by Inductively Coupled Plasma Atomic Emission Spectrometry (ICP-AES), X-Ray Diffraction (XRD) and Scanning Electron Microscopy (SEM – image analysis). The electrochemical behavior of the resultant composite coatings was determined by chronopotentiometry and electrochemical impedance spectroscopy in 0.6 M NaCl solution at pH 6. Heat treatment showed a positive effect on the electrochemical behavior of Ni-P coatings, shifting the open circuit potential towards less active potentials. The incorporation of SiC particles inhibited pit nucleation on the Ni-P composite coating, with or without post heat treatment. However, heat treatment in the Ni-P-SiC seemed to induce cracks in the metallic matrix, initiating at the SiC particles, possibly caused by the contraction in the metallic matrix. The cracked structure promoted localized corrosion, while coatings without heat treatment resulted in a general and uniform corrosion.

Keywords: composite materials, corrosion, electrochemical reactions, Ni-P-SiC.

Introduction

Ni-P alloys have been studied in the last few decades due to their characteristics concerning the effect of phosphorous content on its crystal structure [1,2]. Crystalline Ni-P structures can be obtained, though, by heat treatment above 350 °C [1]. It has been reported that the amorphous form, containing no grain boundaries and structure defects, results in coatings with outstanding mechanical and corrosion properties. Ni-P alloys, however, present low hardness and consequently low wear resistance, restraining their application in industry. Structures with better wear resistance have been successfully achieved by the incorporation of ceramic particles in the metallic matrix, such as SiC, Al_2O_3, Cr_2O_3 and TiO_2 [3-9]. A remarkable improvement in the resistance to localized corrosion of Ni-SiC composite coatings was observed with alloys containing sub-micron SiC particles [10]. This work aims at studying the effects of heat treatment and of the particle incorporation on the electrochemical behavior of Ni-P and Ni-P-SiC (17% at. P) composite coatings containing various amounts of embedded SiC particles, in 0.6 M NaCl.

Experimental

Ni-P and Ni-P-SiC (17 % at. P) composite coatings with varying amounts of incorporated SiC particles were obtained by electrodeposition. The plating bath consisted of $NiSO_4$ 50 $g{\cdot}L^{-1}$, $NiCl_2.6H_2O$ 60 $g{\cdot}L^{-1}$, H_3PO_3 20 $g{\cdot}L^{-1}$, H_3PO_4 50 $g{\cdot}L^{-1}$, Na_2SO_4 50 $g{\cdot}L^{-1}$, containing 0, 40, 80 and 200 $g.L^{-1}$ of SiC particles (with a mean diameter of 600 nm [11]) in suspension, at pH 2. The substrate and counter electrode were made of copper and nickel, respectively. Electrodeposition was carried out at 0.1 $A{\cdot}cm^{-2}$ (which resulted in 50 μm thick coatings, measured by optical microscopy). After the process, the specimens were heat treated at 420 °C for 1 h in N_2 atmosphere. The concentration of SiC embedded in the Ni-P matrix (volume %) was determined by Inductively Coupled Plasma Atomic Emission Spectrometry (ICP-AES), with an error of 2 wt.%. The number of incorporated particles per unit area (particles/μm^2) was determined by image analysis using Scanning Electron Microscope (SEM - JEOL JSM 6400). The crystalline state and thickness of the deposits were obtained by X-Ray Diffraction analysis (XRD), using CuKα (λ=1,5418Å) radiation in the Phillips X´Pert diffractometer, and by optical microscopy, respectively. Open Circuit Potential (OCP) and Electrochemical Impedance Spectroscopy (EIS) were performed in 0.6 M NaCl solution (pH 6) using an EG&G PAR 273 potentiostat and a Solartron 1250 frequency response analyzer. The EIS measurements were carried out at the OCP using a perturbation of 10 mV amplitude signal and frequency range of 100 kHz to 10 mHz. After 1200 h of immersion in the NaCl solution, the coatings were observed in the SEM.

Results and Discussion

The correlation between the amount of SiC in the coating, expressed in volume percent and number of incorporated particles per unit area (particles/μm^2), and the concentration of particles suspended in the solution showed that the volume of SiC particles (vol. %) embedded in the metallic matrix increased with increasing particle concentration in the solution, reaching a saturation point at about 17 vol.% under the conditions used. The increase of particles concentration in the electroplating bath induced a selective phenomenon, promoting smaller particle embedded in the coating (Figs. 1a, b and c).

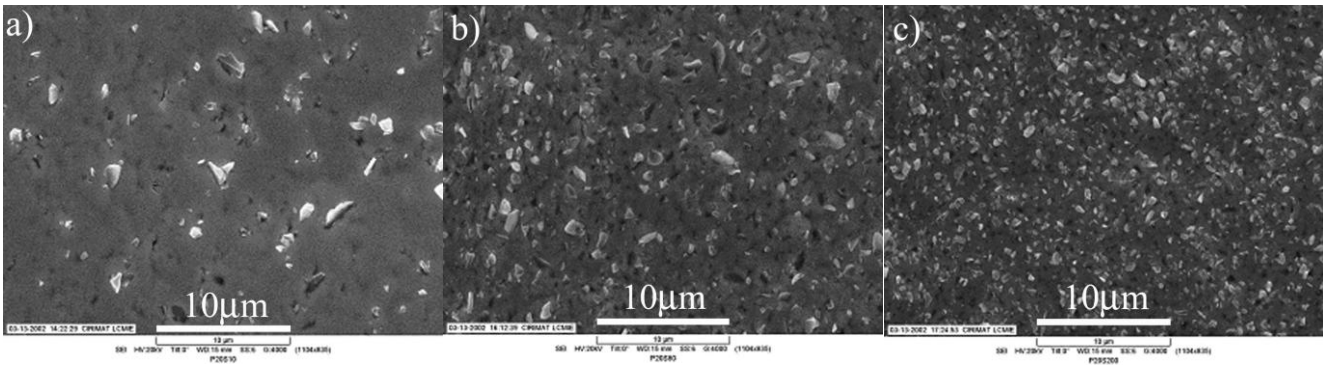

Fig. 1: SEM micrographs of composite Ni-P-SiC coatings obtained from electrolytes with different concentrations of SiC particles: a) 10 g.L^{-1}; b) 80 g.L^{-1} and c) 200 g.L^{-1}.

This phenomenon, also observed by other authors in similar systems [5,11], may be based upon the probability of mechanical interaction between the cathode and the suspended particles. The particle is completely incorporated into the metallic matrix only when the deposit reaches a certain thickness, so that the ejection, caused by the arriving particles, is restrained. The time required for complete particle incorporation is, therefore, a size function, *i.e.*, bigger particles need longer periods for their complete incorporation into the metallic matrix [12]. The incorporation of particles must not affect phosphorous content in the deposit, which remained constant at about 17 at.%. Heat treatment at 420 °C for 1 h in N_2 atmosphere resulted in the crystallization of nickel followed by precipitation of nickel phosphide, Ni_3P ($Ni \rightarrow Ni_{(cfc)} + Ni_3P$), obtained by the X-ray diffraction measurements results. A transition from amorphous to crystalline structure is accompanied by a volume contraction. This is in agreement with the observations for this system, that the coatings suffered about 5 % reduction in thickness with thermal treatment. This structural change and associated contraction, may influence cohesion between the SiC particles and the metallic matrix and, therefore, affect properties such as corrosion resistance.

Open circuit potential measurements with time showed that thermal treatment of Ni-P coatings (without particles) displaced the OCP towards less active values compared to the as-plated specimens. Heat treatment also caused the shift of the OCP to less active values in the first 100 hours. After this period of time, it showed similar behavior as that of the specimens without thermal treatment, i.e. with a stable OCP.

The electrochemical impedance results exhibited one time constant and the fitting parameters were equivalent to the circuit Rs(RpCdl) where Rs is the solution resistance, Rp the polarization resistance, and Cdl the double layer capacitance. The results are presented using Nyquist diagrams, Figs. 2 and 3. The spectra obtained for Ni-P and Ni-P-SiC coatings without thermal treatment in the first hour of immersion in 0.6 M NaCl, pH 6, showed very similar values of polarization resistance (40 kΩ·cm^2 - 45 kΩ·cm^2), Fig. 2a. The same behavior was observed for the heat treated specimens (Fig. 2b), having in this case polarization resistance of the order of 20 kΩ·cm^2. After 1200 hours of immersion, while the as-plated Ni-P coatings (without particles) showed polarization resistance of the order of 100 kΩ·cm^2 (Fig. 3a), the heat treated specimens exhibited 13 kΩ·cm^2 (Fig. 3b).

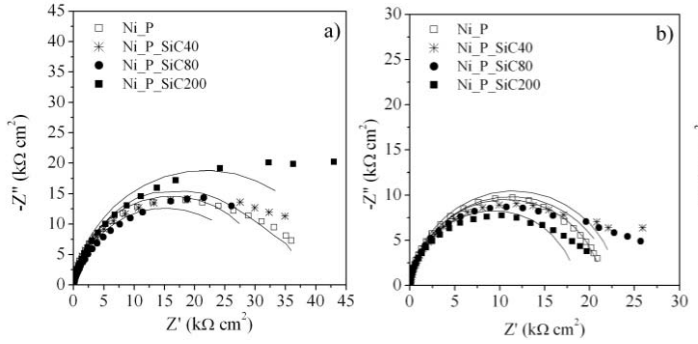

Fig. 2: Nyquist plots for Ni-P, Ni-P-SiC40, Ni-P-SiC80, Ni-P-SiC200 coatings at the OCP, after immersion in 0.6 M NaCl, pH 6, for 1 hour: a) as-plated and b) heat-treated.

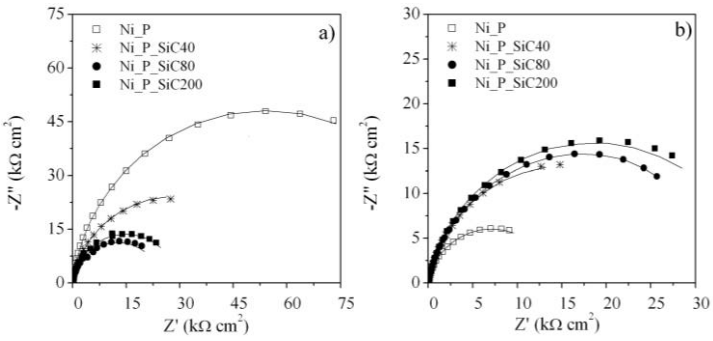

Fig.3: Nyquist plots for Ni-P, Ni-P-SiC40, Ni-P-SiC80, Ni-P-SiC200 coatings at the OCP, after immersion in 0.6 M NaCl for 1200 hours: a) as-plated and b) heat-treated.

Other author [13] have also observed, by impedance studies, higher polarization resistance for the non-treated Ni-P alloys compared to the heat treated specimens and attributed this effect to the crystal structure of the coating. Specimens without thermal treatment are amorphous and are supposed to exhibit better corrosion resistance. Nevertheless, the resistance values for the as-plated Ni-P coatings oscillated with time of immersion in NaCl solution, indicating that this system is less stable than the others. Pitting corrosion was observed, by SEM micrographs, on the as-plated Ni-P coatings (Fig. 4a and b), which was not observed for the heat-treated specimens (Fig. 4c). For other coatings, except for the as-plated Ni-P, the Rp values, with or without heat treatment, were very unstable up to 100 hours of immersion, in the same manner as obtained for the OCP. After this time, a dark grey film formed on the surface and more stable values of polarization resistance were obtained. Similar results were documented by Krolikowski *et al.* [14] and Diegle *et al.* [15].

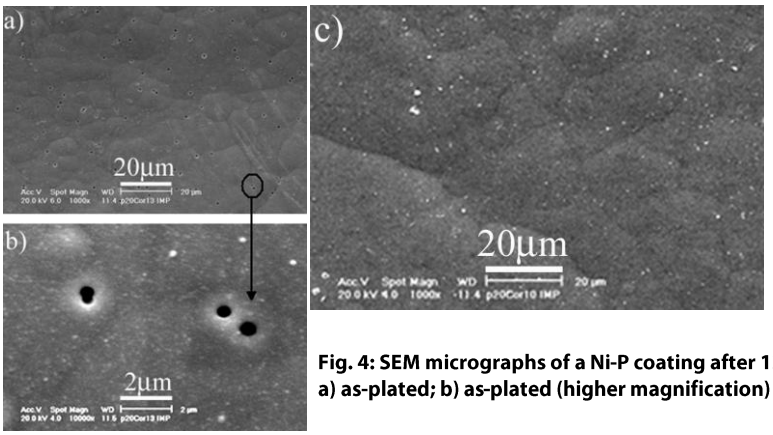

Fig. 4: SEM micrographs of a Ni-P coating after 1200 hours immersed in 0.6 M NaCl, pH 6: a) as-plated; b) as-plated (higher magnification) and c) heat-treated.

The incorporation of SiC particles in the Ni-P coatings affected the polarization resistance (Figs. 3a and b). Lower Rp values were obtained for the as-plated Ni-P-SiC specimens, and higher values for heat treated Ni-P-SiC, compared to the Ni-P coatings. Higher values, with increasing SiC content in the coating, were also obtained by other author [10]. Variations in electrochemical activity of Ni-P-SiC coatings may be related to the surface area effectively exposed to the electrolyte, which is the Ni-P area, once SiC particles are electrochemically inactive. Structural changes in the Ni-P matrix itself with the incorporation of particles are less likely.

The as-plated Ni-P-SiC coating, immersed in NaCl solution for 1200 h, exhibited general corrosion on the surface of the Ni-P matrix (Fig. 5a), while the heat treated Ni-P-SiC specimens showed localized corrosion at the interface between Ni-P and SiC particles (Fig. 5b). With thermal treatment, structural change and contraction may occur. The contraction, which cannot be accommodated by the embedded particles, can result in fissures initiating at the particles, contributing to localized corrosion at the interface Ni-P-SiC.

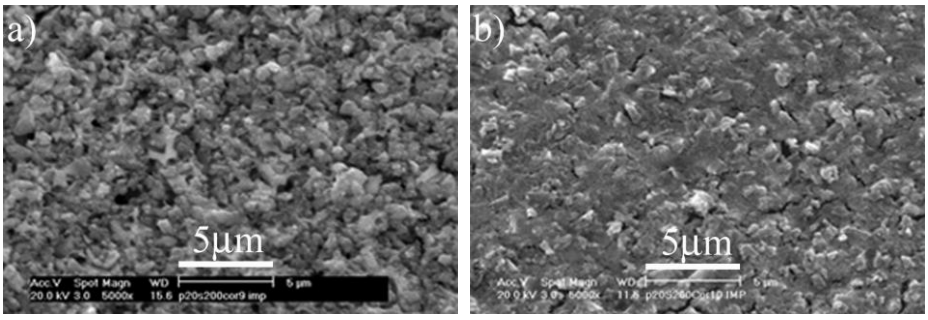

Fig. 5: SEM micrographs of a Ni-P-SiC200 coating after 1200 hours immersed in 0.6 M NaCl, pH 6: a) as-plated and b) heat-treated

Conclusions

The results obtained in this work showed that thermal treatment causes microstructural changes in the Ni-P matrix, going from amorphous to crystalline, followed by a slight contraction in the metallic matrix (5 %). These changes impact the electrochemical behavior of Ni-P coatings. Heat treatment at 420 °C for 1 hour shifts the open circuit potential towards less active values, preventing pit formation.The concentration of particles in the solution affects the particle size incorporated in the coating. The higher the concentration in solution, the smaller the particle embedded in the coating. Phosphorous content in the deposit is not affected by the embedded particles, and remained constant at about 17 %. The higher Rp observed on the as-plated Ni-P (without particles) was not related to a better corrosion resistance but with some other phenomenon occurring during the attack. The incorporation of particles in the coating results in higher polarization resistance, compared to the coatings containing only the metallic matrix (Ni-P), for heat treated specimens. Heat-treated Ni-P-SiC composite coatings, despite particle concentration or particle size, exhibit higher polarization resistance than the Ni-P coatings. The lower electrochemical activity has been associated with the smaller active surface area established by the non-conductive SiC particles.

References

1. J.-P. Bonino, S. Bruet-Hotellaz, C. Bories, P. Pouderoux, A. Rousset, *J. Appl. Electrochem.* **1997**, *27*, 1193.
2. S. Vaillant, *PhD thesis*, Université Paul Sabatier, Toulouse, France, **2002**.
3. Y. Li, *Plat. Surf. Finish.* **1997,** *84*, 77.
4. S. Shawki, Z.A. Hamid, *Anti-Corr. Meth. Mater.* **1997**, *44*, 178.
5. A. Grosjean, *PhD thesis*, Université de Besançon, Besançon, France, **1998**, 215.
6. S. Vaillant, L. Datas, J-P Bonino, *Matériaux et Techniques* **2001**, *89*, 47
7. P. Lima Neto, F. J. B. Rabelo, A. M. M. M. Adam, L. A. Avaca, E. R.Gonzalez, *Interfinish* **1988**, *92*, 385.
8. H. G. Schenzel, H. Kreye, *Plating Surf. Finish.* **1990**, *77*, 50.
9. I. Apachitei, F. D. Tichelaar, J. Duszczyk, L. Katgerman, *Surf. Coat. Technol.* **2002**, *149*, 263.
10. I. Garcia, A. Conde, G. Langelaan, J. P. Celis, *Corrosion Science* **2003**, *45*, 1173.
11. C.F. Malfatti, J. Z. Ferreira, C.B. Santos, B.V. Souza, E.P. Fallavena, S. Vaillant, J.-P. Bonino, *Corrosion Science* **2005,** *47*, 567.
12. J.P. Celis, J. R. Roos, C. A Buelens, *J. Electrochem. Soc.* **1987,** *134*, 1402.
13. M.M.V. Parente, O.R. Mattos, S.L. Díaz, P. Lima Neto and F.J. Fabri Miranda, *J. Appl. Electrochem.* **2001**, *31*, 677.
14. A. Królikowski, P. Butkiewicz, *Electrochimica Acta* **1993**, *38*, 1979.
15. R. B. Diegle, N. R. Sorensen, G. C. Nelson, *J. Electrochem. Soc.* **1986**, *133*, 1769.

A complete version of this manuscript was published in Materials and Corrosion 61 (2010) DOI: 10.1002/maco.200905611

Tribology and surface characterization of brake materials

Ruth Hinrichs[1], Marcos A.Z. Vasconcellos[2], Leonardo Brunnet2, Sebastian Gonçalves[2], Evy Salcedo[3]

[1] Instituto de Geociências – Universidade Federal do Rio Grande do Sul
[2] Instituto de Física – UFRGS
[3] Departamento de Física – Universidade Federal de Santa Catarina

The lining materials of brakes pads are composites formed by hot compaction of powders including different raw materials (more than 20).These components include i) binder, that holds all components together and forms a thermally stable matrix; ii) structural materials, providing mechanical strength. Materials used are metal, carbon, glass, and/or kevlar fibres and more rarely different mineral and ceramic fibres; iii) fillers, to reduce cost and improve manufacturability. Different minerals such as mica and vermiculit are employed. Barium sulphate is another used filler; iv) frictional additives, to ensure stable frictional properties and to control wear rates of both pad and disc. The material of the brake discs is grey cast iron with 3–4 wt.% carbon. This material contains small flakes of graphite in a pearlitic matrix. Tests were performed using an automotive brake full scale dynamometer tests using AK-Master Procedure.

The friction film is observed at the surface of the cast iron disc after dynamotor tests as shown in Figure 1.

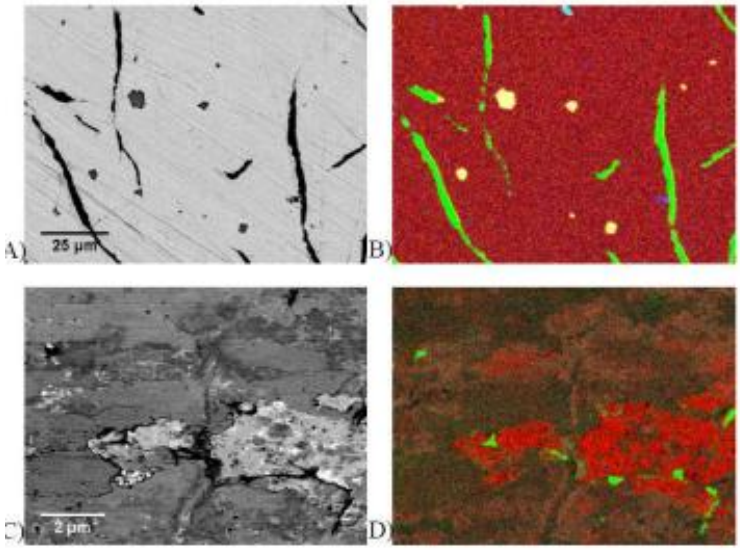

Figure 1.: Disc surface (A) BEI of the pristine grey cast iron disc revealing graphite flakes (black) in a ferritic/pearlitic matrix (light grey); dark grains are MnS 2 . (B) Composite EDS-map (iron: red, graphite: green, Mn+S: light yellow, silicon: blue, aluminum: cyan). (C) BEI of disc surface after the AK-Master friction test. Dark grey surface film (third body) is 6 composed mainly of magnetite and graphite. Light grey areas are exposed iron; bright spots correspond to tin sulfide or barium sulfate from the PMC pad. (D) Composite x-ray map (graphite: green, iron: red, oxygen: cyan, Fe + O: salmon).

In order to observe this film with Transmission Electron Microscopy (TEM), samples were prepared by using Focused Ion Beam (FIB) system as shown in Figure 2.

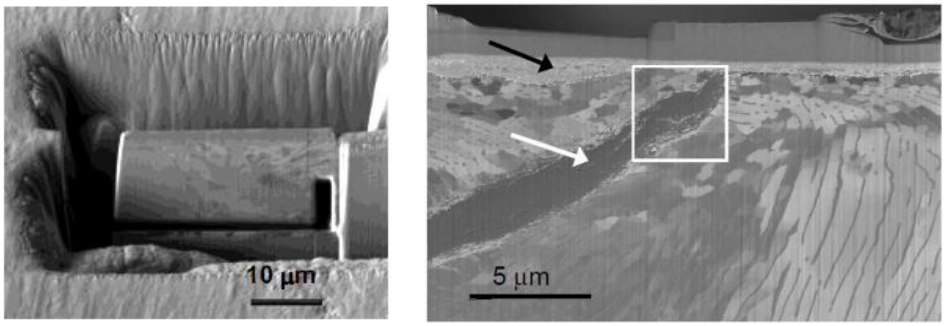

Figure 2. Ion-induced secondary electron image of the TEM lamella still bound to the disc surface. Ion-induced secondary electron image of the TEM lamella. The black arrow indicates the friction film beneath the platinum protective strip. The white arrow indicates the graphite flake diagonally crossing the plastically deformed matrix of the cast iron. The white square indicates the main region of TEM analysis.

The results of TEM presented in Figure 3 show graphite flakes of a grey cast iron brake discs became heavily disordered, with wrinkled few-layer graphenes wedged between nanoparticles of iron and magnetite, due to nanoscale mechanical cutting that occurred during the macroscopic shearing process of braking tests. FIB and EFTEM captured the process of graphite exfoliation and magnetite formation, revealing that the oxidation was fostered by the cracking due to differences in elastic moduli of iron and graphite and by the dissecting of iron into nanoparticles by graphene cutting edges. The latter mechanism will be supported further by oxidation. The anisotropic shear modulus in the graphite crystalline structure caused the delaminating of few-layer graphenes that penetrated the iron bulk, peeling off iron nanoparticles. On the other hand, the low adhesion between graphite basal planes allowed the exfoliation of few-layer graphene batches that were wedged apart by minute iron or magnetite particles [1].

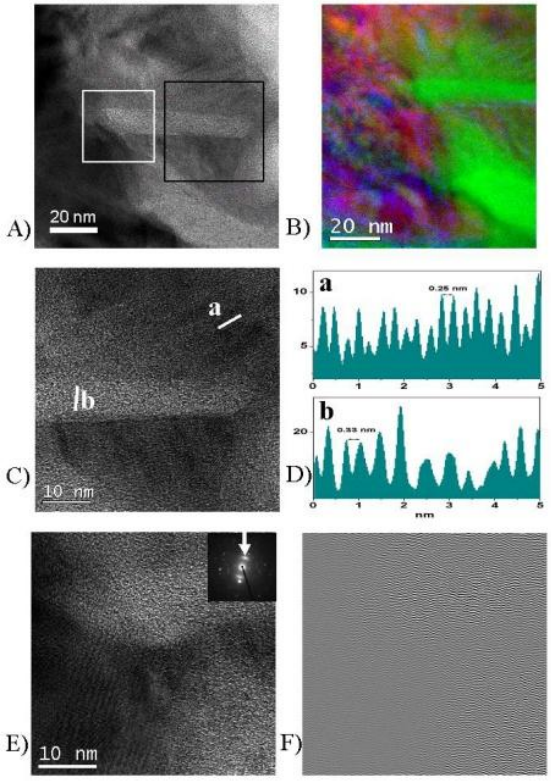

Figure 3. Micrographs, profiles, and maps of graphene exfoliation. (A) EFTEM image of a graphite rod and exfoliating graphene batches between iron-bearing grains. Black square indicates area of Figure 5 C, white one indicates Figure 5 E. (B) EFTEM composite element map (iron: red, carbon: green, oxygen: cyan). (C) High resolution micrograph of graphite between magnetite grains. Lines labeled a and b indicate the location of the contrast profiles at the right. (D) Profile a is compatible with the interplanar distances of magnetite, profile b is few-layer graphene. (E) High resolution EFTEM micrograph of the white square indicated in Figure 5 A, SAED pattern inset. (F) Inverse FFT of the graphite spots (white arrow on the SAED), showing wrinkled lattice planes.

Mössbauer spectroscopy proved to be extremely useful in the identification of iron-bearing phases, the shallow depth and large area sampling of CEMS permitted representative analysis of films on tribo-surfaces. The combination of XRD with Mössbauer Spectroscopy (see Figure 4) identified all iron-bearing compounds on the surface of complex friction couples, like PMC pad and cast iron disc counter parts, even those with low crystallinity [2].

Several publications have emphasized the role of friction films, however no reference was found concerning the presence of pyrite as part of the third body. The origin of iron sulfides has to be more thoroughly investigated and the sulfur source identified. The observation of pyrite in the film opens new questions about its effect on the tribological behavior of brakes and its presence has to be considered in amore realistic description of the braking condition. Pyrite, magnetite, and würstite were positively identified I all friction films, and hematite was ruled out as a major phase. It was shown that iron copper sulfides and iron oxide–hydroxides decomposed under frictional load.

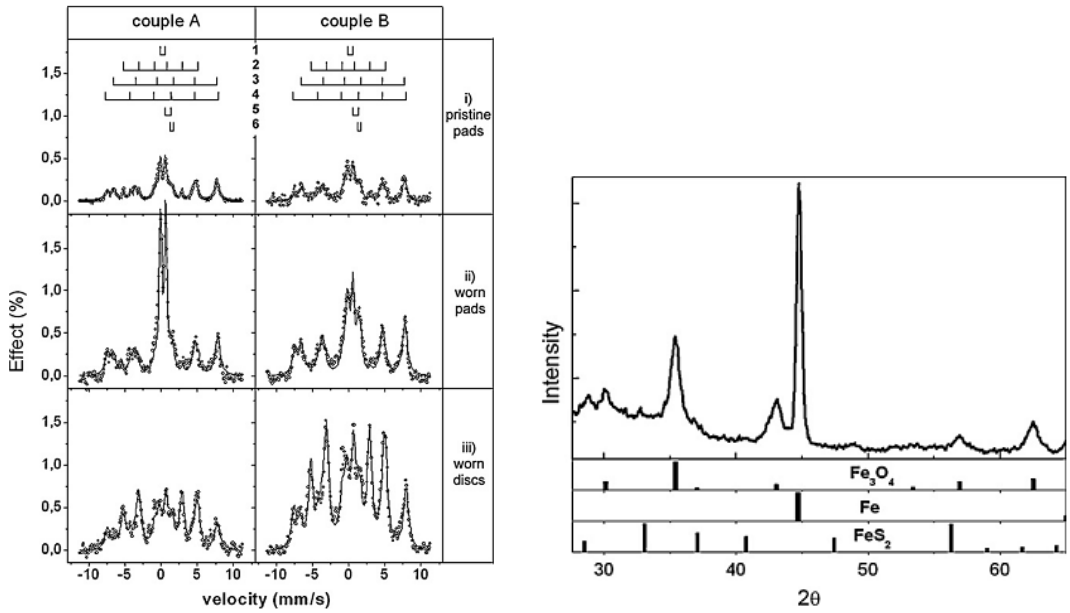

Figure 4. a) CEMS spectra from (i) pristine pads (ii) worn pads and (iii) worn discs. MS peak positions indicated on top refer to (1) pyrite, (2) a-iron, (3 and 4) magnetite, and (5 and 6) wüstite. Same %effect scale on all spectra. b) GIXRD (incidence angle 1◦) from the disc surface after the dynamometer test shows the presence of nano-crystalline magnetite (Fe3O4), a-iron (Fe) and minor amounts of pyrite (FeS2).

Based on the experimental observations of the group, computer simulation are under developmet by the Computer Simulation Group from Physics Institute at UFRGS composed by Dr. Leonardo Brunnet, Dr. Sebastian Gonçalves and Dr. Evy Salcedo (UFSC).

*A complete version of this manuscript was published in Wear 268 (**2010**) 715–720.*

List of Publications, Patents and Communications

Publications in international indexed journals:

1. Barbosa, D. C.; Melo, L. L. ; Trava-Airoldi, V. J. ; Corat E. J. . The Activation Energy for Nanocrystalline Diamond Films Deposited from an Ar/H_2/CH_4/ Hot-Filament Reactor. **Journal of Nanoscience and Nanotechnology**, v. 9, p. 3944-3948 (2009).

2. Zorzi, Janete E.; de Amorim, Cintia L.G. ; Milani, Raquel ; Figueroa, Carlos A. ; da Jornada, João A.H. ; Perottoni, Claudio A. "Ball milling-induced pyrochlore-to-tungsten bronze phase transition in RbNbWO" **Journal of Materials Research**, v. 24, p. 2035 (2009).

3. MARCIANO, F. R. ; D.A. Lima-Oliveira ; N.S. Da-Silva ; A.V. Diniz ; TRAVA-AIROLDI, V. J. ; E.J. Corat . Antibacterial activity of DLC films containing TiO2 nanoparticles. **Journal of Colloid and Interface Science**, v. 340, p. 87 (2009).

4. MARCIANO, F. R. ; MARCIANO, F. R. ; L.F. Bonetti ; N.S. Da-Silva ; TRAVA-AIROLDI, V. J. ; E.J. Corat . Diamond-like carbon films produced from high deposition rates exhibit antibacterial activity. **Synthetic Metals**, v. 159, p. 2167 (2009).

5. MARCIANO, F. R. ; MARCIANO, F. R. ; J.S. Marcuzzo ; L.F. Bonetti ; TRAVA-AIROLDI, V. J. ; E.J. Corat . Use of near atmospheric pressure and low pressure techniques to modification DLC film surface. **Surface & Coatings Technology**, v. 204, p. 64 (2009).

6. Amorim, A. ; Nascente, P.A.P. ; Trava-Airoldi, V.J. ; Corat, E.J. ; Alves, A.R. ; Moro, J.R. . Two-step growth of HFCVD diamond films over large areas. **Vacuum**, v. 83, p. 1054 (2009).

7. Marciano, F.R. ; Bonetti, L.F. ; Pessoa, R.S. ; Massi, M. ; Santos, L.V. ; Trava-Airoldi, V.J. . Oxygen plasma etching of silver-incorporated diamond-like carbon films. **Thin** , v. 517, p. 5739 (2009).

8. Barbosa, D.C. ; Almeida, F.A. ; Silva, R.F. ; Ferreira, N.G. ; Trava-Airoldi, V.J. ; Corat, E.J. . Influence of substrate temperature on formation of ultrananocrystalline diamond films deposited by HFCVD argon-rich gas mixture. **Diamond and Related Materials**, v. 18, p. 1283 (2009).

9. Marciano, F.R. ; Bonetti, L.F. ; Da-Silva, N.S. ; Corat, E.J. ; Trava-Airoldi, V.J. . Wettability and antibacterial activity of modified diamond-like carbon films. **Applied Surface Science**, v. 255, p. 8377 (2009).

10. Marciano, F.R. ; Bonetti, L.F. ; Santos, L.V. ; Da-Silva, N.S. ; Corat, E.J. ; Trava-Airoldi, V.J. . Antibacterial activity of DLC and Ag DLC films produced by PECVD technique. **Diamond and Related Materials,** v. 18, p. 1010 (2009).

11. Statuti R.P.C.C. ; RADI, P. A. ; SANTOS, L. V. ; TRAVA-AIROLDI, V. J. ; SANTOS, L. V. . A tribological study of the hybrid lubrication of DLC films with oil and water. **Wear**, v. 267, p. 1208 (2009).

12. Basso, R.; Candal, R.; Figueroa, C. A.; Wisnivesky, D.; Alavarez, F. "Influence of microstructure on the corrosion behavior of nitrocarburized AISI H13 tool steel obtained by pulsed DC plasma" **Surface and Coatings Technology**, v. 203, p. 1293 (2009).

13. Aguzzoli, C.; Tentardini, E. K.; Figueroa, C. A.; Kwietniewski, C.; Miotti, L.; Baumvol, I. J. R. "Atomic transport and chemical reaction in TiN/Ti nanolayers on plasma nitrided steel" **Applied Physics. A, Materials Science & Processing**, v. 94, p. 263 (2009).

14. Portolan, E.; Baumvol, I.J.R.; Figueroa, C. A. "Electronic structure and mechanical properties of plasma nitrided ferrous alloys" **Applied Surface Science**, v. 255, p. 6661 (2009).

15. Milani, R.; Cardoso, R.P.; Belmonte, T.; Figueroa, C. A.; Perottoni, C.A.; Zorzi, J.E.; Soares, G.V.; Baumvol, I.J.R. "Nitriding of yttria-stabilized zirconia in atmospheric pressure microwave plasma" **Journal of Materials Research**, v. 24, p. 2021 (2009).

16. Kauling, A. P.; Soares, G. V.; Figueroa, C. A.; de Oliveira, R.V.B.; Baumvol, I. J.R.; Giacomelli, C.; Miotti, L. "Polypropylene surface modification by active screen plasma nitriding" **Materials Science & Engineering. C, Biomimetic Materials, Sensors and Systems**, v. 29, p. 363 (2009).

17. Basso, R. L. O.; Pimentel, V. L.; Weber, S.; Marcos, G.; Czerwiec, T.; Baumvol, I. J. R.; Figueroa, C. A. "Magnetic and structural properties of ion nitrided stainless steel" **Journal of Applied Physics**, v. 105, p. 124914 (2009).

18. HOLMBERG, Kenneth ; RONKAINEN, Helena ; LAUKKANEN, Anssi ; WALLIN, Kim ; Hogmark, Sture ; JACOBSON, Staffan ; WIKLUND, Urban ; Souza, Roberto M. ; Ståhle, Per, "Residual stresses in TiN, DLC and MoS_2 coated surfaces with regard to their tribological fracture behavior", **Wear** 267, 2142 (2009).

19. SANCHEZ, C. M., COSTA, M. E. H. M., FONSECA FILHO, Henrique D, FREIRE JUNIOR, F. L. Nitrogen incorporation into titanium diboride films deposited by dc magnetron sputtering: structural modifications. **Thin Solid Films.** , v.517, p.5683 (2009).

20. CHEMALE, L. T.; VASCONCELLOS, M. A. Z. ; HINRICHS, R ; CUNHA, J. B. M. ; CHEMALE JR, F. . Phase quantification in iron ore. **Transactions. Institution of Mining and Metallurgy. Section C. Mineral Processing & Extractive Metallurgy**, v. 118, p. 168 (2009).

21. Wolle, Carlos Frederico Brilhante ; VASCONCELLOS, M. A. Z. ; Hinrichs, Ruth ; Becker, Alex Niederauer ; Barletta, Fernando Branco . The Effect of Argon and Nitrogen Ion Implantation on Nickel-Titanium Rotary Instruments. **Journal of Endodontics**, v. 35, p. 1558 (2009).

22. Pureza, J.M.; LACERDA, M. M. ; De Oliveira, A.L. ; Fragalli, J.F. ; Zanon, R.A.S. . Enhancing accuracy to Stoney Equation. **Applied Surface Science** , v. 255, p. 6426 (2009).

23. A. Hentz, G. S. Parkinson, P. D. Quinn, M. A. Muñoz-Márquez, D. P. Woodruff, P. L. Grande, G. Schiwietz, P. Bailey, and T. C. Q. Noakes, Direct Observation and Theory of Trajectory-Dependent Electronic Energy Losses in Medium-Energy Ion Scattering, **Physical Review Letters,** 102, 096103 (2009).

24. J.M.J. Lopes, U. Littmark, M. Roeckerath, E. Durgun Özben, S. Lenk, U. Breuer,A. Besmehn, A. Stärk, P.L. Grande , M.A. Sortica, C. Radtke, J. Schubert, S. Mantl, Isotopic labeling study of oxygen diffusion in amorphous LaScO3 high-κ films on Si(100) and its effects on the electrical characteristics, **Applied Physics A** 96 447 (2009).

25. M. Shubeita, R. C. Fadanelli, J. F. Dias, P. L. Grande, C. D. Denton and I. Abril, R. Garcia-Molina, N. R. Arista, Role of electronic excitations in the energy loss of H2 projectiles in high-k materials, **Physical Review B** 80, 205316 (2009).

26. M. A. Sortica, P. L. Grande, G. Machado, and L. Miotti, Characterization of nanoparticles through medium-energy ion scattering, **Journal of Applied Physics,** 106 1 (2009).

27. M. H. Oliveira, D.S. Silva, S. D. S. Côrtes, Diamond like carbon used as antireflective coating on crystalline silicon solar cells, **Diamond and Related Materials**, V. 18, 1028 (2009).

28. ALVES C. ; GALVÃO, N. K. DE A. M.; T Belmonte ; G Henrion . OES During Reforming Of Methane By Microwave Plasma At Atmospheric Pressure. **Journal of Analytical Atomic Spectrometry**, v. 24, p. 1459 (2009).

29. Sá, J.C. ; de Brito, R.A. ; Moura, C.E. ; Silva, N.B. ; Alves, M.B.M. ; Júnior, C.Alves . Influence of argon-ion bombardment of titanium surfaces on the cell behavior. **Surface and Coatings Technology**, v. 203, p. 1765 (2009).

30. Tavares, J.C.M.; Cornélio, Deborah A.; da Silva, Naisandra Bezerra; Bezerra de Moura, Carlos Eduardo; de Queiroz, Jana Dara Freires ; Sá, Juliana C. ; Alves Jr. C; de Medeiros, Silvia Regina Batistuzzo . Effect of titanium surface modified by plasma energy source on genotoxic response in vitro. **Toxicology (Amsterdam)**, v. 262, p. 138 (2009).

31. GUERRA NETO, C. L. B.; SILVA, M. A. M. DA ; ALVES C. . Osseointegration evaluation of plasma nitrided titanium implants. **Surface Engineering,** v. 25, p. 434 (2009).

32. GUERRA NETO, C. L. B.; da Silva, M. A. M. ; Alves, C. . Experimental study of plasma nitriding dental implant surfaces. **Surface Engineering**, v. 25, p. 430 (2009).

33. SOUZA, R. M. S ; ARAUJO, F. O. ; COSTA, J. A. P ; Dumelow, T ; OLIVEIRA, R. S. ; ALVES C. . Nitriding in Cathodic Cage of Stainless Steel AISI 316: Influence of Sample Position. **Vacuum**, v. 83, p. 1 (2009).

34. GUERRA NETO, C. L. B. ; SILVA, M. A. M. ; ALVES C. . In vitro study of cell behaviour on plasma surface modified titanium. **Surface Engineering,** v. 25, p. 146 (2009).

35. SÁ, J. C. ; BRITO, R. A. DE ; C.E.MOURA ; N.B.SILVA ; ALVES, M. B. DE M. ; ALVES JUNIOR, C. Influence of bombardment of titanium surfaces on the cell behavior, **Surface and Coatings Technology**, v. 203, p. 1765 (2009).

36. Oliviero, E., David, M. L., Fichtner, P. F. P. Interaction of interstitials with buried amorphous layer in silicon. **Physica Status Solidi (c).** , v.6, p.1969 (2009).

37. REBOH, S., de Mattos, A. A., Barbot, J. F., Declemy, A., Beaufort, M. F., Papale?o, R. M., Bergmann, C. P., Fichtner, P. F. P. Localized exfoliation versus delamination in H and He coimplanted (001) Si. **Journal of Applied Physics**. , v.105, p.093528 (2009).

38. Masunaga, S. H., Jardim, R. F., Fichtner, P. F. P., Rivas, J. Role of dipolar interactions in a system of Ni nanoparticles studied by magnetic susceptibility measurements. **Physical Review. B, Condensed Matter and Materials Physics**. ,v.80, p.184428 (2009).

39. SILVEIRA, F.; Alves, Maria do Carmo Martins ; STEDILE, F. C. ; PERGHER, S. B. C. ; SANTOS, J. H. Z. Microporous and mesoporous supports and their effect on the performance of supported metallocene catalysts. **Journal of Chemical Catalysis. A, Chemical**, v. 315, p. 213 (2009).

40. Fisch, Adriano G. ; Cardozo, Nilo S.M. ; Secchi, Argimiro R. ; Stedile, Fernanda C. ; Radtke, Cláudio ; De Sá, Denise S. ; da Rocha, Zênis N. ; Santos, João Henrique Z. dos ; SANTOS, J. H. Z. . Immobilization of

41. Zirconocene within Silica-tungsten by Entrapment: Tuning Electronic Effects Of The Support On The Supported Complex. **Applied Catalysis. A**, **General**, v. 370, p. 114 (2009).

42. FISCH, A ; CARDOZO, N ; SECCHI, A ; STEDILE, F ; LIVOTTO, P ; DESA, D ; DAROCHA, Z ; DOSSANTOS, J . Immobilization of metallocene within silica titania by a non-hydrolytic sol gel method. **Applied Catalysis. A, General**, v. 354, p. 88 (2009).

43. Silveira, Fernando ; Alves, Maria do Carmo Martins ; Stedile, Fernanda C. ; Pergher, Sibele B. C. ; dos Santos, João Henrique Zimnoch . The Role of the Support in the Performance of Grafted Metallocene Catalysts. **Macromolecular Reaction Engineering**, v. 3, p. 139 (2009).

44. Brambilla, Rodrigo ; Radtke, Cláudio ; Dos Santos, João H. Z. ; Miranda, Márcia S. L. ; SANTOS, J. H. Z. . An investigation on structure and texture of silica-magnesia xerogels. **Journal of Sol-Gel Science and Technology**, v. 51, p. 70 (2009).

45. GOLLMANN, M. A. C. ; CAPELETTI, L. ; MIRANDA, M. S. L. ; SANTOS, J. H. Z. . Modified-sorbents for acetone adsorption: application in ethylene polymerization process. **Chemical Engineering Journal**, v. 147, p. 383 (2009).

46. PETKOWICZ, D ; BRAMBILLA, R ; RADTKE, C ; SILVADASILVA, C ; DAROCHA, Z ; PERGHER, S ; DOSSANTOS, J . Photodegradation of methylene blue by in situ generated titania supported on a NaA zeolite. **Applied Catalysis. A, General**, v. 357, p. 125 (2009).

47. SILVEIRA, F. ; ALVES, M. C. M. ; STEDILE, F. C. ; PERGHER, S. B. C. ; RIGACCI, A.; SANTOS, J. H. Z. Effect of the silica texture on the structure of supported metallocene catalysts. **Journal of Chemical Catalysis. A, Chemical,** v. 298, p. 40 (2009).

48. Franceschini, Fernando C. ; Tavares, Tatiana T. da R. ; Bianchini, Daniela ; Alves, Maria do Carmo M. ; Ferreira, Maria Lujan ; Dos Santos, João H. Z. ; SANTOS, J. H. Z. .Characterization and evaluation of supported -dimethylsilylenebis(indenyl)zirconium dichloride on ethylene polymerization. **Journal of Applied Polymer Science**, v. 112, p. 563 (2009).

49. Borsali, R. Thermo-Responsive Copolymers Based on Poly(-isopropylacrylamide) and Poly[2-(methacryloyloxy)ethyl phosphorylcholine]: Light Scattering and Microscopy Experiments. **Macromolecular Chemistry and Physics** 210, 1726 (2009).

50. Fritzen-Garcia, M.B.; Oliveira, I.R.W.Z.; Zanetti-Ramos, B.G.; Fatibello-Filho, O.; Soldi, V.; Pasa, A.A.; Creczynski-Pasa, T.B. Carbon paste electrode modified with pine kernel peroxidase immobilized on pegylated polyurethane nanoparticles. **Sensors and Actuators. B, Chemical** 139, 570 (2009).

51. Salmoria, G; Ahrens, C; Beal, V; Pires, A; Soldi, V. Evaluation of post-curing and laser manufacturing parameters on the properties of SOMOS 7110 photosensitive resin used in stereolithography**. Materials and Design** 30, 758 (2009).

52. Domenech, S.C.; Bendo, L.; Mattos, D.J.S.; Borges, N.G.; Zucolotto, V.; Mattoso, L.H.C.; Soldi, V.. Elastomeric composites based on ethylene-propylene-diene monomer rubber and conducting polymer-modified carbon black. **Polymer Composites** 30, 897 (2009).

53. Fritzen-Garcia, M.B.; Zanetti-Ramos, B.G.; de Oliveira, C.S.; Soldi, V. ; Pasa, A. A.; Creczynski-Pasa, T.B. Atomic force microscopy imaging of polyurethane nanoparticles onto different solid substrates. **Materials Science & Engineering. C, Biomimetic Materials, Sensors and Systems** 29, 405 (2009).

54. RIGO, R. T.; PERGHER, S. B. C. ; PETKOWICZ, D. I. ; SANTOS, J. H. Z. . Um novo procedimento de síntese de zeólita A empregando argilas naturais. **Química Nova**, v. 32, p. 21 (2009).

55. Melo, A.; Bet, A.C.; Assreuy, J ; Debacher, N. A. ; Soldi, V . Adhesion of L929 mouse fibroblast cells on poly(styrene)/poly(methyl methacrylate) films. **Journal of the Brazilian Chemical Society** 20, 1753 (2009).

56. Lima, A.M.F.; Soldi, V; Borsali, R. Dynamic light scattering and viscosimetry of aqueous solutions of pectin, sodium alginate and their mixtures: effects of added salt, concentration, counterions, temperature and chelating agent. **Journal of the Brazilian Chemical Society** 20, 1705 (2009).

57. Oliveira, A.F.; Soldi, V; Coelho, C.M.M.; Miqueloto, A.; Coimbra, J.L.M. Preparation, characterization and properties of polymeric films with potential application in seed coatings. **Química Nova** 32, 1845-1849, 2009.

58. Cristiano CMZ; Fayad, S. J.; Porto, L. C.; Soldi, V. Protein-Based Films Cross-Linked with 1-Ethyl-3-(3-dimethylamino-propyl) carbodiimide hydrochloride (EDC): Effects of the Cross-Linker and Film Composition on the Permeation Rate of p-Hydroxyacetanilide as a Model Drug. **Journal of the Brazilian Chemical Society** 21, 340 (2010).

59. Soares, Rosane M.D.; Soldi, Valdir. The influence of different cross-linking reactions and glycerol addition on thermal and mechanical properties of biodegradable gliadin-based film. **Materials Science & Engineering. C, Biomimetic Materials, Sensors and Systems** 30, 691 (2010).

60. Caon, T.; Zanetti-Ramos, B.G.; Lemos-Senna, E.; Cloutet, E.; Cramail, H.; Borsali, R.; Soldi, V.; Simões, C.M.O. Evaluation of DNA damage and cytotoxicity of polyurethane-based nano- and microparticles as promising biomaterials for drug delivery systems. **Journal of Nanoparticle Research** 12, 1655 (2010).

61. Vasques C.T.; Domenech, S.C.; Barreto, P. L. M.; Soldi, V. Polypyrrole-modified starch films: structural, thermal, morphological and electrical characterization**. E-Polymers** 026, (2010)

62. Andreani, L.; Cercená, R.; Ramos, B.G.Z. ; Soldi, V. Development and characterization of wheat gluten microspheres for use in a controlled release system. **Materials Science & Engineering. C, Biomimetic Materials, Sensors and Systems** 29, 524 (2009).

63. BRAMBILLA, R. ; RADTKE, C. ; Santos, João Henrique Z. ; MIRANDA, M. S. L. . Silica-magnesia mixed oxides prepared by a modified Stöber route: Structural and textural aspects. **Powder Technology,** v. 198, p. 337 (2010).

64. Silveira, Fernando ; Brambilla, Rodrigo ; Silveira, Nadya Pesce ; do Carmo Martins Alves, Maria ; Stedile, Fernanda C. ; Pergher, Sibele B. C. ; dos Santos, João Henrique Zimnoch . Effect of textural characteristics of supported metallocenes on ethylene polymerization. **Journal of Materials Science**, v. 45, p. 1760 (2010).

65. Rossetto, Enéderson ; Petkowicz, Diego I. ; dos Santos, João H.Z. ; Pergher, Sibele B.C.; Penha, Fábio G. ; dos Santos, João Henrique Zimnoch . Bentonites impregnated with TiO2 for photodegradation of methylene blue. **Applied Clay Science** v. 48, p. 602 (2010).

66. ZELAYA, E., Schryvers, D., Tolley, A., Fichtner, P. F. P. Cavity nucleation and growth in Cu:Zn:Al irradiated with Cu+ ions at different temperatures. **Intermetallics** v.18, p. 493 (2010).

67. Fernandes, V, Schio, P, de Oliveira, A J A, Ortiz, W A, Fichtner, P, AMARAL, L, Graff, I L, Varalda, J, Mattoso, N, Schreiner, W H, Mosca, D H Ferromagnetism induced by oxygen and cerium vacancies above the percolation limit in CeO. **Journal of Physics: Condensed Matter**. , v.22, p.216004 (2010).

68. Cornejo, D.R., Peixoto, T.R.F., REBOH, S., Fichtner, P. F. P., de Franco, V.C., Villas-Boas, V., Missell, F.P. First-order-reversal-curve analysis of Pr:Fe:B-based nanocomposites. **Journal of Magnetism and Magnetic Materials**. , v.322, p.827 (2010).

69. REBOH, S., Barbot, J. F., Beaufort, M. F., Fichtner, P. F. P. H-induced subcritical crack propagation and interaction phenomena in (001) Si using He-cracks templates. **Applied Physics Letters**. , v.96, p.031907 (2010).

70. REBOH, S., Schaurich, F., Declemy, A., Barbot, J. F., Beaufort, M. F., Cherkashin, N., Fichtner, P. F. P. On the microstructure of Si coimplanted with H+ and He+ ions at moderate energies. **Journal of Applied Physics**. , v.108, p.023502 (2010).

71. Pureza, J.M. ; Neri, F. ; Lacerda, M.M. . Stoney equation limits for samples deformed as a cylindrical surface. **Applied Surface Science** , v. 256, p. 4408 (2010).

72. M.A.Z. Vasconcellos, R. Hinrichs, J.B.M. da Cunha e M.R.F. Soares, Mössbauer spectroscopy characterization of automotive brake disc and polymer matrix composite (PMC) pad surfaces**. Wear,** Volume 268, p. 715 (2010).

73. Gavini, Giulio ; Pessoa, Oscar Faciola ; Barletta, Fernando Branco ; Vasconcellos, M.A.Z. ; Caldeira, Celso Luiz . Cyclic Fatigue Resistance of Rotary Nickel-Titanium Instruments Submitted to Nitrogen Ion Implantation. **Journal of Endodontics**, v. 36, p. 1183 (2010).

74. COSTA, M. E. H. M., FREIRE JUNIOR, F. L., Deuterated amorphous carbon films: film growth and properties. **Surface & Coatings Technology.** , v.203, p.1193 (2010).

75. VIANA, G.A, Mottta EF, COSTA, M. E. H. M., FREIRE JUNIOR, F. L., MARQUES, Francisco das Chagas, Diamond-like carbon deposited by plasma techniques as a function of methane. **Diamond and Related Materials**, v.19, p.756 (2010).

76. Gómez, A.G. ; Recco, A.A.C. ; Lima, N.B. ; Martinez, L.G. ; Tschiptschin, A.P. ; Souza, R.M., "Residual stresses in titanium nitride thin films obtained with step variation of substrate bias voltage during deposition", **Surface & Coatings Technology** 204, 3228 (2010).

77. Marlla Vallerius da Costa ; T L Menezes ; Dalla Corte D. A.; OLIVEIRA, C. T. ; Malfatti C F., Iduvirges Lourdes Müller . Silane film obtained from a sol constituted with TMSPMA and TEOS and the hexavalent chromate conversion film: The comparative performance as a post-treatment of zinc coating. **ECS transactions**, v. 25, p. 123 (2010).

78. Marlla Vallerius da Costa; OLIVEIRA, C. T. ; Dalla Corte D. A. ; RIEDER E S ; Iduvirges Lourdes Müller ; Malfatti C. F. . Silane film obtained by sol gel process with cerium addition for post-treatment on zinc-talc composite coatings. **ECS transactions**, v. 25, p. 113 (2010).

79. Ramos, S.C. ; Vasconcelos, G. ; Antunes, E.F. ; Lobo, A.O. ; Trava-Airoldi, V.J. ; Corat, E.J. . Wettability control on vertically-aligned multi-walled carbon nanotube surfaces with oxygen pulsed DC plasma and CO2 laser treatments. **Diamond and Related Materials**, v. 19, p. 752 (2010).

80. Aguzzoli, C.; Marin, C.; Figueroa, C. A.; Soares, G. V.; Baumvol, I. J. R. "Physicochemical, structural, and mechanical properties of Si_3N_4 films annealed in O_2" **Journal of Applied Physics,** v. 107, p. 073521 (2010)

81. Barbosa, D.C.; Barreto, P.R.P. ; Trava-Airoldi, V.J. ; Corat, E.J. . Growth and characterization of diamond micro and nano crystals obtained using different methane concentration in argon-rich gas mixture. **Diamond and Related Materials**, v. 19, p. 768 (2010).

82. Ramos, S.C. ; Vasconcelos, G. ; Antunes, E.F. ; Lobo, A.O. ; Trava-Airoldi, V.J. ; Corat, E.J. . Total re-establishment of superhydrophobicity of vertically-aligned carbon nanotubes by CO_2 laser treatment. **Surface & Coatings Technology**, v. 204, p. 3073 (2010).

83. Marciano, F.R. ; Almeida, E.C. ; Lima-Oliveira, D.A. ; Corat, E.J. ; Trava-Airoldi, V.J. . Crystalline diamond particles into diamond-like carbon films: The influence of the particle sizes on the electrochemical corrosion resistance. **Surface & Coatings Technology**, v. 204, p. 2600 (2010).

84. Marciano, F.R. ; Lima-Oliveira, D.A. ; Da-Silva, N.S. ; Corat, E.J. ; Trava-Airoldi, V.J. . Antibacterial activity of fluorinated diamond-like carbon films produced by PECVD. **Surface & Coatings Technology**, v. 204, p. 2986 (2010).

85. Braga, N.A. ; Cairo, C.A.A. ; Ferreira, N.G. ; Baldan, M.R. ; Trava-Airoldi, V.J. . One-step CVD-diamond coating process on 3-D titanium substrates using reticulated vitreous carbon as a solid carbon source. **Diamond and Related Materials**, v. 19, p. 764 (2010).

86. Cemin, F.; Echeverrigaray, F. G.; Rovani, A. C.; Amorim, C. L.G. ; Basso, R. L. O. ; Baumvol, I. J. R.; Figueroa, C. A. "Influence of atomic and mechanical attrition on low temperature plasma nitriding of ferrous alloys" **Materials Science & Engineering. A, Structural Materials: properties, microstructure and processing**, v. 527, p. 3206 (2010).

87. Marciano, F.R. ; Almeida, E.C. ; Bonetti, L.F. ; Corat, E.J. ; Trava-Airoldi, V.J. . Improvement of diamond-like carbon electrochemical corrosion resistance by addition of nanocrystalline diamond. **Journal of Colloid and Interface Science**, v. 342, p. 636 (2010).

88. Rovani, A. C.; Fischer, R. R.; Cemin, F.; Echeverrigaray, F. G. ; Basso, R. L. O.; Amorim, C.L.G.; Soares, G.V.; Baumvol, I.J.R.; Figueroa, C. A. "Effect of hydrogen on plasma post-oxidation of ferrous alloys" **Scripta Materialia**, v. 62, p. 863 (2010).

89. Leite, M. V.; Figueroa, C. A.; Gallo, S. C.; Rovani, A.C.; Basso, R. L. O.; Mei, P. R.; Baumvol, I. J. R.; Sinatora, A. "Wear mechanisms and microstructure of pulsed plasma nitrided aisi H13 tool steel" **Wear** ,v. 269, p. 466 (2010).

90. Basso, R. L. O.; Pastore, H. O.; Schmidt, V.; Baumvol, I. J. R.; Abarca, S. A. C.; de Souza, F. S.; Spinelli, A.; Figueroa, C. A.; Giacomelli, C. "Microstructure and corrosion behaviour of pulsed plasma nitrided AISI H13 tool steel" **Corrosion Science**, v. 52, p.3133 (2010).

91. Radtke, C; Krug, C; Soares, GV; Baumvol, IJR; Lopes, JMJ; Durgun-Ozben, E; Nichau, A; Schubert, J; Mantl, S. 2010. Physicochemical and Electrical Properties of LaLuO3/Ge(100) Structures submitted to Postdeposition Annealings. **Electrochemical and Solid State Letters** 13 (5): G37-(2010).

Book Chapters:

1. Marciano, F. R. ; L.F. Bonetti ; Pessoa, R.S. ; J.S. Marcuzzo ; MASSI, M ; Santos, L.V. ; E. J. Corat ; Trava-Airoldi, V.J. . Mass Spectrometry Evaluation of the Improvement of DLC Film Lifetime Using Silver Nanoparticles for Application on Space Devices: Material Review and Etching Experiments. In: Nova Publishers. (Org.). Handbook on Mass Spectrometry: Instrumentation, Data and Analysis, and Applications. New York: Nova Publishers, 2009.

2. Krug, Cristiano; RADTKE, C. Nanocristais semicondutores. In: Adriana Raffin Pohlmann; Carlos Otávio Petter; Naira Maria Balzaretti; Sílvia Staniscuaski Guterres. (Org.). Tópicos em Nanociência e Nanotecnologia. 1 ed. Porto Alegre: Editora da UFRGS, 2010, v. 2 .

Communications presented in International Conferences:

1. Figueroa, C. A.; Portolan E.; Maia da Costa, M. E. H.; Dotto M. E. R.; Soares G. V.; Baumvol, I. J.R. ; Aguzzoli, C "Structural and mechanical properties of vanadium carbide obtained by dc reactive magnetron sputtering" 10th International Workshop on Plasma-Based Ion Implantation & Deposition, 2009, São José dos Campos – SP.

2. Amorim C. L. G.; Figueroa, C. A.; Zorzi, J. E.;Basso, R. L. O., Baumvol, I. J. R.; Perottoni, C. A. "RF-induced plasma nitriding of zirconia" 10th International Workshop on Plasma-Based Ion Implantation & Deposition, 2009, São José dos Campos – SP.

3. Strapasson G. ; Figueroa, C. A.; Soares G. V.; Baumvol, I. J. R.; Tentardini, E. K. "Low-friction TiN/MoS2 nano-structured coatings investigated before and after tribological application" 10th International Workshop on Plasma-Based Ion Implantation & Deposition, 2009, São José dos Campos – SP.

4. Aguzzoli, C.; Soares G. V.; Figueroa, C. A.; Baumvol, I. J. R. "Tribological and structural characterization of TiC and VC thin films deposited by DC magnetron sputtering" 10th International Workshop on Plasma-Based Ion Implantation & Deposition, 2009, São José dos Campos – SP.

5. Figueroa, C. A.; Baumvol, I. J. R.; C. Aguzzoli; Soares G. V. "Physicochemical and tribological investigations of TiC and VC thin films deposited on Si by DC reactive magnetron sputtering" 11th International Conference on Advanced Materials, 2009, Rio de Janeiro – RJ.

6. Gasparin A.; Baumvol, I. J. R.; Umpierre A. P.; Crespi A. E.; Figueroa, C. A.; Cemin F.; Nunes R. C. R.; Giacomelli, C "Adhesion measurement of Cu thin films on polyamide and polypropylene substrates" 11th International Conference on Advanced Materials, 2009, Rio de Janeiro – RJ.

7. Strapasson G.; Figueroa, C. A.; Soares G. V.; Basso, R. L. O.; Baumvol, I. J.R.; Tentardini, E. K. "Low-Friction TiN/ MoS2 Nano-structured coatings investigated before and after tribological application" 11th International Conference on Advanced Materials, 2009, Rio de Janeiro – RJ.

8. Cemin F.; Amorim C.L.G.; Basso, R. L. O.; Baumvol, I. J.R. ; Figueroa, C. A. "Mechanical and atomic attrition effects on low temperature plasma nitriding of ferrous alloys" 11th International Conference on Advanced Materials, 2009, Rio de Janeiro - RJ.

9. Rovani, A. C.; Cemin F. ; Echeverrigaray F.G.; Basso, R. L. O.; Fischer R.; G. Dropke ; Baumvol, I. J. R. ; Amorim C. L. G. ; Figueroa, C. A. "Plasma nitriding and post-oxidation mechanisms in ferrous alloys" 11th International Conference on Advanced Materials, 2009, Rio de Janeiro

10. Malfatti C. F.. Elaboration of YSZ films on porous substrates. In: Seventh International Latin-American Conference on Powder Tecnology, 2009, Atibaia. Seventh International Latin-American Conference on Powder Tecnology, 2009

11. Marlla Vallerius da Costa ; OLIVEIRA, C. T. ; Malfatti C. F. ; Bonino J P ; Iduvirges Lourdes Müller ; T L Menezes . Influence of Silane Films in the Zinc coating post-treatment. In: Seventh International Latin-Conference on Powder Tecnology, 2009, Atibaia. Seventh International Latin-Conference on Powder Tecnology, 2009.

12. Marlla Vallerius da costa ; OLIVEIRA, C. T. ; T L Menezes ; Iduvirges Lourdes Müller ; Malfatti C. F. . Electrochemical study of silane films and chromate conversion coatings applied on zinc coatings. 11th Internations Conference on Advanced Materials, 2009, Rio de Janeiro..

13. FREIRE JR, F.L.. Nanostructured carbon based-materials: thin films, nanotubes and composites (Palestra convidada no Indo-Brazil Symposium on Avanced Materials, Rio de Janeiro, 2009).

14. Marcelo Eduardo Huguenin Maia da Costa, Marta Elisa Rosso Dotto , Fernando Lázaro Freire Junior. Effects of the pressure and the self-bias voltage on the doped and undoped amorphous hydrogenated carbon films properties. 11th Internations Conference on Advanced Materials, 2009, Rio de Janeiro..

15. A. Viana and F. C. Marques, Amorphous carbon deposited without vacuum pumping during deposition" ICMCTF – San Diego, CA- USA, 2009.

16. F.C. Marques, G. A. Viana, E. F. Motta, D. S. Silva, A. D. S. Côrtes, Tetrahedral amorphous carbon (t-aC) deposited by filtered cathodic vacuum arc (FCVA) bombarded by argon ions, ICMCTF – San Diego, CA- USA, 2010.

17. Grande P. Energy loss calculations for MEIS, 19th Internacional Conference on Ion Beam Analysis, Cambridge, UK, 2009.

18. Grande P. Characterization of nanoparticles through MEIS The influence of the symmetrical lineshape 5th International Workshop on High-Resolution Depth Profiling.. Kyoto, Japão, 2009.

19. D.F. Franceschini, F.P. Pereira, D.M. Souza - New framework for structural characterization of a-C:H films from single-wavelength optical constants – 11th International Conference on advanced materials – ICAM 2009 – Rio de Janeiro, 2009.

20. Carlos Manuel Sanchez Tasayco,Marcelo Eduardo Huguenin Maia da Costa, Dante Ferreira Franceschini - Pulsed Nd:YAG laser-deposition carbon thin films: Effect of the laser fluency - 11th International Conference on advanced materials – ICAM 2009, 2009.

21. Fabiano Pinto Pereira,Dácio Moreira Souza and Dante Ferreira Franceschini - In-situ optical characterization of plasma deposited a-C:H films during deposition by CH_4 plasmas and erosion by N_2-H_2 plasmas - - 11th International Conference on advanced materials – ICAM 2009 – Rio de Janeiro, 2009.
22. Weber, T. ; Basso, R. L. O. ; SOARES, G. V. ; BAUMVOL, I. J. R. ; VASCONCELLOS, M. A. Z. ; KRUG, C. . Hysteresis effect and film characterization in DC reactive sputtering of titania and alumina. In: 11th International Conference on Advanced Materials, 2009, Rio de Janeiro.

23. COSTA, M. E. H. M., FREIRE JUNIOR, F. L., Deuterated amorphous carbon films: film growth and properties. Simposium: Protective Coatings and Thin films. E-MRS Spring Meeting 2009, Strasbourg, 2009.

24. CAMPOS, R. A. ; BARQUETE, D. M. ; Edwards, E. R. ; Trava-Airoldi, V.J. ; CORAT, E. J. . Deposition of CVD diamond films on WC-Co-TiC inserts for machining. 11th International Conference on Advanced Materials, 2009, Rio de Janeiro.

25. Larrudé, D. G. ; F. H. Monteiro ; M. E. H. Maia da Costa ; Fernando Lázaro Freire Jr. . Multi-walled carbon nanotubes functionalized with silver nanoparticles. 11th International Conference on Advanced Materials, 2009, Rio de Janeiro.

26. Weber, T.; Basso, R. L. O. ; SOARES, G. V. ; BAUMVOL, I. J. R. ; VASCONCELLOS, M. A. Z. ; KRUG, C.. Deposition and characterization of DC reactive magnetron sputtered titania and alumina coatings. In: 10th International Workshop on Plasma-Based Ion Implantation and Deposition, 2009, São José dos Campos. 10th International Workshop on Plasma-Based Ion Implantation and Deposition, 2009.

27. Ruth Hinrichs, Marcos Vasconcellos, Werner Oesterle, Claudia Prietzel,Magnetite formation observed with TEM on brake discs. First TMS-ABM International Materials Congress. Rio de Janeiro 2010.

28. Vasconcellos, MAZ, Lima, S.C. Hinrichs, R. Hardness evaluation, stoichiometru and grain size of titanium nitride films obtained with plasma nitriding on TiAlV samples. First TMS-ABM International Materials Congress. Rio de Janeiro 2010.

29. MAIA da COSTA, M E H; HOLGADO, D. P. ; FREIRE JR, F. L., Hydrophobicity changes promoted by argon and CF4 plasma treatments on DLC films, Symposium L: Carbon -or nitrogen-containing nanostructured composite films. E-MRS spring Meeting 2010, Strasbourg, 2010.

30. Multi-walled carbon nanotubes functionalized with silver nanoparticles, F. H. Monteiro ; Larrudé, D. G. ; M. E. H. Maia da Costa ; F. L. Freire Jr., Tallarico E. 11th International Conference on the science and application of nanotubes 2010, Montreal.

Software:

1. PowerMEIS – analysis of NPs via ion scattering. The manual can be found in:

https://docs.google.com/fileview?id=0Bw24Rtu3Nv_VZmJmNzdkNzEtNGI2Ni00OWM2LWFlNDMtYjRkNWU1NTUzNmUz&hl=pt_BR

Patents:

1. Kauling, A.P.; Figueroa, C.A.; Miotti, L; Giocamelli, C; Soares, G.V.; Baumvol, I.J.R. "Processo suportado por tela ativa em/sobre superfícies e estruturas obtidas a partir de tal processo" Instituto Nacional de Propriedade Industrial (INPI), 06.05.09, às 16:16 horas, protocolo nº 020090042881 (2009).

2. Filmes de carbono tipo diamante com partículas de diamante em sua estrutura: F.R. Marciano, L.F. Bonetti, E.J. Corat e V.J. Trava-Airoldi, patente depositada no INPI em 2009.

3. Patente depositada com a BRASKEM

   Pub. No.: WO/2010/001298 International Application No.: PCT/IB2009/052681
   Publication Date: 07.01.2010 International Filing Date: 22.06.2009
   Chapter 2 Demand Filed: 28.04.2010
   IPC: G01N 31/22 (2006.01), G01N 33/52 (2006.01)
   Applicants: Braskem S.A. [BR/BR]; 1561, Eteno st. Complexo Químico de Camaçari Camaçari (BR) (All Except US).
   Universidade Federal do Rio Grande do Sul [BR/BR]; 110, Paulo Gama Ave. Farroupilha Porto Alegre (BR) (All Except US).
   ACEVEDO, Edwin, Moncada [CO/BR]; (BR) (US Only).
   PIRES, Gilvan, Pozebon [BR/BR]; (BR) (US Only).
   DOS SANTOS, João, Henrique, Zimnoch [BR/BR]; (BR) (US Only).

4. R. G. F. Gonçalves, R. G. Lacerda, A.S. Ferlauto, L.O. Ladeira, K. Krambrock, M. V. B. Pinheiro, A. S. Leal, G. A. Viana and F. C. Marques "Processo de fabricação de semente radioativa para braquiterapia através da ativação neutrônica de uma matriz de carbono amorfo dopado com xenônio-124 e produto". Pedido de patente PI 0802834-6. Instituto Nacional de Propriedade Industrial (INPI),

Formation of high quality human resources

During the period covered by this report twenty one (21) students obtained their Doctor degree and twenty eight (28) obtained the Master degree. The following list contains the name of the student, the name of his advisor and the University where the degree was obtained. The Brazilian agency responsible for the fellowship is also quoted.

Besides the graduate students, dozens of undergraduate students participated of research activities developed a different Universities under the supervision of one of the main researchers of the Institute (INES). They usually have the *Iniciação Cientifica* fellowship from CNPq and state agencies, like FAPESP and FAPERJ.

Doctor degree:

1. Renato Barbosa de Oliveira. Incorporação de nitrogênio em nanotubos de carbono sintetizados por spray-pirólise. 2010. Tese (Doutorado em Física) - Pontifícia Universidade Católica do Rio de Janeiro, Coordenação de Aperfeiçoamento de Pessoal de Nível Superior. *Orientador:* Fernando Lázaro Freire Junior.

2. Cristian Viáfara. Transição no regime de desgaste por deslizamento dos aços: uma abordagem termodinâmica. 2010. Tese (Doutorado em Engenharia Mecânica) - Escola Politécnica da Usp, Fundação de Amparo à Pesquisa do Estado de São Paulo. *Orientador:* Amilton Sinatora

3. Maurícia Beddin Fritzen Garcia. Imobilização de enzimas em materiais nanoestruturados: atividade, estabilidade e aplicação da peroxidase imobilizada em bicamadas lipídicas e nanopartículas poliméricas. 2010. Tese (Doutorado em Quimica) - Universidade Federal de Santa Catarina, Conselho Nacional de Desenvolvimento Científico e Tecnológico. *Co-Orientador:* Valdir Soldi

4. Sara Aida Rodrigez Pulecio. Modelamento do ensaio de indentação instrumentada usando elementos finitos e análise dimensional - Análise de unicidade, variações experimentais, atrito e geometria e deformações do indentador. 2010. Tese (Doutorado em Engenharia Mecânica) - Universidade de São Paulo, Conselho Nacional de Desenvolvimento Científico e Tecnológico. *Orientador:* Roberto Martins de Souza.

5. Rafael M. Lattuada. Estudo da ecotoxicidade de efluentes da mineração de carvão e a aplicação de adsorventes alternativos em associação com fotocatálise heterogênea na remoção de metais e HPAs. 2010. Tese (Doutorado em Química) - Universidade Federal do Rio Grande do Sul, *Orientador:* João Henrique Zimnoch dos Santos

6. Samir Shubeita. Análise do Efeito de Proximidade e Explosão Coulombiana em Filmes Ultrafinos. 2010. Tese (Doutorado em Física) - Universidade Federal do Rio Grande do Sul, Conselho Nacional de Desenvolvimento Científico e Tecnológico. *Orientador:* Pedro Luis Grande.

7. Adriano Giraldi Fisch. Heterogeneização de metalocenos por encapsulamento em suportes funcionais. 2009. Tese (Doutorado em Engenharia Química) - Universidade Federal do Rio Grande do Sul, Coordenação de Aperfeiçoamento de Pessoal de Nível Superior. *Orientador:* João Henrique Zimnoch dos Santos.

8. Rafael Peretti Pezzi. Análise de Materiais Nanoestruturados Utilizando Feixes de Íons. 2009. Tese (Doutorado em Física) - Universidade Federal do Rio Grande do Sul, Coordenação de Aperfeiçoamento de Pessoal de Nível Superior. *Orientador:* Israel Jacob Rabin Baumvol.

9. Simone de Paula Moreira. Purificação de silício metalúrgico por fusão zonal horizontal em forno de feixe de elétrons. 2009. Tese (Doutorado em Doutorado em Engenharia Mecânica) - Universidade Estadual de Campinas, Conselho Nacional de Desenvolvimento Científico e Tecnológico. *Orientador:* Paulo Roberto Mei.

10. Adriano Friedrich Feil. Nanoestruturas de Óxidos de Al e Ti Obtidas a Partir do Processo de Anodização: Fabricação, Caracterização e Aplicações. 2009. Tese (Doutorado em Ciências dos Materiais) - Universidade Federal do Rio Grande do Sul, Coordenação de Aperfeiçoamento de Pessoal de Nível Superior. *Co-Orientador:* Livio Amaral

11. Rossano Lang Carvalho. Nanoestruturas Luminescentes FeSi2 Produzidas pela Técnica de Implantação e Irradiação Iônica: Caracterização Estrutural e Óptica. 2009. Tese (Doutorado em Ciências dos Materiais) - Universidade Federal do Rio Grande do Sul, Conselho Nacional de Desenvolvimento Científico e Tecnológico. *Orientador:* Livio Amaral.

12. Tatiana Lisboa Marcondes. Formação de nanopartículas de Sn e PbSe via implantação iônica em Si(100). 2009. Tese (Doutorado em Microeletrônica) - Universidade Federal do Rio Grande do Sul, Coordenação de Aperfeiçoamento de Pessoal de Nível Superior. *Orientador:* Paulo Fernando Papaleo Fichtner.

13. Juliana Carvalho Sá. Efeito da modificação de superfícies de titânio tratadas por plasma na proliferação de células-tronco visando aplicações odontológicas. 2009. Tese (Doutorado em Ciência e Engenharia de Petróleo) - Universidade Federal do Rio Grande do Norte, *Orientador:* Clodomiro Alves Junior.

14. Thercio Henrique de Carvalho Costa. Influência das espécies do plasma de N2-O2 na modificação de superfícies de poliester. 2009. Tese (Doutorado em Ciência e Engenharia de Materiais) - Universidade Federal do Rio Grande do Norte. *Orientador:* Clodomiro Alves Junior.

15. Paulo Fernandes Barbieri. Propriedades Eletrônicas e Estruturais do Xenônio Implantado em Silício Amorfo. 2009. Tese (Doutorado em Física) - Universidade Estadual de Campinas, Coordenação de Aperfeiçoamento de Pessoal de Nível Superior. *Orientador:* Francisco das Chagas Marques.

16. Michelle Cequeira Feitor. Efeito antibacteriano de tecidos têxteis cobertos por prata através da técnica de deposição por plasma.. 2009. Tese (Doutorado em Ciência e Engenharia de Materiais) - Universidade Federal do Rio Grande do Norte, *Orientador:* Clodomiro Alves Junior.

17. Palova Santos Balzer. Estudo comparativo do efeito plastificante de policaprolactona e dioctil ftalato em poli (cloreto de vinila). 2009. Tese (Doutorado em Ciência e Engenharia de Materiais) - Universidade Federal de Santa Catarina, *Orientador:* Valdir Soldi.

18. Aline Fernandes de Oliveira. Desenvolvimento, caracterização e aplicação de biofilmes e esferas, obtidos a partir de carboximetilcelulose e alginato de sódio em processos de liberação controlada de nutrientes. 2009. Tese (Doutorado em Quimica) - Universidade Federal de Santa Catarina, Conselho Nacional de Desenvolvimento Científico e Tecnológico. *Orientador:* Valdir Soldi.

19. Cláudia Menegaz Zaccaron Cristiano. Blendas formadas por caseína e gelatina: efeito da adição de plastificante e de agente reticulante e interações com copolímeros. 2009. Tese (Doutorado em Programa de Pós-Graduação em Química) - Universidade Federal de Santa Catarina, Conselho Nacional de Desenvolvimento Científico e Tecnológico. *Orientador:* Valdir Soldi.

20. Karin Graf. Desenvolvimento de revestimentos Nb/Al por PTA. 2009. Tese (Doutorado em Engenharia) - Universidade Federal do Paraná, Agência Nacional do petróleo. *Orientador:* Ana Sofia Clímaco Monteiro de Oliveira.

21. Myriano Henriques de Oliveira Júnior. Propriedades optoeletrônicas e estruturais de carbono amorfo tetraédrico. 2009. Tese (Doutorado em Física) - Universidade Estadual de Campinas, Coordenação de Aperfeiçoamento de Pessoal de Nível Superior. *Orientador:* Francisco das Chagas Marques.

Master Degree

1. Deise Schafer. Modificação da anisotropia magnética através de feixes de Íons. 2010. Dissertação (Mestrado em Física) - Universidade Federal do Rio Grande do Sul, Conselho Nacional de Desenvolvimento Científico e Tecnológico. *Orientador:* Pedro Luis Grande.

2. Larissa Brentano Capeletti. Efeitos da rota sol-gel no encapsulamento de indicadores colorimétricos e fluorimétricos e em suas performances como sensores de pH e gás amônia. 2010. Dissertação (Mestrado em Química) - Universidade Federal do Rio Grande do Sul, Conselho Nacional de Desenvolvimento Científico e Tecnológico. *Orientador:* João Henrique Zimnoch dos Santos.

3. Ivan Pozzobon Pires. Implicações da utilização de organoalcoxisilanos sobre a síntese de sílicas híbridas pelo processo sol-gel dopadas com antocianinas. 2010. Dissertação (Mestrado em Ciências dos Materiais) - Universidade Federal do Rio Grande do Sul, Coordenação de Aperfeiçoamento de Pessoal de Nível Superior. *Orientador:* João Henrique Zimnoch dos Santos.

4. Samira Jamil Fayad. Obtenção e caracterização de micro e nanopartículas a base de proteína isolada de soja. 2010. Dissertação (Mestrado em Química) - Universidade Federal de Santa Catarina, Conselho Nacional de Desenvolvimento Científico e Tecnológico. *Orientador:* Valdir Soldi.

5. Linana Appel Boufleur. Embalagens Metálicas e Alimentos: o caso do Atum Enlatado. 2010. Dissertação (Mestrado em Ciências dos Materiais) - Universidade Federal do Rio Grande do Sul, Coordenação de Aperfeiçoamento de Pessoal de Nível Superior. *Orientador:* Livio Amaral.

6. Cheila Rovani. Efeito do hidrogênio e mecanismos na pós-oxidação por plasma pulsado de ligas ferrosas nitretadas. 2010. Dissertação (Mestrado em Materiais) - Universidade de Caxias do Sul, Conselho Nacional de Desenvolvimento Científico e Tecnológico. *Orientador:* Carlos Alejandro Figueroa.

7. Saulo Cordeiro Lima. Desenvolvimento de um sistema de nitretação a plasma e investigação da influência da temperatura e composição da atmosfera na nitretação da liga Ti-6Al-4V. 2010. Dissertação (Mestrado em Física) - Universidade Federal do Rio Grande do Sul, Coordenação de Aperfeiçoamento de Pessoal de Nível Superior. *Orientador:* Marcos Antonio Zen Vasconcellos.

8. Douglas Soares da Silva. Camadas antirefletoras de carbono amorfo e carbeto de silício para células solares de silício cristalino. 2009. Dissertação (Mestrado em Física) - Universidade Estadual de Campinas, Fundação de Amparo à Pesquisa do Estado de São Paulo. *Orientador:* Francisco das Chagas Marques.

9. Aline de Lima Vieira. Deposição de filmes de carbono amorfo hidrogenado por plasmas de catodo oco.. 2009. Dissertação (Mestrado em Física) - Universidade Federal Fluminense, *Orientador:* Dante Ferreira Franceschini Filho.

10. Edson Hiromassa Takano. Revestimentos para eixos pelo processo de Plasma por Arco transferido. 2009. Dissertação (Mestrado em Engenharia Mecânica) - Universidade Federal do Paraná, Agência Nacional do petróleo. *Orientador:* Ana Sofia Clímaco Monteiro de Oliveira.

11. Wellington Linconl Chimanski de Souza. Simulação numérica do processo de revestimento por plasma de arco transferido. 2009. Dissertação (Mestrado em Engenharia Mecânica) - Universidade Federal do Paraná, . *Co-Orientador:* Ana Sofia Clímaco Monteiro de Oliveira.

12. Emiliano Chemello. Avaliação de diferentes potenciais interatômicos no cálculo do tensor de elasticidade do tungstato de zircônio. 2009. Dissertação (Mestrado em Materiais) - Universidade de Caxias do Sul, *Orientador:* Cláudio Antônio Perottoni.

13. Eduardo Portolan. Propriedades estruturais e mecânicas do carbeto de vanádio obtido por magnetron sputtering reactivo. 2009. Dissertação (Mestrado em Materiais) - Universidade de Caxias do Sul, *Orientador:* Carlos Alejandro Figueroa.

14. Fernando Bonatto. Síntese e Caracterização de Nanoestruturas Formadas pela Anodização de Titânio.. 2009. Dissertação (Mestrado em Ciências dos Materiais) - Universidade Federal do Rio Grande do Sul, *Co-Orientador:* Livio Amaral.

15. Diego Ivan Petkowicz. Zeólitas sintetizadas com fontes alternativas de silício e alumínio. Aplicação em fotocatálise. 2009. Dissertação (Mestrado em Ciências dos Materiais) - Universidade Federal do Rio Grande do Sul, Coordenação de Aperfeiçoamento de Pessoal de Nível Superior. *Orientador:* João Henrique Zimnoch dos Santos.

16. Cristóvão de Lemos. Síntese e caracterização de catalisadores Ziegler-Natta de alto rendimento: avaliação na polimerização de eteno. 2009. Dissertação (Mestrado em Química) - Universidade Federal do Rio Grande do Sul, *Orientador:* João Henrique Zimnoch dos Santos

17. Raquel Milani. Nitretação a plasma de zircônia parcialmente estabilizada. 2009. Dissertação (Mestrado em Materiais) - Universidade de Caxias do Sul, Conselho Nacional de Desenvolvimento Científico e Tecnológico. *Co-Orientador:* Gabriel Vieira Soares

18. Jumir Vieira de Carvalho Junior. Passivação Superficial de Germânio para Aplicações em Nanoeletrônica. 2009. Dissertação (Mestrado em Física) - Universidade Federal do Rio Grande do Sul, Conselho Nacional de Desenvolvimento Científico e Tecnológico. *Orientador:* Cristiano Krug.

19. Fabrício Pinheiro dos Santos. Uso de Simuladores para Previsão da Corrosão pelo CO2 em Aço Carbono na Indústria do Petróleo. 2009. Dissertação (Mestrado em Engenharia de Minas, Metalúrgica e de Materiais) - Universidade Federal do Rio Grande do Sul, *Orientador:* Carlos Eduardo Fortis Kwietniewski.

20. Raphael Piazzarollo loureiro. Avaliação da resistência à corrosão de juntas soldadas de aço inoxidável UNS S31703 (AISI 317L). 2009. Dissertação (Mestrado em Engenharia de Minas, Metalúrgica e de Materiais) - Universidade Federal do Rio Grande do Sul, *Orientador:* Carlos Eduardo Fortis Kwietniewski.

21. Maurício de Albuquerque Sortica. Caracterização de Nanoestruturas Através da Técnica de Meis. 2009. 0 f. Dissertação (Mestrado em Física) - Universidade Federal do Rio Grande do Sul, Conselho Nacional de Desenvolvimento Científico e Tecnológico. *Orientador:* Pedro Luis Grande.

22. Magnus Kaldieff Pereira. Ressonância de Plasmon de Superfície Localizado e Espalhamento Raman em Soluções Coloidais de Ouro. 2009. Dissertação (Mestrado em Física) - Universidade Federal do Rio Grande do Sul, Conselho Nacional de Desenvolvimento Científico e Tecnológico. *Orientador:* Ricardo Rego Bordalo Correia.

23. Adilto Pereira Andrade Cunha. Efeitos da adição de molibdênio e nióbio na microestrutura e propriedades mecânicas de aço 0,5 %C laminado a quente. 2009. Dissertação (Mestrado em Engenharia Mecânica) - Universidade Estadual de Campinas, Fundação de Pesquisa do Maranhão. *Orientador:* Paulo Roberto Mei.

24. Alex Soares Duarte. Fabricação e Caracterização de Nanoponteiras Metálicas para Microscopia Óptica de Campo Próximo. 2009. Dissertação (Mestrado em Física) - Universidade Federal do Rio Grande do Sul, Conselho Nacional de Desenvolvimento Científico e Tecnológico. *Orientador:* Ricardo Rego Bordalo Correia.

25. Marco Aurelio Rosso Santana Mendes. Estudo do desgaste de ferramentas com e sem revestimento de filmes finos utilizadas em operações de conformação a frio. 2009. Dissertação (Mestrado em Engenharia Mecânica) - Universidade de São Paulo. *Orientador:* Roberto Martins de Souza.

26. Francieric Alves de Araújo. Processamento e análise de imagens aplicados na caracterização da superfície de titânio submetido a um ensaio de cultura de célula. 2009. Dissertação (Mestrado em Ciência e Engenharia de Materiais) - Universidade Federal do Rio Grande do Norte, *Orientador:* Clodomiro Alves Junior.

27. Sergio Barros de Sousa. Modelo Mecânico de análise quantitativa da dureza de metais através de ensaios de penetração. 2009. Dissertação (Mestrado em Ciência e Engenharia de Materiais) - Universidade Federal do Rio Grande do Norte, *Orientador:* Clodomiro Alves Junior.

28. Duciane Oliveira de Freiteas. Análise do efeito do efeito da modificação superficial de tecido 100% algodão tratado com plasma de atmosfera CH4 e CH4/Ar. 2009. Dissertação (Mestrado em Ciência e Engenharia de Materiais) - Universidade Federal do Rio Grande do Norte, Coordenação de Aperfeiçoamento de Pessoal de Nível Superior. *Orientador:* Clodomiro Alves Junior.

Transfer of knowledge to the society

Our Institute developed four lines of action in this subject in its first year. Researchers from different sections of our Institute and industrial and media partners worked together in the following actions:

1) Diffusion of knowledge to the public in general using the web.

A website (**www.engenhariadesuperficies.com.br**) dedicated to surface engineering issues was created. Weekly, pieces of news, job and academic opportunities and events are published on our site. The site also gives visibility to our scientific production (list of papers and patents) and to our infrastructure and human resources. It has a "speak with us" section open to questions and requirements from the public, which received more than 30 contacts in the first year.

Besides that, we used popular social media pages (Slideshare, YouTube, Flickr) to publish 40 presentations prepared by our researches about surface engineering issues, an e-book about plasma nitriding, and videos and photos showing the beauty of surface engineering. Our members also produced weekly posts for our blog about surface engineering and society, including topics such as the history of surface engineering in Brazil, university-industry interaction and applications on health and textile industries.

The news and updates are communicated to our public through a monthly e-newsletter and a Twitter account.

Finally, our Institute had a constant presence on sites and newsletters of Industry Federations (Simplas, Simecs, CIC), universities (UCS, UFRGS, Inpe) and the CNPq site, as well as some mentions on regional newspapers and magazines dedicated to the industry. In total, 70 pieces of news mentioned our Institute and the surface engineering.

All these actions contributed significantly to generate a high volume of trustable information about surface engineering on the web in Portuguese, creating a virtuous circle of dissemination, searches and visibility.

Our content received up-to-date more than 68.000 views from the public. Our website conquered the first place in Google´s searches with the keywords "engenharia de superficies" (the Portuguese translation of "surface engineering").

2) Transfer of knowledge to the industrial sector.

A program of surface engineering training for human resources of the industry is being accomplished by our Institute in partnership with the Federation of the Metalworking Industries of Caxias do Sul (Simecs). Our researchers and partners gave 4 technical talks on surface engineering topics (tribology, coatings, plasma nitriding, nanotechnology), reaching 260 people. Our Institute also organized a 14 classes course (**Introduction to wear and friction**) given by prof. Amilton Sinatora (USP) at UCS, for both engineering students and Simecs associates.

Our Institute also acted in partnership with the Federation of Plastic Industries of Caxias do Sul (Simplas) for the dissemination of surface engineering. Two talks were given for more than 250 associates. Besides, our Institute was present with a stand at Plastech, one of the major Brazilian fairs of the plastic industry (18.000 participants).

At USP, our Institute offered two short courses given by external specialists. Each course attracted 40 people from both the industry and the university:

- **Principles of Surface Texturing** Prof. Izhak Etsion (Technion) at the Surface Phenomena Laboratory, University of São Paulo.
- **Surface Finish Metrology** organized with the Center of Excelence of Taylor Hobson (United Kingdom) at the Surface Phenomena Laboratory, University of São Paulo.

Besides that, 3 meetings were organized by our Institute to promote university-industry debate and action:

- **Solar-grade silicon development meeting** (November 2009, at Unicamp).

- **Tribological challenges on the next generation of flex-fuel engines** (August and December 2009, at Mahle headquarters and at USP).

Our environment also promoted the creation, in June 2009, of a spin-off company dedicated to plasma surface engineering. Plasmar Tecnologia was established by researchers and students from the UCS section of our Institute. Since its creation, it has been providing high technology surface treatments to the metalworking companies at Caxias do Sul. Presently, Plasmar is also working on R&D projects for the gas and oil industry.

Finally, there are many contracts between our laboratories and industries like Petrobras, Braskem, Frasle, Nanovetores and Villares for R&D activities.

3) Open-lab days for young students.

Many laboratories (UFRGS, UDESC, UCS, and PUC-RIO) had a special day where they were open for high-schools student's visits, as an effort to convince young people to follow a profession in science or engineering.

4) Organization of world class scientific meetings in Brazil.

The institute was also involved in the organization of:

- **Simposium Protective Coatings: Surface Engineering** at the International Conferences on Advanced Materials, September 2009, Rio de Janeiro (Chairs: Fernando Lázaro Freire Jr , Y.W. Chung and Israel J.R. Baumvol)

- **Brazil-Argentina School on Nanostructured Coatings**, collaboration with CBAN (Centro Brasil-Argentina de Nanotecnologia) at PUC-Rio, December 2009 (organizer: Fernando Lázaro Freire Jr.)

National Institute of Surface Engineering

CNPq
Conselho Nacional de Desenvolvimento Científico e Tecnológico

inct
institutos nacionais de ciência e tecnologia

Industrial Sponsors

SIMECS

SIMPLÁS
SINDICATO DAS INDÚSTRIAS DE MATERIAL PLÁSTICO DO NORDESTE GAÚCHO

SINDIALI

Sivecarga

Sindijoias

Support

Pontifícia Universidade Católica

www.engenhariadesuperficies.com.br